The spatial and temporal distribution of oceanic dimethylsulfide and its effects on atmospheric composition and aerosol forcing

by

Jan-Erik Tesdal
B.Sc., McGill University, 2011

A Thesis Submitted in Partial Fulfillment of the
Requirements for the Degree of

MASTER OF SCIENCE

in the School of Earth and Ocean Sciences

The spatial and temporal distribution of oceanic dimethylsulfide and its effects on atmospheric composition and aerosol forcing

by

Jan-Erik Tesdal
B.Sc., McGill University, 2011

Supervisory Committee

Dr. James R. Christian, Co-Supervisor
(School of Earth and Ocean Sciences)

Dr. Adam H. Monahan, Co-Supervisor
(School of Earth and Ocean Sciences)

Dr. Knut von Salzen, Departmental Member
(School of Earth and Ocean Sciences)

Supervisory Committee

Dr. James R. Christian, Co-Supervisor
(School of Earth and Ocean Sciences)

Dr. Adam H. Monahan, Co-Supervisor
(School of Earth and Ocean Sciences)

Dr. Knut von Salzen, Departmental Member
(School of Earth and Ocean Sciences)

ABSTRACT

The ocean emission and subsequent oxidation of dimethylsulfide (DMS) provides a source of sulfate in the atmosphere, potentially affecting the amount of solar radiation reaching the Earth's surface through both direct and indirect radiative effects of sulfate aerosols. DMS in the ocean can be quite variable with season and location, which in turn leads to high spatial and temporal variability of ocean DMS emissions. This study tested currently available observational and empirically-based climatologies of DMS concentration in the surface ocean. The exploration of the existing parameterizations mainly reveals the limitations of estimating DMS with an empirical model based on variables such as chlorophyll and mixed layer depth. The different algorithms show significant differences in spatial pattern, and none correlate strongly with observations. There is considerable uncertainty both in terms of the spatiotemporal distribution in DMS concentration and flux, as well as in the global total DMS flux. The present research investigates the influence of DMS on sulfate aerosols and radiative fluxes given different DMS climatologies in the fourth generation of the Canadian Global Atmospheric Climate Model (CanAM4.1). In general, the response in the radiative flux seems to follow the variation in the global mean flux of DMS linearly. Differences in the spatial and temporal structure of oceanic DMS have only a secondary effect on the radiative changes. The overall response of the atmosphere to the presence or

absence of structure of DMS in space and time is distinctly smaller compared to the possible uncertainty of this response associated with the magnitude of the annually averaged global flux.

Contents

List of Tables

List of Figures

ACKNOWLEDGEMENTS

I would like to express my sincere thanks, first and foremost, to my supervisors Dr. Adam Monahan, Dr. Jim Christian and Dr. Knut von Salzen for guiding me through my studies over the past three years.

I am grateful to all of the people who provided me with data or placed their data sets in the public domain. In particular, I want to thank O. Aumont, S. Belviso, C. de Boyer Montégut, E. Buitenhuis, S. Elliott, I. Masotti, R. Simó, M. Vogt, and M. Woodhouse for sharing data or helping me to find them.

Natural Sciences and Engineering Research Council (NSERC) of Canada and the CREATE Training Program in Interdisciplinary Climate Science at the University of Victoria provided me the ability to complete this project with its generous funding.

I also want to express my deepest appreciation to Marjorie Butler and Peter Larson, as well as to Birgit, Kaare and Lisa – my mother, father, and sister – for their love and their belief in me, and for the great support along the way that helped this thesis come to be.

Chapter 1

Introduction

The flux of biogenically derived dimethylsulfide (DMS) from the ocean represents a major source of sulfur into the Earth's atmosphere (Andreae and Raemdonck, 1983; Bates et al., 1992). The oxidation of DMS in the atmosphere produces sulfate aerosols, which affect incoming solar radiation directly, via scattering, and indirectly, by contributing to cloud condensation nuclei (CCN), which influence the radiative properties of clouds (Andreae and Crutzen, 1997; Charlson et al., 1987).

More than 40 years ago, Lovelock et al. (1972) presented the first quantitative measurements of DMS concentration in the surface ocean and the atmosphere, pointing to the importance of DMS in closing the world's sulfur budget. Interest in scientific research on DMS rose for several reasons, not least of which is its potential influence on Earth's climate. Shaw (1983) was the first to propose a link between ocean biota and the Earth's radiation budget via the emission of DMS. But the "CLAW hypothesis", proposed by and named for Charlson, Lovelock, Andreae, and Warren (1987), is generally credited as having launched the modern era of research into the role of DMS in the climate system. The CLAW hypothesis suggests the existence of a negative feedback loop involving phytoplankton and the Earth's climate through a link between temperature and DMS production (Charlson et al., 1987).

Although numerous studies have since investigated the details of the proposed mechanisms in this feedback loop, there is still no consensus about the importance of DMS in regional and global climate and about the response of the sulfur cycle to climate change. Recent studies have questioned the central premise of the CLAW hypothesis and some researchers assert that the climatic effects of DMS are relatively minor and that many other aerosol precursors (e.g., sea salt and organic compounds) could play an equal or greater climatic role (Quinn and Bates, 2011). Further evidence against

the CLAW hypothesis is the lack of evidence of a strong DMS-induced formation of CCN in a global aerosol microphysics model (Woodhouse et al., 2010, 2013). This is coupled with uncertainty about how changes in CCN affect cloud albedo (Stevens and Feingold, 2009). Finally, some modelling studies indicate that DMS production is insensitive to future changes in climate (Bopp et al., 2003; Vallina and Simó, 2007). Some model studies indicate a more substantial response of DMS in warming scenarios; however, they provide contradictory results, where DMS production can be either enhanced (Cameron-Smith et al., 2011; Gabric et al., 2005, 2004) or reduced (Kloster et al., 2007; Six et al., 2013) by increased carbon dioxide and climate change. Along with uncertainties in atmospheric chemistry and cloud physics, the uncertain influence of DMS in the present and future climate arises because DMS cycling in the ocean is more complex than was initially realized (Stefels et al., 2007).

Researchers have yet to achieve a consistent, complete understanding of the physical and biogeochemical processes that control the production of DMS and its removal from the ocean. It is known that DMS derives from a precursor compound, dimethylsulfoniopropionate (DMSP), which is produced mainly by a range of micro- and macroalgae, but also found in more complex organisms, including corals (Raina et al., 2013; Stefels, 2000). However, it is not known exactly why DMSP is produced or what selective advantage compensates for the metabolic cost of producing such a compound. Past studies have suggested various purposes for DMSP: as a factor in the osmoregulation (Stefels, 2000; Vairavamurthy et al., 1985), as a cryoprotectant (Karsten et al., 1992, 1996), as an antioxidant (Sunda et al., 2002), and as a grazing deterrent or chemical defense mechanism (Steinke et al., 2002; Wolfe and Steinke, 1996; Wolfe et al., 1997).

DMSP is produced in varying quantities by a number of phytoplankton classes (Keller et al., 1989). Production depends strongly on the type of algae, with low concentrations generally found in diatoms and high concentrations found in some other groups such as dinoflagellates, prymnesiophytes, and haptophytes (Keller et al., 1989; Stefels et al., 2007; Yoch, 2002). DMSP is released into the water during grazing (Wolfe and Steinke, 1996), viral lysis (Malin et al., 1998) and other forms of algal mortality (Nguyen et al., 1988). After DMSP enters the water column, it can be converted to DMS by the enzyme DMSP-lyase (Curson et al., 2008; Todd et al., 2009, 2007). Not all DMSP is converted to DMS (Kiene and Linn, 2000). Nonetheless, DMS production in surface waters seems to depend mostly on the rate at which phytoplankton cells release DMSP, coupled with bacterial activity that converts DMSP to DMS (e.g., Bates et al.,

1994; Kiene et al., 2000; Stefels, 2000). Demand for sulfur appears to be one factor in the bacterial DMSP conversion rate: high demand leads to high assimilation of sulfur and low conversion of DMSP to DMS (Kiene et al., 2000). Current experimental evidence is lacking, but some researchers have suggested direct transfer across the cell membrane as an additional source of DMS in the water column (Vallina et al., 2008; Vogt et al., 2010). Sunda et al. (2002) suggested that shortage of nutrients or increased levels of ultraviolet (UV) radiation might lead to intracellular cleavage of DMSP and a direct DMS release from phytoplankton cells.

DMS can be removed from the water by bacterial consumption (Vila-Costa et al., 2006), by photooxidation (Brimblecombe and Shooter, 1986; Kieber et al., 1996), and by outgassing to the atmosphere (Nightingale et al., 2000; Zemmelink et al., 2004a,b). The relative importance of these removal pathways depends on physical conditions and varies in time and space. Some studies have shown, for example, that exposure to UV radiation reduces bacterial consumption of DMS (Slezak et al., 2001; Toole et al., 2006). Other environmental factors likely control the rate of DMS consumption by bacteria, in particular the ones that regulate general bacterial activity, such as temperature and availability of nutrients (nitrogen, phosphorus) and dissolved organic matter. Photooxidation of DMS – yielding, among other products, dimethylsulphoxide (DMSO) – depends on incident solar radiation and temperature at the ocean surface (Toole et al., 2006, 2003). Outgassing of DMS from the ocean surface is of interest because of its potential climatic significance, but it is a relatively minor term in the ocean DMS budget. Potentially as little as 1-10% of ocean DMS production reaches the atmosphere (Bates et al., 1994; Malin et al., 1992). The dynamics of DMS(P) are described in detail elsewhere (e.g., Kiene et al., 2000; Simó, 2004; Stefels et al., 2007).

Despite extensive research, it has been difficult to completely elucidate the production and consumption processes of DMS, which involve the entire planktonic ecosystem including diverse phytoplankton taxa. Specific algal species can be identified as the most important DMSP sources, and the DMSP production rate is influenced by the physiological condition of the individual algal cells. Many factors, both biotic and abiotic, affect how much DMSP is converted into DMS and the turnover time of DMS in the water column (Stefels et al., 2007). This complexity explains why there is no clear relationship between DMS concentration and commonly measured parameters associated with plankton biomass or productivity (e.g., chlorophyll or nutrient concentrations). Thus, DMS fields cannot unambiguously be reconstructed from well-constrained biological and chemical fields, increasing the difficulty of using

models to project DMS concentrations in future climates.

A major milestone in DMS research was the compilation of a global DMS database (Kettle et al., 1999). This database helped to develop a better understanding of spatial and temporal patterns of DMS concentration and the extent of its interannual variability (Halloran et al., 2010). This database is a key tool for modellers attempting to develop diagnostic and prognostic formulations of DMS to include in global ocean models. However, spatial and temporal variations in DMS concentration, as well as interannual variability, are still not well constrained because the number of available observations is still relatively small. The current observational dataset provides only sparse information from wide expanses of the ocean. However, there are large temporal and spatial variations in the sea surface concentration of DMS (Asher et al., 2011; Tortell et al., 2011; Tortell, 2005). Ideally, one would have measurements uniformly distributed and at different times of the year to fully characterize the spatial and seasonal variability. Since data this comprehensive are not yet available, interpolation and extrapolation schemes are required to construct continuous global fields of DMS concentrations that are based on the available *in situ* observations (Kettle et al., 1999; Lana et al., 2011). These estimates generally indicate continuously elevated concentrations in tropical latitudes in contrast to low (winter) and high (summer) concentrations in temperate and high latitudes. However, one needs to recognize biases in both geographic and temporal distribution of the raw data, mainly attributable to the way cruises were planned and how frequently some locations were visited.

In general, there are three main approaches to estimating the global distribution of DMS concentration: (1) interpolation of *in situ* observations (Kettle et al., 1999; Lana et al., 2011); (2) empirical parameterizations (e.g., Anderson et al., 2001; Simó and Dachs, 2002), which use other fields to calculate DMS; and (3) prognostic formulations within a process-based model (Le Clainche et al., 2010). The following section describes each of these approaches in more detail.

1.1 Reconstructing global distributions of DMS

The earliest studies on this topic estimated DMS from a small number of measurements. The pioneering work by Bates et al. (1987) proposed a direct relationship between DMS flux and surface irradiance. This reconstruction of DMS flux found its first application in atmospheric modeling. Erickson et al. (1990) calculated a global field of ocean DMS concentration with the relationship from Bates et al. (1987). This preliminary

model of a global distribution of DMS concentration suggested a relationship between DMS and latitude, where concentrations are greatest at higher latitudes. However, this model failed to explain how DMS varies longitudinally. The work of Bates et al. (1987) was also used by Spiro et al. (1992) to construct a climatology of ocean DMS flux. Pham et al. (1995) considered the empirical relationship between solar radiation and DMS flux to derive the distribution of DMS emissions, by distributing an estimate of the global DMS source strength (19.2 TgS y^{-1}) over the world's oceans, modulated by the solar radiation reaching the ocean according to Bates et al. (1987). Other early estimates of spatial and temporal variations of DMS for specific regions, rather than globally, include Galloway et al. (1992); Liss et al. (1993); Tarrasón et al. (1995); Turner et al. (1996, 1995).

1.1.1 Observation-based DMS distributions

A major step towards improved, data-based global representation of surface ocean DMS concentration was the construction of a DMS climatology based on more than 15,000 *in situ* DMS measurements (Kettle et al., 1999). Similar to the World Ocean Atlas (WOA) approach of developing continuous fields of e.g., nitrate concentration (Garcia et al., 2010), the Kettle climatology was generated from available DMS measurements using extrapolation and interpolation techniques to derive continuous monthly fields of sea surface concentration of DMS. Kettle et al. (1999) used all available DMS measurements, organized them into grid boxes for each climatological month (from January to December), and constructed gridded datasets of DMS concentration. To obtain continuous data fields, one must interpolate (through space and time) between data points and extrapolate to fill regions with no data coverage. Shortly after the release of the DMS climatology by Kettle et al. (1999) (hereafter referred to as K99), an updated version was published by Kettle and Andreae (2000) (hereafter referred to as K00), which incorporated a minor adjustment to address problematic interpolated regions in the high northern latitudes in winter, and integrated a few additional DMS measurements.

The sparsity of DMS measurements is important given the high variability of DMS concentration. This lack of data was a serious shortcoming of the Kettle climatologies. Lana et al. (2011) produced an updated DMS climatology incorporating new measurements obtained between 2000 and 2009 (representing an almost threefold increase relative to K00, from ∼16,500 observations to 47,313). Given its release in

2010, the Lana climatology is commonly abbreviated as L10. Although L10 includes three times as many measurements as the older K99 and K00, many of the gridded DMS values are still based on interpolation and extrapolation methods that do not consider physical and biogeochemical processes. Furthermore, the climatologies of both Kettle et al. and Lana et al. involve a rather subjective division of the oceans into so-called biogeochemical provinces (Longhurst et al., 1995), which raises questions regarding the fidelity with which these climatological maps represent actual spatial and temporal patterns of DMS concentrations.

1.1.2 Empirical reconstructions of the DMS distribution

Alternative methods for deriving DMS distributions that are not prescribed functions of space and time have attracted attention for at least two reasons. First, observation-based DMS fields are a product of somewhat subjective (e.g., categorization of DMS data by biogeochemical provinces) and nonphysical methodologies and do not offer insight into the interactions between DMS concentration and ocean physical and biogeochemical processes. Secondly, such fields do not account for interannual variability and potential trends due to climate change. Shortly after the work of Kettle et al. (1999) and Kettle and Andreae (2000), a series of studies were conducted in which the available DMS database was used to construct algorithms that predict DMS distributions based on other parameters. The assumption underlying these empirical models is that realistic DMS variation can be produced by empirically derived equations describing the links between DMS and readily available biophysical parameters.

Anderson et al. (2001) used the available global set of *in situ* measurements, as presented by Kettle et al. (1999), to construct a multivariate empirical relationship between DMS and chlorophyll a concentration (hereafter, chlorophyll), light, and nitrate. In a sense, Anderson et al. (2001) utilized a proxy for primary productivity to derive DMS variations in the ocean. This approach resulted in high concentrations of DMS where productivity is generally high, such as the high-latitude oceans in summer as well as coastal and upwelling regions. However, the approach underestimates DMS spatial variability across lower productivity areas.

A major drawback in using bulk properties such as chlorophyll as a variable from which to calculate DMS values is that different phytoplankton groups produce varying amounts of DMSP and are thus associated with varying DMS concentrations

(Keller et al., 1989). To address this concern, the composition of the phytoplankton community has been used as additional information to construct a second class of DMS parameterizations (Aumont et al., 2002; Belviso et al., 2004b). The nonlinear relationships devised by Aumont et al. (2002) use chlorophyll and a measure of the phytoplankton community composition, the Fp ratio, to estimate DMS concentrations. The Fp ratio represents the proportion of diatoms within the phytoplankton community and is determined from pigment concentrations (fucoxanthin and peridinin), as described by Claustre (1994). However, pigment data are often scarce, and global ocean models do not include pigments as a readily available output. Aumont et al. (2002) approximated the Fp ratio as the ratio of silicious to nonsilicious phytoplankton. Instead of observational data, chlorophyll and Fp ratio values from a global ocean biogeochemical model were used. Thus, this approach was subject to model bias.

To overcome the necessity of using rarely-available pigment data or silicate ratios, Belviso et al. (2004b) modified the relationship devised by Aumont et al. (2002) to model the Fp ratio directly from chlorophyll. The new empirical relationship is a nonlinear function that calculates DMS solely from chlorophyll. Therefore, satellite chlorophyll data can be used to derive a global distribution of DMS. Similar to the approach of Anderson et al. (2001), a disadvantage of this approach is that it leads to DMS concentrations that are too dependent on chlorophyll. Subsequent studies have shown that in many regions DMS concentration shows no correlation, or even a negative correlation, with chlorophyll (e.g., Toole and Siegel, 2004).

To accommodate the lack of a consistent correlation between DMS concentrations and phytoplankton biomass or biological productivity, Simó and Dachs (2002) developed a two-equation algorithm that uses mixed layer depth (MLD) as a key predictor of DMS variability. Using data available at the time, Simó and Pedrós-Alió (1999) argued for the existence of a strong relationship between DMS production and MLD. Using the global DMS database (Kettle et al., 1999), Simó and Dachs (2002) found two relationships depending on the ratio of chlorophyll to MLD. In high chlorophyll-to-MLD cases (mostly associated with coastal areas and temperate to high latitudes during the productive season), they found that DMS is a linear function of the chlorophyll-to-MLD ratio. In low-productivity regions, where the chlorophyll-to-MLD ratio is lower than 0.02 mg m^{-4} (85% of the ocean surface), DMS concentration is estimated as a logarithmic function of MLD alone.

Aranami and Tsunogai (2004) refined the Simó and Dachs (2002) algorithm. In high-chlorophyll (low MLD) waters, the linear relationship between DMS and the

chlorophyll-to-MLD ratio remained unmodified. In less productive waters, where MLD is the only parameter used to estimate DMS concentration, Aranami and Tsunogai (2004) postulated that the concentration of DMS is determined by the variation in MLD through dilution, so that the product of DMS and MLD is constant. Independent data from the Pacific suggested that this inverse relationship between DMS and MLD provides a better fit than the logarithmic relationship of Simó and Dachs (2002).

The most recently-developed category of predictive approaches involves the use of a linear relationship between DMS and the amount of solar irradiance that is received in the upper mixed layer. Vallina and Simó (2007) estimated DMS concentration as a linear function of the solar radiation dose (SRD), which is determined from MLD and surface solar irradiance. Biological parameters, such as chlorophyll, the Fp ratio, and nutrient concentrations, are not taken into account. The approach has gained considerable interest because the influence of solar radiation is incorporated (Bates et al., 1987; Toole and Siegel, 2004) and because it only requires MLD and surface irradiance, which are readily available as global data products and are common outputs from models.

Miles et al. (2009) suggested a slight modification of the relationship described by Vallina and Simó (2007), assuming that the correlation between ultraviolet A radiation dose (UVRD) and DMS is a more direct biophysical relationship than DMS and SRD. This reasoning is based on experimental studies. Sunda et al. (2002) showed that some species produce more DMS under elevated UV radiation. Furthermore, an increase in UV radiation increases the DMSP-to-DMS conversion rate (Hefu and Kirst, 1997) through suppression of bacterial activity that consumes DMS and DMSP (Slezak et al., 2001; Toole et al., 2006).

Several studies have used empirical algorithms within global climate models to predict DMS concentrations and emissions in climate change scenarios. Bopp et al. (2003) made use of the relationship of DMS with chlorophyll and the Fp ratio (Aumont et al., 2002) to investigate the effect of a global warming scenario ($2\times CO_2$) on DMS concentration and flux. The calculated change in DMS flux (+2%) generated projections of radiative forcing that would result in only a slight climate feedback (Bopp et al., 2004). Gabric et al. (2004) used the parameterization of Simó and Dachs (2002) to compare present-day DMS concentration with a scenario in which atmospheric CO_2 was three times higher than present-day levels. As a consequence of increased CO_2, they predicted a global DMS flux increase of approximately +14%. Gunson et al. (2006) applied the DMS formulation of Anderson et al. (2001) to

suggest that global temperature changes of up to +1.6℃ or -0.8℃ could occur if DMS flux was decreased or increased respectively by a factor of two. The relationship of DMS with SRD (Vallina and Simó, 2007) was utilized in an ocean general circulation model (GCM) to predict DMS in a climate change scenario with a 50% increase in atmospheric CO_2 compared to the present day (Vallina et al., 2007b). The 50% increase in CO_2 resulted in a ∼1% increase of global mean DMS concentration. In total, these modelling studies suggest only small global increases in DMS flux as a result of anthropogenic forcing. Their results suggest that the response of DMS to climate change would be only a slight climate feedback. However, regional climates, particularly in the Southern Hemisphere, would be more strongly affected (Bopp et al., 2003, 2004; Gabric et al., 2004; Vallina et al., 2007b).

1.1.3 Description of available prognostic formulations

In addition to empirical parameterizations, prognostic models of DMS are the third method used to construct a global DMS distribution. Along with local 1D process-based models (e.g., Polimene et al., 2012; Steiner and Denman, 2008; Toole et al., 2008; Vallina et al., 2008), mechanistic DMS modules have been integrated into biogeochemical/ecosystem models within a 3D ocean framework (e.g., Elliott, 2009; Six and Maier-Reimer, 2006; Vogt et al., 2010). Because it addresses global DMS dynamics, the present study focuses on approaches that use a prognostic biogeochemical formulation within a global (3D) ocean model.

As these prognostic models have become increasingly complex, they have integrated a variety of different source and sink terms, production modeling, and explicit advection and removal of DMS(P) within an ocean ecosystem model (Le Clainche et al., 2010). In general, implementing a marine sulfur cycle has been conducted by coupling a sulfur module to a carbon or nitrogen-based plankton ecosystem model. The number of state variables in the sulfur module varies among approaches but usually includes DMS, particulate DMSP (DMSPp), and/or dissolved DMSP (DMSPd). Most of the models categorize plankton groups into subclasses or so-called functional groups, for which a specific DMSP cell quota (sulfur-to-carbon ratio) is defined. The cell quotas are based on available observations (Stefels et al., 2007) and are generally defined as a constant value for each functional group. Representations of heterotrophic bacteria and zooplankton are typically very simple (Le Clainche et al., 2010).

One of the first ecosystem models to incorporate DMS cycling was presented by

Gabric et al. (1993). This model is a network flow model describing the ocean plankton community in terms of nitrogen coupled with sulfur. This Gabric model has been extended and used to simulate DMS fluxes in the Southern Ocean (Gabric et al., 1996, 1995), the Barents Sea (Gabric et al., 1999) and the North Atlantic (Watts and Bigg, 2001). A series of studies (Gabric et al., 2003, 2005, 1998, 2001) applied the Gabric model to GCM output.

Chu et al. (2003) incorporated a simplified version of the DMS model of Gabric et al. (1993) within a high-resolution version (average 0.2° grid) of the ocean circulation model Parallel Ocean Program (POP). The prognostic DMS formulation in POP was the first fully mechanistic description of the production and removal of DMS that was integrated within a global eddy-permitting ocean GCM. Within the POP module, DMS is produced through the lysis of dissolved DMSP, which in turn is produced by phytoplankton. DMS is also released directly by plankton. DMS is removed by microbial (e.g., bacterial) consumption, photolysis, and gas exchange with the atmosphere. The description of the marine cycling of DMS by Chu et al. (2003) is relatively simple in that DMS production and consumption rates are globally and seasonally constant and are merely adjusted to ensure agreement with global climatologies at basin scale. Furthermore, in this model no distinctions are made for the rate among different plankton species. The marine sulfur module within POP, as part of the Community Climate System Model (CCSM), was subsequently developed in a series of studies (Chu et al., 2004; Elliott, 2009; Elliott et al., 2007) and now includes much greater complexity, including taxonomic resolution, incorporation of stress factors regulating general marine sulfur metabolism, and kinetics of bacterial uptake.

Another global process-based DMS model was presented by Kloster et al. (2006) and was further developed by Six and Maier-Reimer (2006) within the Hamburg Model of Ocean Carbon Cycling (HAMOCC5), the ocean biogeochemistry module of the Max Planck Institute for Meteorology Earth System Model (MPI-ESM). This approach ties the production of DMS to the export of opaline and calciferous shells. It further includes a source through phytoplankton cell disruption (grazing and senescence). DMS loss is modelled as consumption by bacteria, photolysis or outgassing to the atmosphere. The model does not take DMSP production or transformation into account, with the following justification: too little is known about the DMSP to DMS transformation process, and insufficient data regarding DMSPp concentration is available for assessment of model simulation of the concentration of this compound

to be feasible. Kloster et al. (2007) applied this approach to compare simulations of past and future climate conditions. A recent study by Six et al. (2013) applied the DMS module in HAMOCC5 (hereafter HAMOCC) to investigate the effect of ocean acidification on DMS production.

PlankTOM5 (Vogt et al., 2010) and PISCES (Belviso et al., 2012) contain more recently developed DMS modules. PlankTOM5 is a multiple phytoplankton functional type model comprising three phytoplankton groups (nanophytoplankton, diatoms and coccolithophorids), two zooplankton groups (micro- and mesozooplankton) and 29 different tracers (including iron, silica, phosphate, nitrate). The cycling of sulfur is modelled by interactions between the different plankton groups and DMSPp, DMSPd and DMS pools. Similarly, PISCES includes two phytoplankton groups (nanophytoplankton and diatoms) as well as micro- and mesozooplankton, and two sulfur tracers (DMS and DMSPp). Both for PISCES and PlankTOM5, the underlying physical model is the Océan PArallélisé (OPA) global GCM.

1.2 Previous intercomparison studies

A number of studies that critically examine the predictive capabilities of DMS models and algorithms have been published. Belviso et al. (2004a) compared seven global-scale climatologies derived from parameterizations and modeling (Anderson et al., 2001; Aumont et al., 2002; Belviso et al., 2004b; Chu et al., 2003; Simó and Dachs, 2002), as well as the widely used data-based Kettle climatologies (K99, K00). Altogether, a high level of uncertainty was observed for zonal and annual mean concentrations of DMS, although Belviso et al. (2004a) argue that some algorithms perform better than others in specific regions. The tropics were found to be less variable, with a coefficient of variation (CV) of 50%, than the high latitudes (CV = 100%), and uncertainties associated with the sea-surface DMS concentration were found to exceed those of the gas transfer velocity.

Other studies have conducted local comparisons of proposed algorithms and tested them with directly measured data, often from regions of the ocean that are believed to be exceptional in terms of ocean DMS production and/or DMS-aerosol interaction but are poorly sampled. Bell et al. (2006), for example, examined the performance of several algorithms by using measurements that were made as part of the Atlantic Meridional Transect (AMT) program. The authors noted a tendency for recent algorithms to overestimate DMS concentration in oligotrophic waters, with the dilution model by

Aranami and Tsunogai (2004) providing the best fit to the AMT data. Hind et al. (2011) tested a number of predictive algorithms with a comprehensive set of high-resolution data that were collected during the VocalsRex expedition in the southeast Pacific. Although none of the tested algorithms performed very well, the use of the Anderson et al. (2001) algorithm with *in situ* chlorophyll and *in situ* nitrate best captured the variability of offshore eddies and coastal processes. Asher et al. (2011) used high-resolution observations from the northeast subarctic Pacific to examine the variability of sea surface DMS concentration (along with other parameters) at very fine spatial and temporal scales. Using the observational data set to test the algorithms by Simó and Dachs (2002) and Vallina and Simó (2007), they confirmed the ability of these algorithms to predict large-scale seasonal changes in DMS in this region. However, the performance of the algorithms broke down at fine spatial and temporal resolution.

As explained above, the algorithm by Vallina and Simó (2007) assumes that mixed-layer SRD is related to DMS. Vallina and Simó (2007) argued that global surface ocean concentrations of DMS are more closely correlated with SRD in the mixed layer than with other parameters, such as chlorophyll or temperature. However, these findings were not supported by Belviso and Caniaux (2009) who found that only 19% to 24% of the variance in monthly surface DMS concentration in the northeast Atlantic can be explained by SRD, compared to 81% reported by Vallina and Simó (2007) in the northwest Mediterranean. Using the updated GSS database of DMS concentration measurements, Derevianko et al. (2009) could not confirm a robust relationship between SRD and DMS globally. A linear relationship between DMS and SRD, however, was supported by Miles et al. (2009) with the use of *in situ* data from the AMT program. Sensitivity tests further showed that the relationship between DMS and SRD is strongly affected by the model used for attenuation of irradiance (Miles et al., 2009). While such methodologies have been disputed (Hind et al., 2011), the possible existence of a closely coupled seasonal cycle that involves both SRD and DMS raises important questions, at the very least, concerning the appropriate scale for substantiating a climate feedback mechanism (Derevianko et al., 2009; Vallina and Simó, 2007). Derevianko et al. (2009) found that SRD accounted for only 14% of the total variance, but they noted that monthly mean data may not fully capture the effects of smaller scale phenomena, such as synoptic scale storms and cloud cover variations.

Halloran et al. (2010) examined two DMS parameterizations (Anderson et al., 2001;

Simó and Dachs, 2002), within a fully coupled Earth System Model (HadGEM2-ES), and argued that they can estimate independent observations of DMS concentrations with a level of skill similar to that of K99. The algorithms were generally found to be poor predictors of DMS concentration, partly because of presumed inaccuracies in the modelled biological fields. The authors contend that differences in predicted future seawater concentrations of DMS between the algorithms occurred largely because the algorithm by Simó and Dachs (2002) uses MLD as a parameter, while that of Anderson et al. (2001) does not. Woodhouse et al. (2010) calculated the sensitivity of cloud condensation nuclei (CCN) to changing DMS flux using five different DMS climatologies within a global aerosol microphysics model. A wide range of DMS fluxes was observed among the different climatologies, but CCN concentration was found to be relatively insensitive to changes in DMS flux.

Le Clainche et al. (2010) compared contemporary 3D process-based models (along with 1D, single column models) of DMS. Each of the four 3D models (POP-TGM, PISCES, HAMOCC, and PlankTOM5) depicted generally similar DMS(P) cycle processes, with none of the models explicitly representing bacteria. The models differed in their ability to capture the observed seasonal cycles of chlorophyll and DMS concentration at low and mid-latitudes. In this regard, POP-TGM was found to be the most successful in reproducing the change from positive (higher latitudes) to negative (lower latitudes) seasonal correlation between chlorophyll and DMS concentration. The models were more comparable in their ability to simulate chlorophyll than DMS.

1.3 Scope of this study

There are three distinct parts to this study: (1) An analysis of the various parameterizations and reconstructions of DMS concentration, (2) a sensitivity analysis of DMS flux for a range of DMS concentration fields and gas transfer formulations and (3) an investigation of the impact of different representations of DMS concentrations and fluxes on atmospheric composition and radiative fluxes in a comprehensive atmospheric GCM. Chapter 2 focuses on the ocean, where possible ways to represent ocean DMS concentration are outlined and tested in order to quantify uncertainties in DMS concentration. Chapter 3 is concerned with what happens at the air-sea interface, and analyzes dependence of DMS flux on different air-sea gas transfer models. Chapter 4 addresses the effects of DMS in the atmosphere, and how the uncertainty in spatial and temporal distribution of DMS concentration and the overall strength of DMS flux

affects the atmospheric sulfur cycle and aerosol radiative effects.

A nearly complete collection of existing DMS reconstructions allows thorough investigation of their similarities and differences. By comparing these different climatologies, one can identify regions in which climatologies generally agree or disagree with each other. Furthermore, given the expanded global repository of DMS measurements since the construction of K00 (GSS database), it is possible to appraise the strengths and weaknesses of each DMS reconstruction.

As described in Section 1.2, comparisons of a subset of the global DMS fields have previously been published. Belviso et al. (2004a) described the earlier observation-based climatologies (K99 and K00), the first set of parameterized DMS fields (Anderson et al., 2001; Aumont et al., 2002; Belviso et al., 2004b; Simó and Dachs, 2002), and one of the first prognostically modelled DMS fields (Chu et al., 2003). Le Clainche et al. (2010) compared an initial collection of prognostic DMS models (PlankTOM, POP-TGM, PISCES, and HAMOCC). Chapter 2 extends these analyses with an expanded set of DMS fields from new algorithms, a variety of input data fields and additional point observations of DMS.

Chapter 3 provides an assessment of the uncertainty in DMS flux due to variation in gas exchange parameterizations (in addition to the variation in DMS concentration). Air-sea gas exchange is a key process in the climatic influence of DMS. A considerable amount of research has been devoted to air-sea flux of DMS, and a number of standard parameterizations have been developed to model the efflux of DMS from the ocean. In this study only the most commonly used gas transfer models are considered; those of Liss and Merlivat (1986), Wanninkhof (1992), and Nightingale et al. (2000). The influence of the air-side resistance on DMS flux estimates will also be considered.

In Chapter 4, the atmospheric sulfur cycle (DMS, sulfur dioxide and sulfate) and associated radiative forcing of sulfate aerosol are investigated by coupling different DMS climatologies with the Canadian Atmosphere Model (CanAM4.1). The main focus of Chapter 4 is a set of sensitivity analyses to investigate the sensitivity of the atmospheric response to (1) the spatial and temporal structure of DMS concentration, (2) the relationship between flux and concentration of DMS, and (3) the overall DMS source strength. The observed sensitivities of atmospheric sulfur burdens and radiative forcing can then be translated into an estimate of uncertainty in climate effects of DMS given the range of DMS concentration and flux estimates.

Each chapter builds on the results of the preceding chapters. In Chapter 2, uncertainty in DMS concentration is considered, which is further used in Chapter

3 to assess uncertainty in DMS flux. Chapter 4 takes the uncertainty about DMS flux and assesses its implications for atmospheric chemistry and climate, using a set of model simulations. Hence, the combined studies of Chapters 2-4 will assess the role of DMS in the present climate by estimating and comparing uncertainties in the representations of concentration and air-sea exchange. A summary and conclusions are presented in Chapter 5, along with limitations of the current study and potential avenues for further research.

Chapter 2

Intercomparison of available reconstruction approaches for global modelling purposes

2.1 Introduction

The main goal of Chapter 2 is to compare a number of published representations of surface ocean DMS concentration for climate modelling. Research in the last ∼15 years has led to a range of different DMS reconstruction approaches. Global DMS fields were either directly derived from DMS observations (Kettle et al., 1999; Lana et al., 2011), calculated from other proxy data sets (e.g., Anderson et al., 2001; Simó and Dachs, 2002), or prognostically modelled (e.g., Vogt et al., 2010). Implementing these different fields in the model leads to differences in air-sea flux, atmospheric sulfur burden and aerosol concentration, and thus climate influence. Before any of these DMS representations are used as part of a modelling study (Chapter 4), the different fields are first evaluated and compared. With the use of current information on DMS dynamics in the ocean, derived DMS fields are examined to determine their geophysical and biogeochemical fidelity.

A number of global climatological maps derived from the approaches described above have been obtained for this intercomparison study. Given the complex DMS dynamics within the oceans, it is questionable whether the climatological fields of the monthly global distribution of DMS concentrations are geophysically plausible. The precision and/or accuracy of the emerging patterns and gradients of DMS concentration

in these climatologies might be inadequate for a robust estimate of DMS fluxes and its influence on climate. Outlining the differences and similarities among the fields can help determine what underlying reasons account for the different patterns of DMS distribution among different schemes.

The sensitivity of different algorithm outputs to different input fields (observational climatology versus model) is also examined. Depending on the field used, different data products can be used as an input for a specific algorithm to derive DMS distribution. This analysis gives insight into the level of sensitivity of the parameterizations in terms of differences in input fields, such as mixed layer depth (MLD), which is a key parameter in some algorithms. Mixed layer depth can be defined in different ways. The question to be considered is how sensitive a given algorithm is to the exact MLD definition. Large sensitivity would imply that the implementation of such an algorithm in an ocean model would require that its applicability to the exact formulation used to define the MLD in the ocean model be determined.

2.2 Methods

2.2.1 Datasets

The datasets considered in this thesis were obtained from various sources. Global fields of DMS concentration were either obtained directly as gridded fields or reproduced through various parameterizations using global fields of the input parameters. For intercomparison of DMS climatologies, all fields were regridded to a common $1^\circ \times 1^\circ$ grid. Most regridding was done by built-in functions in Ferret (http://ferret.pmel.noaa.gov/Ferret, Hankin et al. (2007)) or Matlab (http://www.mathworks.com/products/matlab). In case of irregular model grids, Climate Data Operators (https://code.zmaw.de/projects/cdo) were used to grid the data onto uniform, regular grids.

2.2.1.1 Observationally-based DMS climatologies

One of the central datasets used in this study are the observation-based monthly climatological fields of DMS. The contemporary L10 climatology (Lana et al., 2011) was downloaded from the Surface Ocean – Lower Atmosphere Study (SOLAS) website (http://www.bodc.ac.uk/solas_integration/implementation_products/group1/dms/).
For reference, the older DMS K00 climatology by Kettle and Andreae (2000) and K99 climatology by Kettle et al. (1999) were also obtained. The K00 climatology was

originally obtained from the National Center for Atmospheric Research (NCAR) data archive (http://rda.ucar.edu/datasets/ds289.2/), whereas the K99 climatology was the version used in the Canadian Earth System Model, provided by Knut von Salzen. All three climatologies were constructed using surface (0-10 m) DMS concentration measurements exclusively, with a 1°×1° resolution. No modification was made to the fields. Because the L10 climatology provides a direct update from the K99 and K00 climatologies, with a substantial addition of data (∼38,000 new samples) but a similar methodology, the L10 climatology was used as the reference climatology for comparing DMS distributions generated from models or empirical algorithms. Table 2.1 provides a list of the basic characteristics of the three observation-based climatologies that have been used in DMS research.

Table 2.1: Basic characteristics of past and contemporary DMS climatologies, including mean and standard deviation*.

Name	Number of Observations	Time span	Mean (nM)	σ_s (nM)	σ_t (nM)	Reference
K99	14,980	1972-1997	2.22	1.17	1.51	Kettle et al. (1999)
K00	∼16,500	1972-1999	2.17	1.14	1.66	Kettle and Andreae (2000)
L10	47,313	1972-2009	2.35	1.25	1.29	Lana et al. (2011)

* The mean is given as an area-weighted annual global mean. σ_s is the standard deviation in space (calculated as the area-weighted standard deviation of the annual mean distribution). σ_t is the standard deviation in time (calculated as the area-weighted mean of the global distribution of seasonal standard deviation).

The observational data on which the K99, K00, and L10 climatologies are based, are collected in the Global Surface Seawater DMS database (GSS database) and were obtained from NOAA-PMEL (http://saga.pmel.noaa.gov/dms). The dataset not only contains sea surface concentration of DMS, but includes a range of ancillary data (chlorophyll, light, MLD, etc.) for a subset of observations. The database includes a total of 48,134 DMS measurements, of which only 9984 contain DMS and chlorophyll. There are 4893 data points for DMSP (dissolved and/or particulate), but only 130 locations contain a full set of measurements. Previous studies (e.g., Kettle et al., 1999) used the GSS database to explore correlations of DMS with the other measured quantities in the dataset, but no single variable produced a significant correlation. The main use of the GSS database in this study was to evaluate reconstructions of DMS concentration, and thus mainly involves only DMS measurements and metadata

(location, date, and time).

2.2.1.2 Simulated DMS distributions

Besides the parameterized reconstruction considered in Section 2.2.2, DMS distributions have been obtained from global model simulations. Two modeled DMS datasets were obtained from the historical simulations of 20th century climate as standardized for the Coupled Model Intercomparison Project 5 (CMIP5, Taylor et al., 2012). One is from the Hadley Centre Global Environmental Model version 2 – Earth System model (HadGEM2-ES), and the other one is from the Max Planck Institute for Meteorology Earth System Model – Low Resolution (MPI-ESM-LR). Both datasets contain monthly outputs from historical simulations (1850 to 2005) and RCP 4.5/8.5 scenarios (Moss et al., 2010) from 2005 to 2100. The time period relevant to this study is between 1972 and 2010 because DMS observations are available only from that period. For the intercomparison of climatologies, simulated DMS distributions from HadGEM2-ES and MPI-ESM-LR were averaged to 12 monthly climatological fields (January to December) over this time period, and regridded to $1^\circ \times 1^\circ$ resolution.

The DMS output from HadGEM2 is generated within the global ocean biogeochemical model Diat-HadOCC (hereafter, HadOCC). DMS concentrations are derived from the SD02 empirical algorithm (Simó and Dachs, 2002), which calculates DMS as a function of model MLD and chlorophyll (Collins et al., 2011). The CMIP5 output of DMS from HadGEM2 represents a contemporary example of the online application of a parameterization within a global model to simulate DMS, in contrast to a fully prognostic treatment to simulate dynamics of DMS production and consumption (e.g., Vogt et al., 2010). The details of the implementation and evaluation of the DMS scheme in HadOCC are described in Halloran et al. (2010).

In contrast to HadGEM2-ES, the CMIP5 DMS dataset from MPI-ESM-LR simulates DMS with a fully prognostic formulation within the Hamburg Ocean Carbon Cycle model (HAMOCC) (Ilyina et al., 2013). The marine sulfur cycle within HAMOCC allows for the explicit representation of sources and sinks of DMS (Kloster et al., 2006; Six and Maier-Reimer, 2006) and is one of the four global 3D models that currently simulate DMS prognostically (Le Clainche et al., 2010). HAMOCC's DMS formulation includes a simple production term, a bacterial consumption term, removal by photolysis, and air–sea gas exchange. Unlike other prognostic schemes, HAMOCC describes only DMS explicitly, while its precursor compound DMSP is not considered as a

tracer (Ilyina et al., 2013). DMS production is related to export production of silicate and calcium carbonate, where scaling factors account for greater DMS production associated with calcareous vs. silicious phytoplankton. The consumption of DMS by bacteria is a simple Monod function with a temperature dependent maximum rate. The destruction of DMS through photolysis is controlled by a photolysis rate constant and the local solar radiation. The studies by Kloster et al. (2006, 2007) and Six and Maier-Reimer (2006) contain a detailed description of the HAMOCC DMS model.

Table 2.2: Basic characteristics of the prognostic DMS models evaluated. Mean and standard deviations are computed as in Table 2.1.

Name	Physical model	Biogeochemistry /Carbon cycle model	Mean (nM)	σ_s (nM)	σ_t (nM)	Reference(s)
HAMOCC	MPI-ESM-LR	HAMOCC5	2.05	1.81	1.11	Kloster et al. (2006), Six and Maier-Reimer (2006)
PlankTOM	OPA	PlankTOM5	1.74	0.80	0.77	Vogt et al. (2010)
PISCES	OPA	PISCES	1.64	0.93	1.04	Belviso et al. (2012)
POP-TGM	POP	DML-TGM	2.03	1.13	1.23	Elliott (2009)

Climatological maps of sea surface DMS concentration were obtained from other GCM simulations using prognostic DMS schemes via direct correspondence with the research groups. The models considered includes the ocean biogeochemistry model PlankTOM5 (Vogt et al., 2010), embedded in the OPA physical model. 12 monthly fields of simulated sea surface DMS concentration from the Pelagic Interaction Scheme for Carbon & Ecosystem Studies (PISCES) was provided by I. Masotti. This study also used annual and zonal mean DMS concentration fields derived from a model run of the POP Trace Gas Module (POP-TGM), as described in Elliott (2009). Table 2.2 shows the basic characteristics of the prognostic DMS models discussed in this study. All fields were regridded to a uniform, $1^\circ \times 1^\circ$ grid to ease intercomparison. For all the models the average grid resolution is slightly lower than $1^\circ \times 1^\circ$, such that no degradation of the data occurs due to the interpolation. It is important to note that the averaging period differs for each of the models. For PlankTOM5, the DMS dataset is derived only from the year 2006 (Vogt et al., 2010). For PISCES the 12

monthly concentration fields are from the fourth year of a short (< 5 years) sensitivity experiment, which was initiated after a spin up of several thousand years. The DMS distribution from POP-TGM is derived from one year of a standard model run forced with a repeating year of NCEP reanalysis (Elliott, 2009).

2.2.1.3 Datasets for parameterized DMS distributions

Further datasets were obtained in order to derive DMS distributions from algorithms (Section 2.2.2). As with the DMS fields, these were regridded to a common resolution of $1^\circ \times 1^\circ$. The construction of DMS fields via algorithms in the present study includes new and updated datasets that were not available at the time the algorithms were originally published. For instance, Anderson et al. (2001) used modelled nitrate concentration, whereas this study uses monthly climatological fields of nitrate from the World Ocean Atlas (WOA) 2009 (Garcia et al., 2010). There was no monthly observation-based nitrate climatology available to Anderson et al. (2001).

For the application of those algorithms making use of chlorophyll, satellite chlorophyll data from three different sensors (SeaWiFS, MODIS-Aqua, and MODIS-Terra) were combined to create a single climatology of chlorophyll. The chlorophyll dataset consists of 15 years of data (1998-2012). The SeaWiFS dataset starts in 1998 and continues through 2007. MODIS-Terra and Aqua data begin in 2001 and 2003 respectively and continue through 2012. For a given year, data from all available sensors are used to derive the climatological mean.

The chlorophyll climatology has 12 monthly mean fields. However, these data do not represent complete seasonal and global coverage. For example, there is an absence of data in the high latitudes of the winter hemisphere (because the sensors measure Earth radiance derived from backscattered solar radiation). In some months, certain regions completely lack data due to conditions such as persistent dust (e.g., in the Arabian Sea in July), clouds, or ice cover. A simple linear method was employed to interpolate temporal data gaps, while near-zero chlorophyll concentrations (10^{-7} mg m^{-3}) were assigned to high latitudes in winter. Underestimation of chlorophyll in the winter hemisphere is expected to have little effect on algorithm performance. For instance, for SD02 and AT04 it can be assumed that chlorophyll is sufficiently low in the high latitudes in winter that the algorithm will normally apply the MLD-only equation (see equation (3) in Section 2.2.2.3). A sensitivity test with AN01-derived DMS concentrations confirmed a marginal effect of the exact methodology of filling

the gaps in the chlorophyll dataset. As a lower extreme case, one approach used zero to fill the data gaps and, as an upper extreme, another approach filled gaps by linear interpolation. The difference in global mean concentration between those two extreme cases was just 0.05 nM (∼2%).

Various mixed layer depth (MLD) fields were obtained. MLD can be characterized by a range of criteria. In general, MLD is based on the first depth at which density or temperature changes by a specified amount relative to the surface. Among the available empirical approaches, various types of MLD climatologies were used. The original approach by Simó and Dachs (2002) used a MLD derived from WOA temperature and salinity fields with the MLD being the depth at which density is 0.125 kg m^{-3} higher than at the surface (Levitus, 1982). In contrast, Vallina and Simó (2007) used one of the MLD fields from de Boyer Montégut et al. (2004), defined as the depth at which temperature is 0.1°C lower compared to 5 m depth.

To explore the sensitivity of the algorithms to differences among MLD climatologies, a range of different data sources and MLD definitions were considered. Two main sources were used: those of de Boyer Montégut et al. (2004) and WOA (Levitus, 1982). Various types of MLD climatologies from de Boyer Montégut et al. (2004) were obtained from the Ifremer/Los Mixed Layer Depth Climatology website (http://www.ifremer.fr/cerweb/deboyer/mld/home.php). WOA 2009 temperature (Locarnini et al., 2010) and salinity fields (Antonov et al., 2010) were obtained to construct a climatology, in which MLD was defined as the depth at which density was 0.125 kg m^{-3} higher than at the surface. Furthermore, a monthly MLD simulated by the Canadian Earth System Model (CanESM2) with historical greenhouse-gas forcing was included, derived from averaging monthly fields from 1986 through 2005. This field corresponds to the variable "omlmax" in the CMIP5 data archive, and represents the maximum MLD in a given month.

For those algorithms making use of irradiance, all-sky surface shortwave irradiance products from the Clouds and the Earth's Radiant Energy System (CERES) (Kato et al. 2013; Loeb et al. 2009, http://ceres.larc.nasa.gov/) and the International Satellite Cloud Climatology Project (ISCCP) dataset (Bishop et al., 1997) were obtained. In addition, daily mean solar irradiance at the top of the atmosphere was calculated according to Brock (1981) and then converted into surface irradiance using a fixed transmission coefficient of 0.5 (Vallina and Simó, 2007).

A global dataset of satellite-surface ultraviolet (UV) radiation at Earth's surface, weighted for UV-A, was obtained from the NCAR Community Data Portal (http://cdp.

ucar.edu). The dataset is derived by averaging UV-A radiation between wavelengths 315 to 400 nm, over the years 1979 through 2000. The UV irradiance is defined at the Earth's surface, calculated with the Tropospheric Ultraviolet-Visible (TUV) radiative transfer model given estimates of ozone and clouds from NASA's Total Ozone Mapping Spectrometer (TOMS). A full description of the dataset is provided by Lee-Taylor et al. (2010).

2.2.2 The use of algorithms to reconstruct global distributions of DMS

Different types of algorithms have been derived empirically using available data, given a limited understanding of the underlying processes controlling sea surface concentrations of DMS. Table 2.3 lists all of the algorithms considered in this study and their general characteristics. It must be emphasized that all algorithms presented in this section are empirical. They have been constructed only from specific predictors and predictands, which are usually limited in geographical and seasonal coverage, with little or no sampling of interannual variability. Access to the entire updated database of DMS bottle data provides the opportunity to recalculate empirical coefficients for some of the algorithms. Based on the various available input datasets and the updated DMS database, the goal was to discover to what extent the coefficients could vary. If any coefficient in the algorithms was derived from the best fit between DMS bottle and corresponding input data, updated DMS and input datasets were used to reestimate these empirical coefficients. It was assumed that the functional forms were generally optimal for the given input data; however the coefficients are subject to retuning. Only some cases presented a convincing reason to reestimate coefficients and use those instead of the ones in the original publication. In most cases, the changes in the coefficients were minor or somewhat dubious, given the large spreads in the data.

The sensitivity of the modelled DMS concentration to variations in the input fields was tested. The focus was on input fields that tended to be less constrained between different data products and which were likely to show a difference between observation-based, reanalysis and model-derived products. For the final intercomparison, observation-based input fields were chosen for each DMS parameterization that would give rise to the best agreement with DMS observations.

Four principal classes of empirical models exist, distinguished by the predictor of DMS concentrations used. The first and only example of its class, Anderson et al.

Table 2.3: List of empirical algorithms and models evaluated in this study, including ranges of global mean and standard deviation of DMS concentration given a set of possible values of the input fields. DMS concentrations were computed as described in the text (Section 2.2.2). Mean and standard deviations are computed as in Table 2.1.

Name	Input fields	Range of			Reference
		mean (nM)	σ_s (nM)	σ_t (nM)	
AN01	chlorophyll, nitrate, surface irradiance	2.17-2.22	1.22-1.27	0.44-0.55	Anderson et al. (2001)
BE04	chlorophyll	1.55-1.76	1.19-1.36	0.35-0.46	Belviso et al. (2004a)
AU02†	chlorophyll, silica	1.70	1.65	0.43	Aumont et al. (2002)
SD02	chlorophyll, MLD	1.78-2.62	1.39-3.63	0.57-1.17	Simó and Dachs (2002)
HadOCC†	chlorophyll, MLD	2.09	2.23	1.01	Collins et al. (2011)
AT04	chlorophyll, MLD	1.36-2.62	1.29-3.09	0.66-1.59	Aranami and Tsunogai (2004)
VS07	MLD, surface irradiance	1.94-2.57	1.22-1.63	0.73-0.90	Vallina and Simó (2007)
MI09	MLD, surface UV irradiance	2.21-2.41	1.22-1.57	0.40-0.82	Miles et al. (2009)

† Model output.

(2001) used a proxy for primary productivity to derive the global monthly fields of DMS. Two other studies soon followed, which computed DMS concentrations from chlorophyll and an index of marine phytoplankton community structure (Aumont et al., 2002; Belviso et al., 2004b). The third class of studies use mixed layer depth as the critical variable to model DMS (Aranami and Tsunogai, 2004; Simó and Dachs, 2002). As a further refinement of the MLD approach, a fourth class of studies modelled DMS as a function of the so-called solar radiation dose, which, in turn, is mainly a function of MLD (Vallina and Simó, 2007). Descriptions are provided below of each algorithm discussed and tested in this study. For clarity, the following abbreviations are used to identify them: (1) AN01 (Anderson et al., 2001), (2) AU02 (Aumont et al., 2002) and BE04 (Belviso et al., 2004b), (3) SD02 (Simó and Dachs, 2002) and AT04 (Aranami and Tsunogai, 2004), and (4) VS07 (Vallina and Simó, 2007) and MI09 (Miles et al., 2009).

2.2.2.1 AN01

The AN01 scheme of Anderson et al. (2001) is an empirical relationship between DMS and the product of surface chlorophyll concentration (C), light intensity (J) and a nutrient term. The nutrient term (Q) is a Michaelis-Menten-type limitation factor: $Q = N/(K_N + N)$, where K_N is the half saturation constant (taken as 0.5 mmol N m^{-3}) and N is the sea-surface nitrate concentration. For the original AN01 parameterization, Anderson et al. used the GSS DMS database (Kettle et al., 1999), extracting DMS and *in situ* chlorophyll and combining them with monthly average values for light (Esbensen and Kushnir, 1981) and HadOCC simulated sea-surface nitrate concentration (Palmer and Totterdell, 2001). This resulted in 2622 locations that had DMS and values for chlorophyll, light, and nitrate; only a small fraction of the DMS observations in the database had a corresponding value for chlorophyll. A scatterplot of DMS vs. $\log_{10}(CJQ)$ using these data did not show a clear correlation, so Anderson et al. binned the data sequentially in ascending values of $\log_{10}(CJQ)$. Each bin had exactly 23 data points whose DMS concentration and $\log_{10}(CJQ)$ values were averaged to give 114 binned values. The DMS vs. $\log_{10}(CJQ)$ plot of those points showed a much clearer relationship. Then, the binned values were the basis of the least-squares broken-stick regression:

$$\begin{aligned} DMS &= 2.29 && \text{for} \quad \log_{10}(CJQ) \leq 1.72 \\ DMS &= 8.24[\log_{10}(CJQ) - 1.72] + 2.29 && \text{for} \quad \log_{10}(CJQ) > 1.72 \end{aligned} \tag{1}$$

For this study, the AN01 parameterization was re-evaluated with the updated GSS database, and new chlorophyll, shortwave radiation, and nitrate climatologies were used (Figure 2.1). Various data sources were used, including: the limited number of in-situ chlorophyll or satellite-derived chlorophyll, and shortwave radiation from either ISCCP or CERES (accounting for clouds). In addition, various binning methods with varied amounts of data in each bin were tested. One difference from the original approach of AN01 was that $\log_{10}(DMS)$ was used as the predictand rather than DMS (Figure 2.1). The broken-stick regression results are not strongly sensitive to the choice of dataset or bin number. The best-fit model is:

$$\begin{aligned} \log_{10}(DMS) &= 0.07\log_{10}(CJQ) + 0.23 && \text{for} \quad \log_{10}(CJQ) \leq 1.50 \\ \log_{10}(DMS) &= 0.52\log_{10}(CJQ) - 0.45 && \text{for} \quad \log_{10}(CJQ) > 1.50 \end{aligned} \tag{2}$$

Interestingly, with the additional data, a positive slope for data in the lower range

of $\log_{10}(CJQ)$ could be detected. A slightly stronger correlation could be achieved with observations when using the new regression based on the logarithmic transformation. Because the algorithm was meant to derive global DMS distribution from climatological data, the particular relationship above is only based on climatological satellite chlorophyll instead of *in situ* measurements. Furthermore, discrete DMS measurements were averaged in monthly $1^\circ \times 1^\circ$ bins, and each bin mean value was associated with the corresponding value of chlorophyll, light, and nitrate from the climatologies. Monthly global DMS fields were derived by using the new equation with monthly fields of chlorophyll concentration, irradiance, and nitrate.

2.2.2.2 AU02 / BE04

Aumont et al. (2002) presented diagnostic relationships to predict particulate DMSP as well as DMS concentration as a function of chlorophyll concentration and a ratio indicating the proportion of microphytoplankton (Fp-ratio). The Fp-ratio was originally defined as the ratio of the integrated concentrations of the pigments fucoxanthin (characteristic for diatoms) and peridinin (characteristic for dinoflagellates) to the sum of the integrated concentrations of diagnostic pigments of all taxa in a plankton community (Claustre, 1994). Due to the difficulty of estimating global distributions of those pigments (whether through models or observations), Aumont et al. (2002) estimated the Fp ratio with a silica ratio that is defined as the ratio of the local production of biogenic silica to the maximum production of biogenic silica. This proxy estimate was then applied in a global ocean model to derive the global distribution of DMS and DMSP. Global observation-based fields of either Fp-ratio or silica ratio were unavailable, so reconstructing DMS with the AU02 algorithm was impossible. Therefore, only the model output from the original publication (Aumont et al., 2002) was used. In the present study, AU02 represents a model-derived DMS reconstruction and is independent of observational input data.

Belviso et al. (2004b) modified the empirical relationship of Aumont et al. (2002) to describe DMS as a function of chlorophyll only. Pigment measurements from the Atlantic Ocean (Belviso et al., 2001) were used to come up with an empirical relationship that describes the Fp ratio as a function of chlorophyll concentration. Thus, Belviso et al. (2004b) were able to use global fields of chlorophyll from a 4-year (1998-2001) long dataset of satellite (SeaWiFS) measurements to generate monthly mean maps of sea-surface DMS concentration. As with AU02, the absence of global

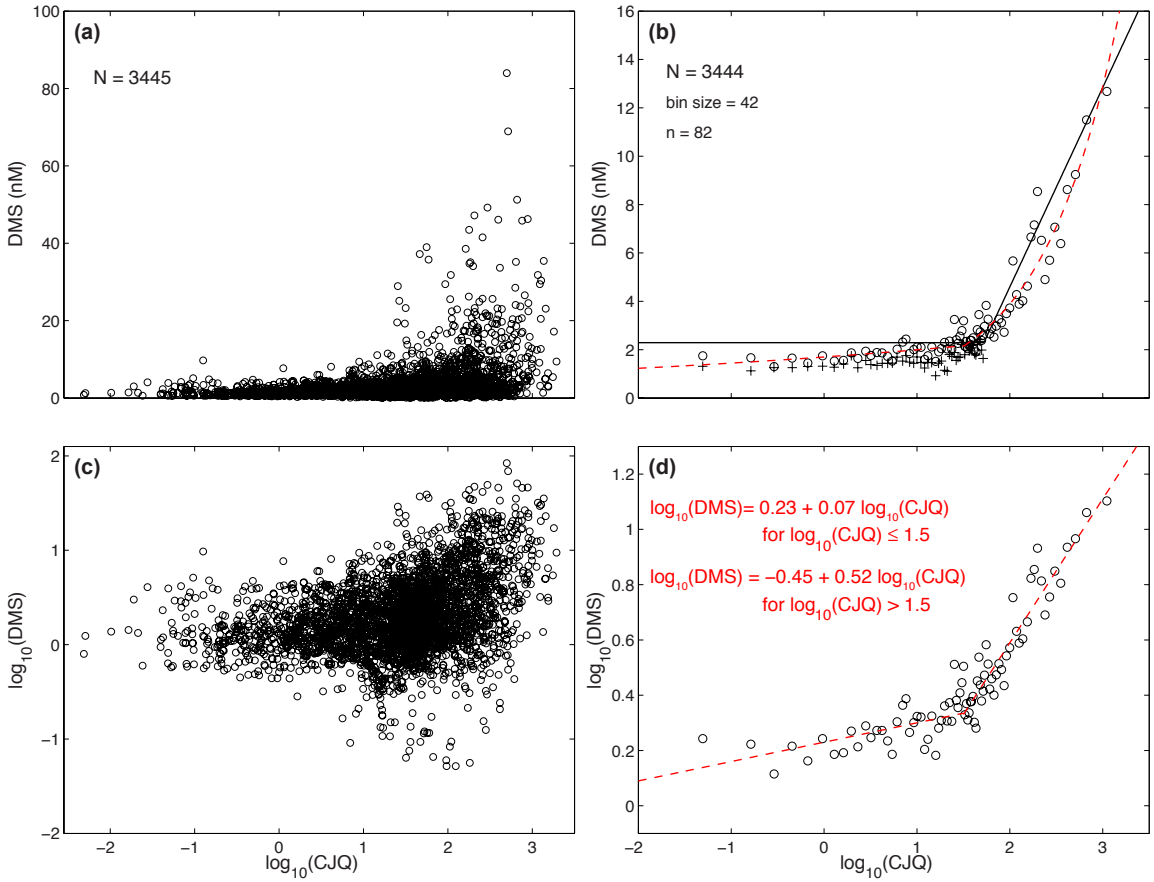

Figure 2.1: DMS (a, b) and $\log_{10}$(DMS) (c, d) vs. $\log_{10}$(CJQ). (a, c) Raw data (N = 3445); (b, d) Binned data after averaging 3444 raw data points into 82 bins containing each 42 raw data points. One data point was randomly omitted in the binning process to ensure that each bin contained an equal number of data points. A similar illustration was used as in Anderson et al. (2001) in order to better compare the original and new approaches. Open circles in (b) and (d) show the means of the 82 bins which are the basis of the new "broken-stick" regression. The median of each bin of 42 raw data values for $\log_{10}(\text{CJQ}) < 1.5$ are included in (b) to compare with the original approach of Anderson et al. (2001) who used the median for $\log_{10}$(CJQ) (instead of the mean) below the breaking point(s) for the regression. The "broken-stick" regression based on $\log_{10}$(DMS) vs. $\log_{10}$(CJQ) is shown as a red dashed line (b, d). Original AN01 regression is shown as a black solid line in (b).

pigment data precluded the present analysis from re-estimating model parameters of the BE04 algorithm.

To construct a monthly DMS climatology following the BE04 approach, the equations were used as described in Belviso et al. (2004b). In addition to the 4 years of monthly fields of chlorophyll, this study also used the climatological mean field for

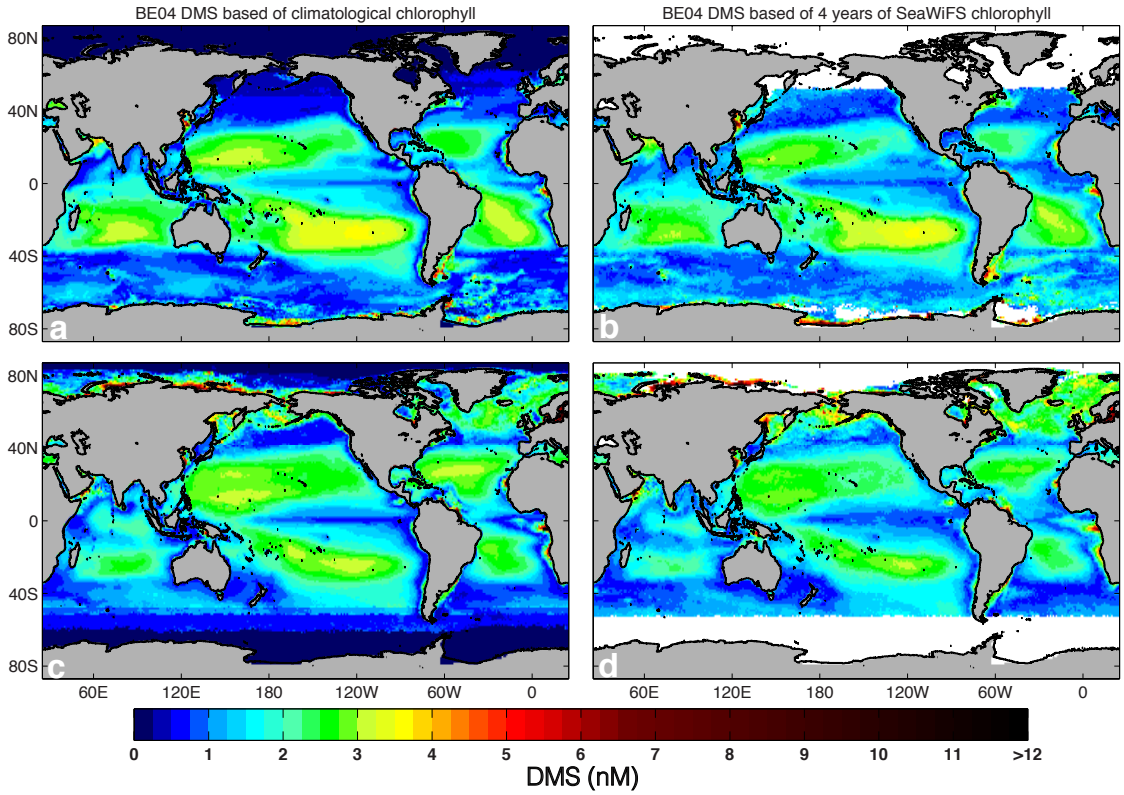

Figure 2.2: Seasonal mean of DMS surface concentration computed from BE04 algorithm. (a, c) Global distribution of DMS concentration derived from chlorophyll climatology and (b, d) from monthly fields of SeaWiFS chlorophyll. Seasonal distributions are averages for December-January-February (a, b) and June-July-August (c, d).

each month. While this approach might have reduced the resulting variability, the original dataset (S. Belviso, personal communication) showed close agreement with the climatological approach (Figure 2.2). For construction of the DMS climatology with the BE04 algorithm, the method of the original authors was used when filling data gaps. Instead of estimating missing chlorophyll data by linear interpolation, DMS was set as 0.2 nM for all regions where the chlorophyll climatology had no data. In addition, the same upper cutoff for DMS concentration, 50 nM, was used, to avoid unrealistically high values for coastal waters.

2.2.2.3 SD02 / AT04

Simó and Dachs (2002) built an empirical relationship that enables calculation of DMS from chlorophyll concentrations (Chl) and MLD. As in AN01, they chose data pairs

from the DMS database that included both chlorophyll and DMS. Filtering out those data points that had DMS $>$ 100 nM and/or chlorophyll $>$ 15 mg m^{-3} (that is, points associated with coastal areas or extreme algal blooms) resulted in 2385 data pairs. Each pair was then associated with a climatological MLD by corresponding latitude, longitude, and month. The MLD was taken from an older climatology (Monterey and Levitus, 1997). Data pairs were averaged according to cruises or hydrographic regions, resulting in 43 average values for DMS (nM), Chl (mg m^{-3}), and MLD (m). Given the 43 data points, Simó and Dachs (2002) came up with a two-equation algorithm with a threshold determined by the ratio of chlorophyll to MLD (Chl/MLD, mg m^{-4}):

$$\begin{aligned} DMS &= -\ln(MLD) + 5.7 \qquad \text{for} \quad Chl/MLD < 0.02 \text{ mg m}^{-4} \\ DMS &= 55.8\left(\frac{Chl}{MLD}\right) + 0.6 \qquad \text{for} \quad Chl/MLD \geq 0.02 \text{ mg m}^{-4} \end{aligned} \tag{3}$$

Since the -ln(MLD) term in equation (3) produces negative DMS concentration for very large MLD, a lower limit of zero had to be imposed for the calculated DMS concentration.

Aranami and Tsunogai (2004) considered additional observational DMS data from northern North Pacific regions using the method proposed by Simó and Dachs (2002). They found that the Simó and Dachs algorithm is not entirely consistent with observations in the open ocean. In the case of Chl/MLD $<$ 0.02 mg m^{-4}, the SD02 relationship underestimates DMS in shallower MLD (MLD $<$ $\sim$40 m) and overestimates it in deeper mixed layers. Aranami and Tsunogai (2004) only reconsidered the MLD-only equation of the piecewise relationship of Simó and Dachs (2002) (first line in equation (3)). Instead of the inverse logarithmic regression with MLD, they suggested a simple dilution model as an alternative. The dilution model produced by Aranami and Tsunogai (2004) is

$$DMS \times MLD = \text{constant} \qquad \text{for} \quad Chl/MLD < 0.02 \text{ mg m}^{-4} \tag{4}$$

The given observation yielded a best-fit relationship of DMS$\times$MLD = 60$\pm$30 μmol m^{-2}. The dilution model suggests a variability in DMS that is larger than that given by Simó and Dachs (2002) (see Figure 5 in Aranami and Tsunogai (2004)).

The present study reconsidered both approaches with the complete GSS DMS database and the chlorophyll climatology and MLD climatologies. Use of additional data that included all ocean regions showed much more variability than the results

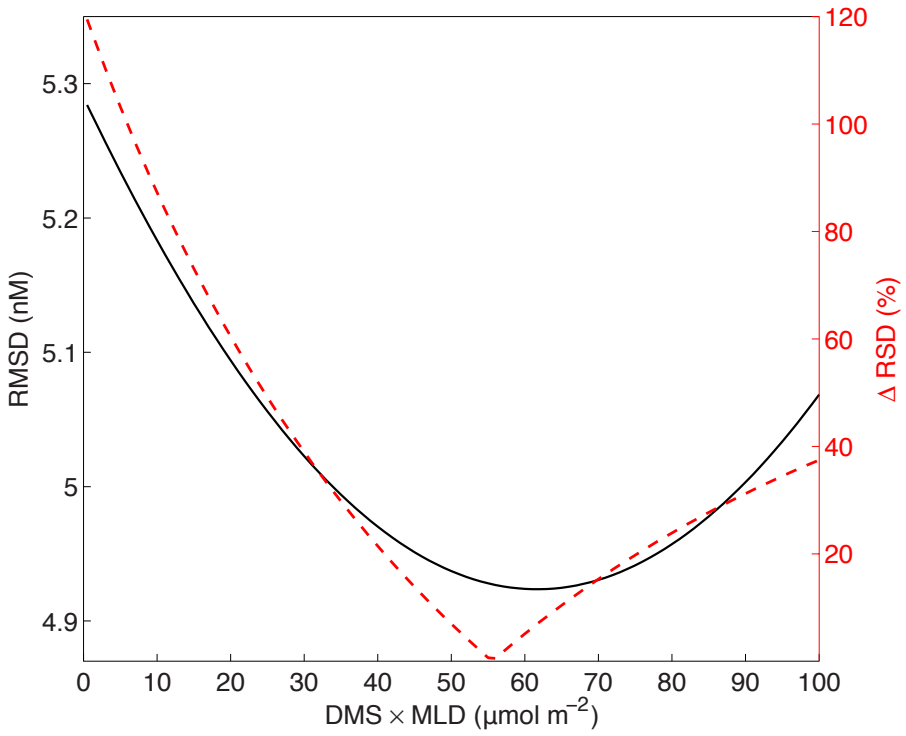

Figure 2.3: Variation in the root mean square difference (RMSD) and the difference in relative standard deviation (RSD) between AT04 derived and observed DMS with DMS×MLD for Chl/MLD< 0.02 mg m^{-4}.

of Simó and Dachs (2002) indicated. The regression model was not robust to a variation of binning approaches, such that a regression analysis could not detect a robust best-choice relationship between DMS and MLD. Therefore, it was decided to retain the equations as published in Simó and Dachs (2002) to create a monthly climatology of DMS fields using the composite chlorophyll climatology and available MLD fields.

For the AT04 approach, the relationship DMS×MLD = 56 μmol m^{-2} was used to reconstruct global fields of DMS concentration, because this value minimized the misfit between model and the observations (Figure 2.3). Considering various binning techniques and different MLD climatologies, Spearman rank correlation for the AT04 model with observations ranged from 0.27 to 0.41. The MLD fields of de Boyer Montégut et al. (2004) resulted in the best possible correlation with observations. AT04 derived DMS distributions with MLD based on a fixed density criterion (depth at which $\sigma_\theta > 0.03$ compared to σ_θ at 10 m depth) or a fixed temperature criterion (0.2℃ departure with respect to the temperature at 10 m)

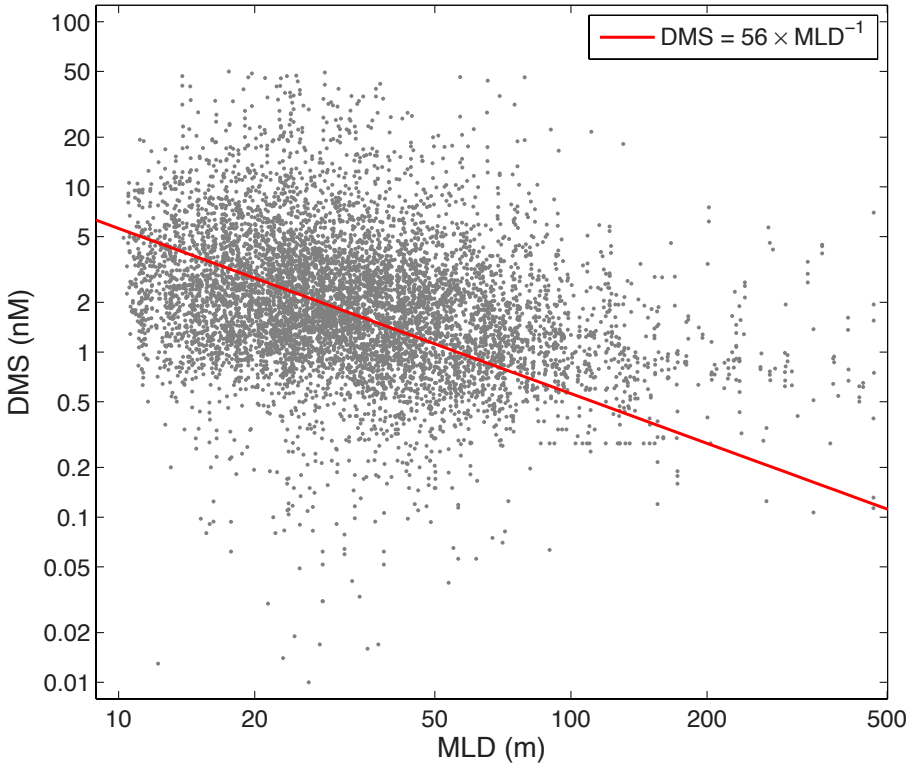

Figure 2.4: Regression for the AT04 algorithm for DMS vs. MLD in case of Chl/MLD$<$ 0.02 mg m^{-4}. Averages of DMS and MLD for 5°×5° latitude-longitude grid boxes are shown as grey data points.

resulted in similar correlation with observations. The correlation between modelled and observed DMS was relatively insensitive to DMS×MLD ranging from 30 to 60 μmol m^{-2}. For DMS×MLD $>$ 60 μmol m^{-2}, correlation with observations declined. The constant value of 56 μmol m^{-2} for DMS×MLD was chosen so that the relative standard deviation (sigma/mean) of the resulting DMS distribution was closest to that of the observational (GSS) DMS dataset (for DMS $<$ 50 nM). Furthermore, DMS×MLD = 56 μmol m^{-2} is approximately the value for which the root mean square difference between parameterized and observed DMS is at a minimum (Figure 2.3). However, the scatter of the data is very large (Figure 2.4).

2.2.2.4 VS07 / MI09

Vallina and Simó (2007) investigated the possibility that seawater concentration of DMS is linked to the exposure to sunlight that organisms in the sunlit ocean surface layer receive. They defined a so-called solar radiation dose (SRD) to describe the

exposure of sunlight the upper mixed layer receives on average at a certain time of the year. As in Vallina and Simó (2007), SRD was calculated in the present study assuming an exponential decay of the daily average surface solar irradiance (I_0) with depth, such that

$$SRD = \frac{I_0}{(kMLD)} \left(1 - e^{-kMLD}\right) \tag{5}$$

where I_0 is the daily average surface solar irradiance, and k the light-extinction coefficient. For the global ocean, Vallina and Simó (2007) calculated daily average top-of-the-atmosphere solar irradiance (Brock, 1981) and then applied a transmission coefficient of 0.5 to obtain I_0. This methodology was tested along with more realistic satellite derived surface irradiance products from CERES and ISCCP. Furthermore, various MLD climatologies based on different criteria were considered. In the original study by Vallina and Simó (2007), MLD was obtained from de Boyer Montégut et al. (2004), with a fixed temperature criterion, taken as the depth at which temperature was 0.1℃ lower than the temperature at 5 m depth (hereinafter referred to as VS07it). The present study also uses two additional MLD climatologies from de Boyer Montégut et al. (2004) (referred to as BMit and BMip), as well as MLD derived from the World Ocean Atlas 2009 temperature (Locarnini et al., 2010) and salinity fields (Antonov et al., 2010) (referred to as WOA09). Vallina and Simó (2007) light-extinction coefficient of $k = 0.06$ m^{-1} was adopted, based on previous experimental studies (Smith and Baker, 1979).

The DMS-SRD linear relationship was re-fitted for the different light and MLD climatologies, based on the approach of Vallina and Simo (2007). To construct a global relationship between DMS and SRD, the ocean was divided into 10°×20° latitude-longitude boxes. For each month, gridded SRD data and available DMS measurements from the GSS DMS database were averaged within the boxes. Further averaging of the DMS and SRD data by 15 W m^{-2} intervals reveals a linear relationship between DMS and SRD. Linear regression analyses of DMS vs. SRD for each combination of MLD and light fields yield corresponding equations that can be used to construct a global climatology of DMS from global fields of MLD and light. Figure 2.5 (a) through (d) illustrate examples of linear regression between DMS and SRD.

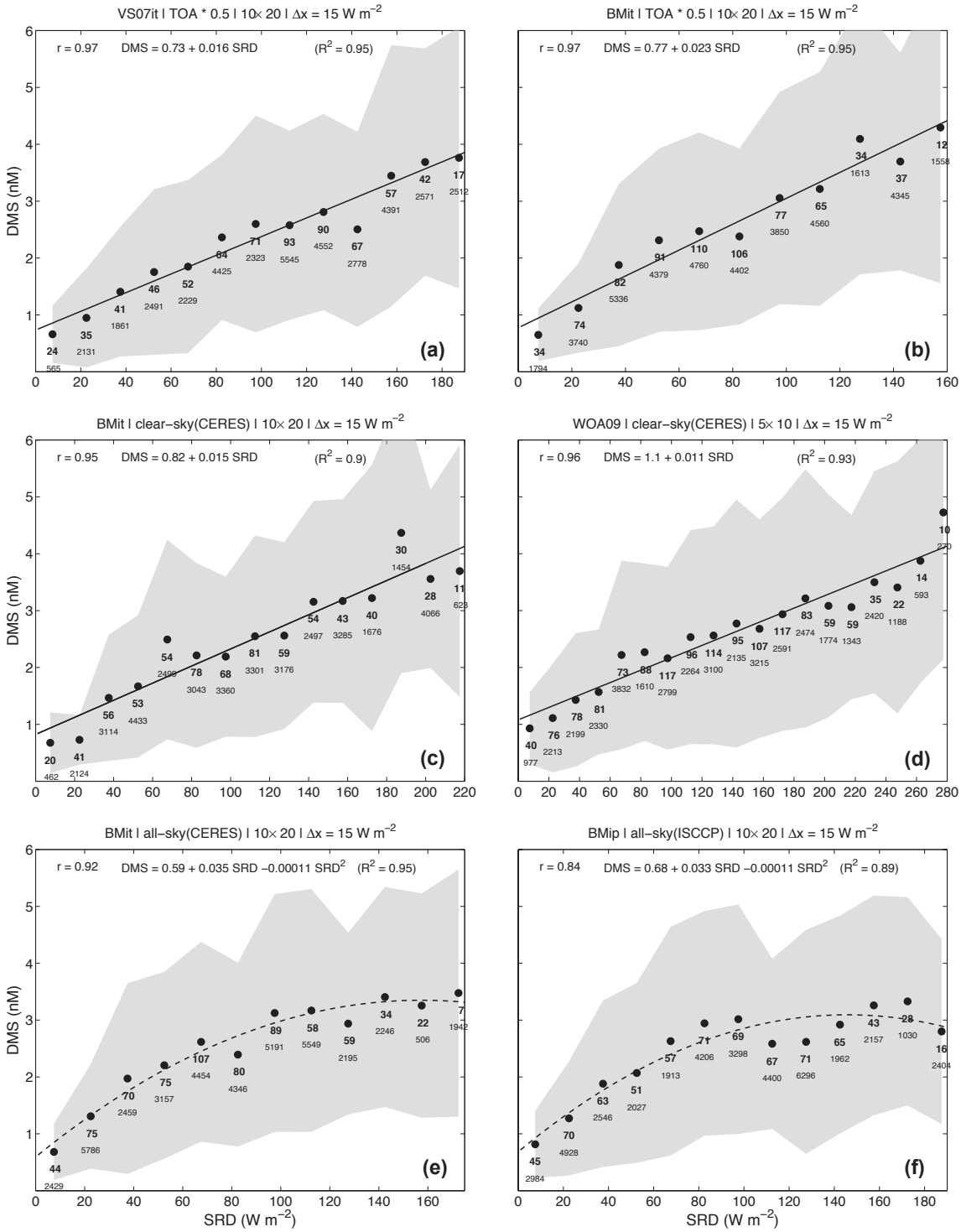

Figure 2.5: Regression of DMS on SRD for the VS07 algorithm. (Continued on the following page)

Figure 2.5: Similar illustration was used as in Vallina and Simó (2007)/Lana et al. (2012) in order to better compare results of this study with previous studies. As for the original VS07 approach, DMS and SRD are first averaged by grid size (10° latitude by 20° longitude) and then binned by SRD intervals of 15 W m^{-2}. The gray shaded area shows the standard deviation of the averages (black dots). Under each data point, the upper number represent the amount of 10°×20° means and the lower number represents the amount of original DMS samples included. Different panels show regression corresponding to different sources: Top panels (a, b) show regressions using half of top-of-the-atmosphere (TOA) for I_0 with (a) MLD as in original VS07 (VS07it: definition criterion of a 0.1℃ departure with respect to the temperature at 5 m) and (b) MLD by de Boyer Montegut (BMit: definition criterion of a 0.5℃ departure with respect to the temperature at 10 m). Middle panels (c, d) show regressions using clear-sky surface irradiance by CERES for I_0 with (c) MLD by BMit and (d) MLD by WOA 2009 (definition criterion of depth at which density is 0.125 kg m^{-3} greater with respect to surface). Bottom panels (e, f) show regressions using all-sky surface irradiance by (e) CERES and (f) ISCCP for I_0 with (e) MLD by BMit and (f) MLD by de Boyer Montegut (BMip: definition criterion of 0.03 kg m^{-3} departure with respect to value at 10 m depth). When using all-sky surface irradiance for I_0 (e, f), the relationship is nonlinear, such that a quadratic (instead of a linear) regression is shown in panels e and f.

Miles et al. (2009) used observational data from the Atlantic Meridional Transect (AMT) program to test the VS07 relationship between DMS and SRD. Besides SRD, Miles et al. also derived an ultraviolet radiation dose, restricting surface irradiance to a narrower spectral band corresponding to UV-A (315-400 nm). The proposed relationship between DMS and UVRD uses a cloud-adjusted irradiance field and considers only UV radiation, which is believed to affect DMSP production in phytoplankton. However, the new expression did not improve the correlation with Miles et al.'s AMT data compared to the SRD methodology of Vallina and Simó (2007).

This study used the same methodology as described in Vallina and Simó (2007) to derive DMS distributions from the MI09 approach. The only difference was the use of a UVA climatology instead of total solar irradiance. Furthermore, a universal attenuation coefficient of $k = 0.10$ m^{-1}, appropriate for UVA under oligotrophic conditions (Miles et al., 2009), was used. As a global field of I_0, the NASA TOMS UVA surface irradiance product was used. As with VS07, the present study considered different MLD fields to obtain relationships between DMS and UVRD (Figure 2.6).

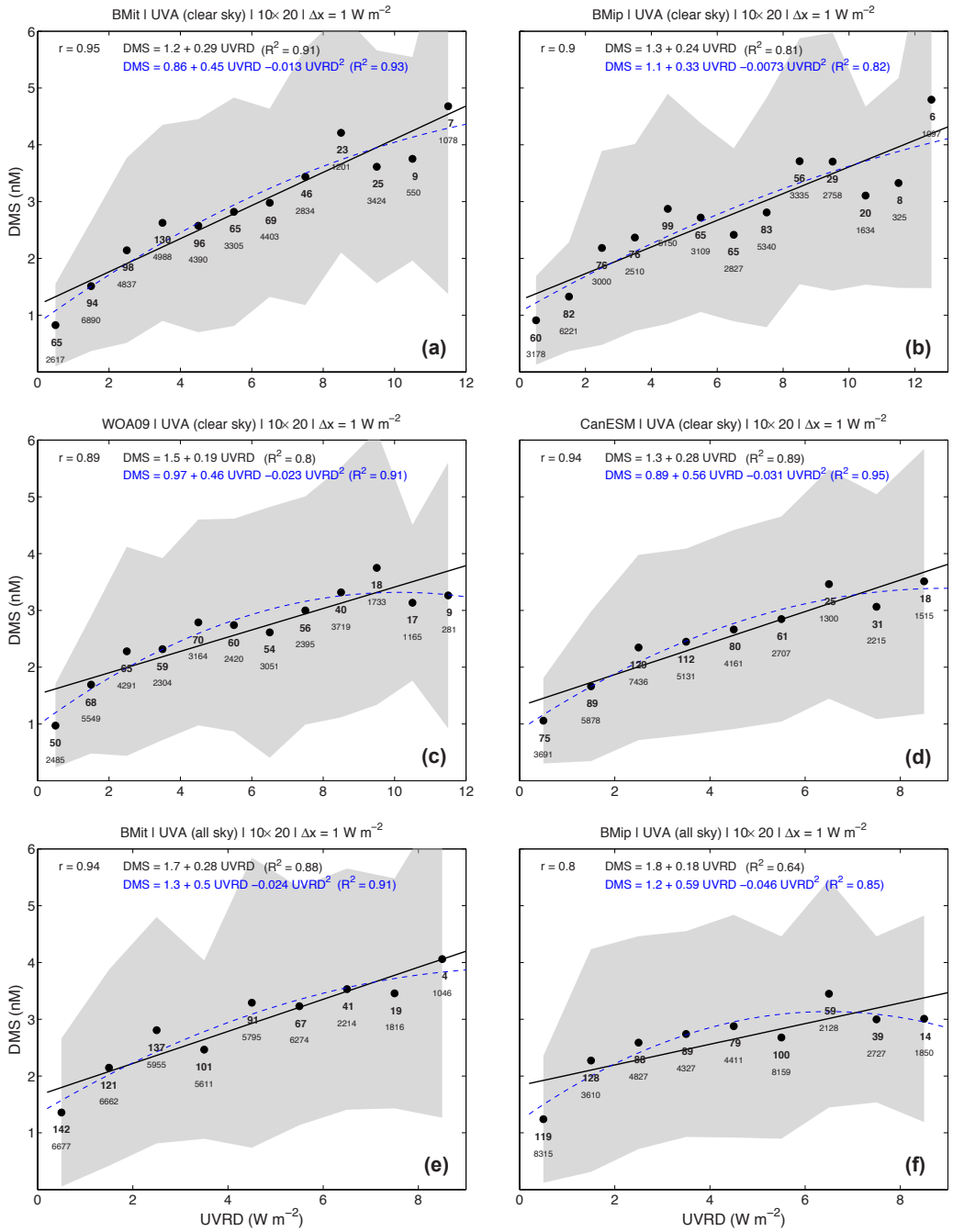

Figure 2.6: Regression of DMS on UVRD for the MI09 algorithm. Illustration is as in Figure 2.5. DMS and UVRD are first averaged by grid size (10° latitude by 20° longitude) and then binned by UVRD intervals of 1 W m^{-2}. Different panels show regression corresponding to different sources. The upper four panels show regression using clear-sky UV-A irradiance with (a, b) MLD by de Boyer Montegut (BMit and BMip); (c) WOA 2009 and (d) CanESM. The bottom two panels show regression using all-sky UV-A irradiance with MLD by (e) BMit and (f) BMip.

2.2.3 Methodology used for the intercomparison and evaluation of DMS climatologies

2.2.3.1 Taylor diagram

Taylor diagrams (Taylor, 2001) are a convenient way to compare all available DMS reconstruction simultaneously with a reference dataset (in the present case, L10 or the observations). Taylor diagrams were computed for the complete global spatiotemporal distributions of DMS concentration. In a Taylor diagram, each dataset (reference and test) is represented by a single point. The radial distance (i.e., the distance from the origin) of the point on the diagram corresponds to the standard deviation of the dataset, while the angle relative to the vertical corresponds to the correlation coefficient. The centered root-mean-square (RMS) error corresponds to the distance between the points corresponding to the reference and test datasets (Taylor, 2001).

2.2.3.2 Mapping temporal correlations

To analyze temporal correlations between reconstructed DMS distributions and the observation-based L10 climatology, global maps of correlations between seasonal cycles were constructed. This revealed information about regional differences, such as where specific reconstructions were consistent with the L10 climatology, and where they were not. The procedures described in Lana et al. (2012) and Vallina et al. (2007a) were followed, with slight modifications. Global distributions of Spearman's rank correlation coefficient (ρ) were derived by taking the gridded data in a 5°×5° window and calculating the corresponding ρ for each 1°×1° grid point. The rank coefficient ρ was used instead of the more usual Pearson coefficient, because the seasonal cycles are not normally distributed. Rather than evaluating temporal correlations for each individual grid point, a perimeter of 5°×5° was chosen. Thus, for each grid point within a monthly map, 24 surrounding points were used in the evaluation along with the central point. This helped to focus the analysis on larger-scale variations, and minimize the influence of small-scale differences. For 12 monthly fields, 300 data points (12×25) were used to calculate ρ for individual 1°×1° grid points. Along the coast, points were omitted which had more than 5 grid points of land mask.

2.2.3.3 Binning, averaging, and filtering DMS data

For comparison to DMS observations, the gridded DMS fields were sampled at the corresponding location and month. When comparing gridded products representing mean data for a given climatological month, differences in scale and resolution need to be taken into account. The gridded products are not directly comparable to the raw observations, as the gridded products do not resolve the fine-scale temporal and spatial variability of the observational data. To account for differences in spatial and temporal structure, observations were binned by month in 5°×5° grid boxes, and the gridded DMS products were sampled monthly as 5°×5° spatial averages at the locations of the raw observations. Abnormally extreme raw data ($>$ 100 nM), such as data arising from an algal bloom, were not considered representative of the regional mean state and removed from the analysis before averaging. Grid averages that consisted of less than three measurements were flagged for optional filtering. When averaging the gridded fields, 5°×5° domains which contained more than 10 points associated with land mask were excluded from further analysis.

For comparison of annual cycles (Section 2.3.4.3), control regions were chosen that have (near) complete seasonal coverage of observational data. For each region, spatial averages of available observations, L10 and reconstructed DMS were computed for each month of the year. When averaging observational data by month, the available samples were first averaged for each 5°×5° grid within the control area, instead of computing a single average for the entire region. This was done because discrete DMS samples from the GSS database are usually distributed non-uniformly within the assigned control regions. A single mean for the observational data in a given region could be dominated by a few clusters of data points, and would not be representative of the whole region.

2.3 Results

2.3.1 Observationally-based climatologies

The observation-based climatologies (K99, K00, and L10) are produced using similar methodologies, with L10 making use of the largest set of observations (Table 2.1). Nonetheless, similarities and differences among the three climatologies are evident from their annual mean spatial distributions and zonal mean distribution in latitude and time (Figure 2.7).

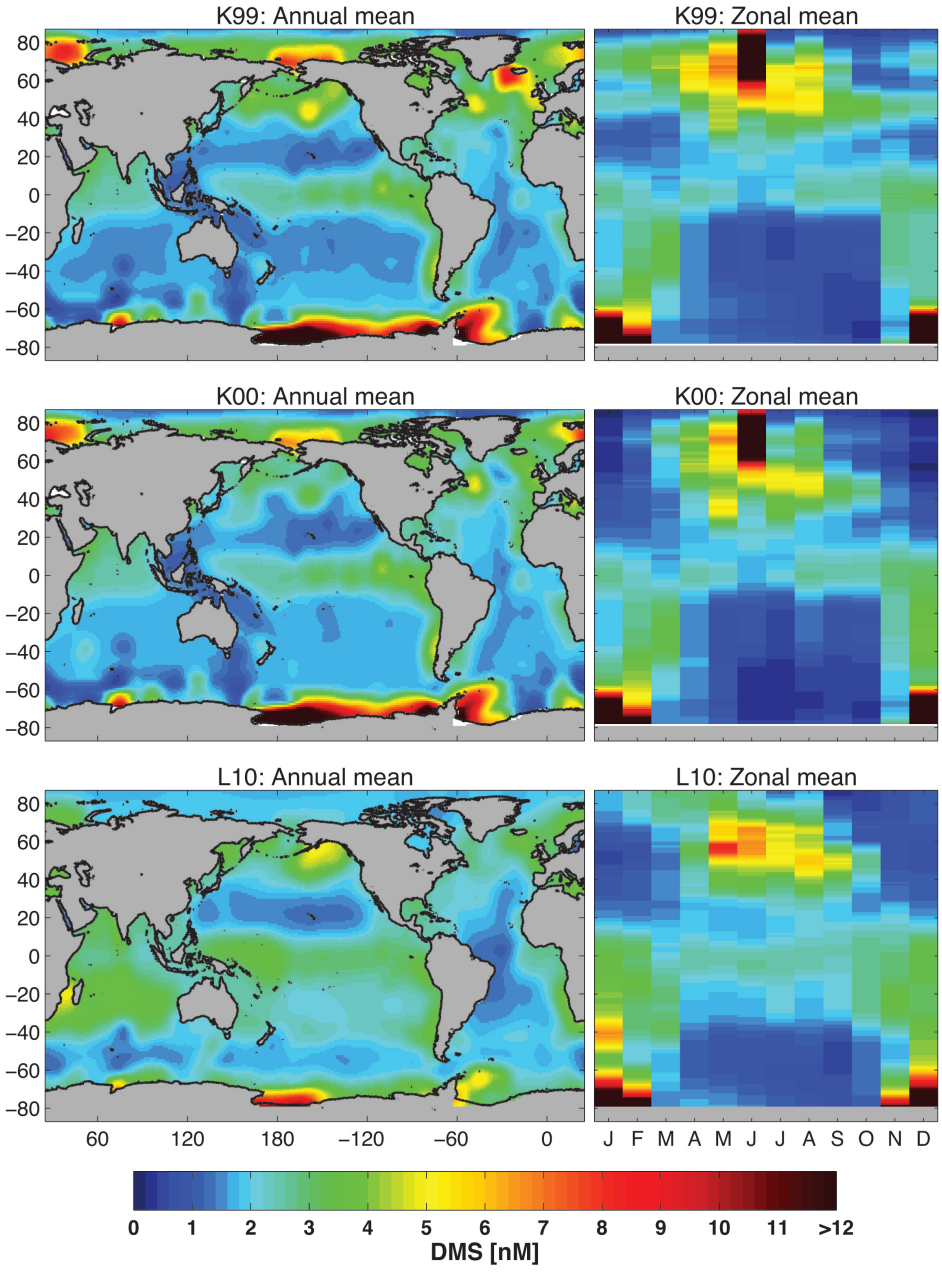

Figure 2.7: Global map of annual mean DMS concentration (nM) and corresponding zonal mean annual cycle for each observation-based climatology: K99 (upper panel), K00 (middle panel) and L10 (lower panel). The colour scale has an upper limit of 12 nM for illustrative purposes. Note that there are regions in the high latitudes where annual mean DMS concentration exceeds 12 nM.

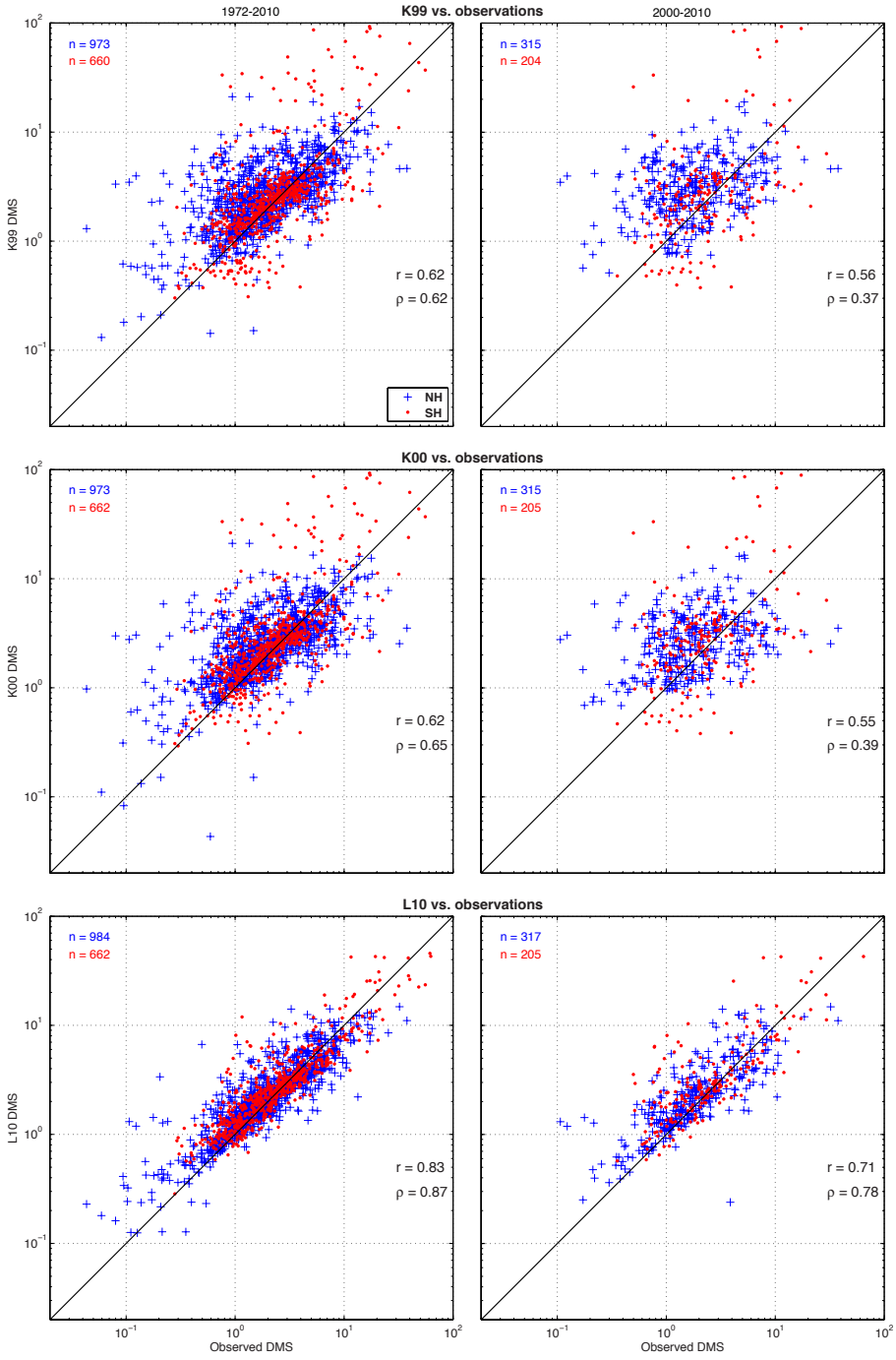

Figure 2.8: Scatter plots (log scale) of climatology versus raw observed DMS concentration (nM). In-situ DMS concentration samples were averaged in monthly 5°×5° bins and compared to the corresponding 5°×5° monthly averaged value of each climatological DMS field. Red dots represent data from the Southern Hemisphere and blue crosses represent data from the Northern Hemisphere.

The differences between K99 and K00 are minor since only slight adjustments from K99 were undertaken in constructing K00. Both climatologies have the same basic spatial structure (Figure 2.7). K00 included a few updates in terms of data additions from the Atlantic (Belviso et al., 2000) and Indian Oceans (Sciare et al., 1999). The main change resulted from a modification in the interpolation scheme that better represents wintertime DMS concentrations for high latitude provinces (Kettle and Andreae, 2000). The effect of the adjustment is evident in the clear reduction in the annual mean DMS concentration in the North Atlantic and North Pacific, as well as a slight increase in the Southern Hemisphere. The change in the temporal interpolation scheme is also evident in the enhanced seasonality in K00 relative to K99, as illustrated in the latitude–time plot of K99 and K00 (Figure 2.7). The high northern latitudes show lower DMS concentration during the winter months in K00 as compared to K99. In turn, the Southern Hemisphere in K00 shows higher DMS concentration in December.

On the other hand, the differences between K00 and L10 are rather large (Figure 2.7). The methodology used to produce the fields is the same, but the inclusion of about 10 more years of data has changed the temporal and spatial pattern significantly. In particular, DMS concentrations in the Southern Hemisphere differ due to addition of many new data (Lana et al., 2011). Annual mean DMS concentration is nearly twice as large in the southern Indian Ocean and Western Equatorial Pacific in L10 compared to K00. There is higher annual DMS concentration in the northeast Pacific, whereas the annual mean in the North Atlantic is reduced in L10 compared to K00. A detailed description of the improved spatial and temporal patterns of L10 compared to K00 is presented in Lana et al. (2011). Since L10 represents a distinct improvement from K99 and K00 (Figure 2.8), it can be regarded as the best available choice for the observationally-based DMS climatology.

2.3.2 Sensitivity of parameterized DMS to different input fields

Before comparing the DMS distributions from the available empirical algorithms with the observation-based climatology and models, it is important to consider the robustness of each individual algorithm to variations in its input fields. The questions to be addressed are: Which algorithm tends to be more sensitive to which input field? Are the differences resulting from different inputs comparable to the differences among different functional forms (e.g., SD02 vs. AT04)? To what extent does reestimation

of the algorithm's coefficients with new data change the output? As GCM fields are biased relative to observations, the sensitivity of simulated DMS fields to input fields is particularly important with regard to the implementation of these algorithms in global models.

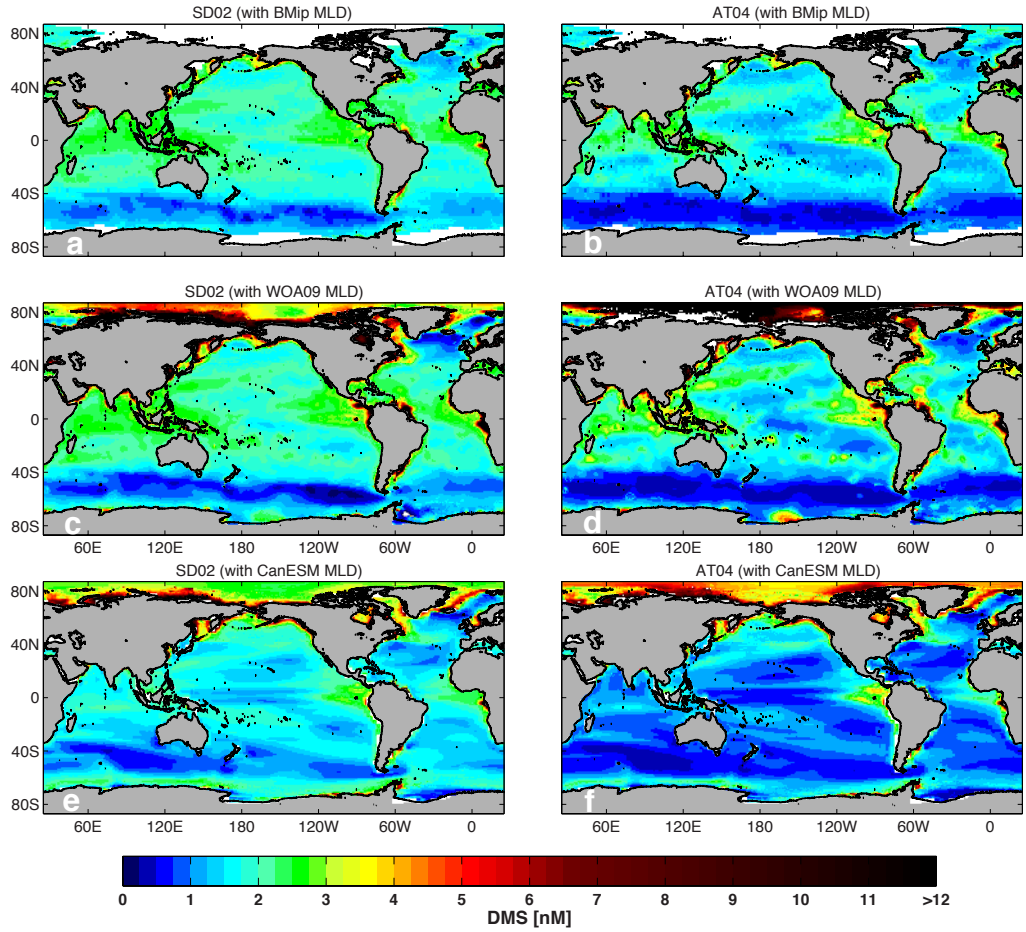

Figure 2.9: Global maps of the annual mean surface concentration of DMS (nM) computed with the SD02 (a, c, e) and AT04 (b, d, f) algorithms with different MLD products: (a, b) BMip; (c, d) WOA09 and (e, f) CanESM.

Global climatologies of chlorophyll are based on satellite ocean colour. Since such remotely-sensed chlorophyll products are fairly well constrained (McClain, 2009), few differences among the different products can be expected. For the algorithms that have chlorophyll as an input field (AN01, BE02, SD02, and AT04), three different chlorophyll fields were used, which are not entirely independent of each other: (1) a SeaWiFS chlorophyll climatology (1998-2004); (2) monthly fields of SeaWiFS chlorophyll from

2000 to 2007; and (3) a composite of SeaWiFS, MODIS-Aqua, and Terra (1998-2012). For any particular algorithm, the resulting DMS fields from the different climatological fields were very similar. The algorithm with the greatest sensitivity to chlorophyll is BE04, for which the global mean varies from 1.55 to 1.76 nM among the three fields (Table 2.3). SD02 and AT04 have greater sensitivity overall, although this is not due to chlorophyll.

Biases in GCM-based chlorophyll are expected to be larger than observationally based values, which can lead to greater differences in DMS concentration. The exploration of DMS sensitivity to differences in simulated chlorophyll distributions was not within the scope of this study. However, this study considered SD02-simulated DMS from HadOCC (Collins et al., 2011) and AU02-simulated DMS from IPSL-OCCM2 (Aumont et al., 2002), both use simulated chlorophyll concentrations. Comparisons between SD02 derived DMS from satellite chlorophyll fields and HadOCC as well as between AU02 derived DMS from satellite chlorophyll and IPSL-OCCM2 is discussed in Section 2.3.3.

Low sensitivity was observed in AN01 when using different surface irradiance products. In SD02, AT04, VS07, and MI09, algorithm sensitivity was explored for different MLD products, both model derived (CanESM2) and observation-based (WOA 2009; de Boyer Montégut et al., 2004). In general, the sensitivities of the algorithms to different MLD input fields were fairly low. Among the observation-based MLD climatologies (WOA 2009; de Boyer Montégut et al., 2004) especially in SD02 and AT04, the main deviations were in the variability of the output fields (Table 2.3). The largest differences occurred over the continental shelves, and mostly in the Northern Hemisphere summer (Figure 2.9). Those regions are generally associated with high chlorophyll concentrations, so small changes in MLD result in large changes of the chlorophyll to MLD ratio and therefore of the predicted DMS. While the MLD field in Arctic and coastal regions derived from WOA 2009 temperature and salinity is strongly influenced by the strong salinity gradients that occur due to strong fluxes of freshwater, these features are not apparent in the MLD field from de Boyer Montégut et al. (2004). When the continental shelves are disregarded, annual mean fields of DMS concentration are more consistent among the different MLD input fields (Figure 2.9).

Not surprisingly, the differences in the DMS fields using model simulated MLD were greater compared to different observation-based data products (Figure 2.9), as spatial patterns of modelled MLD fields are less constrained than those based on

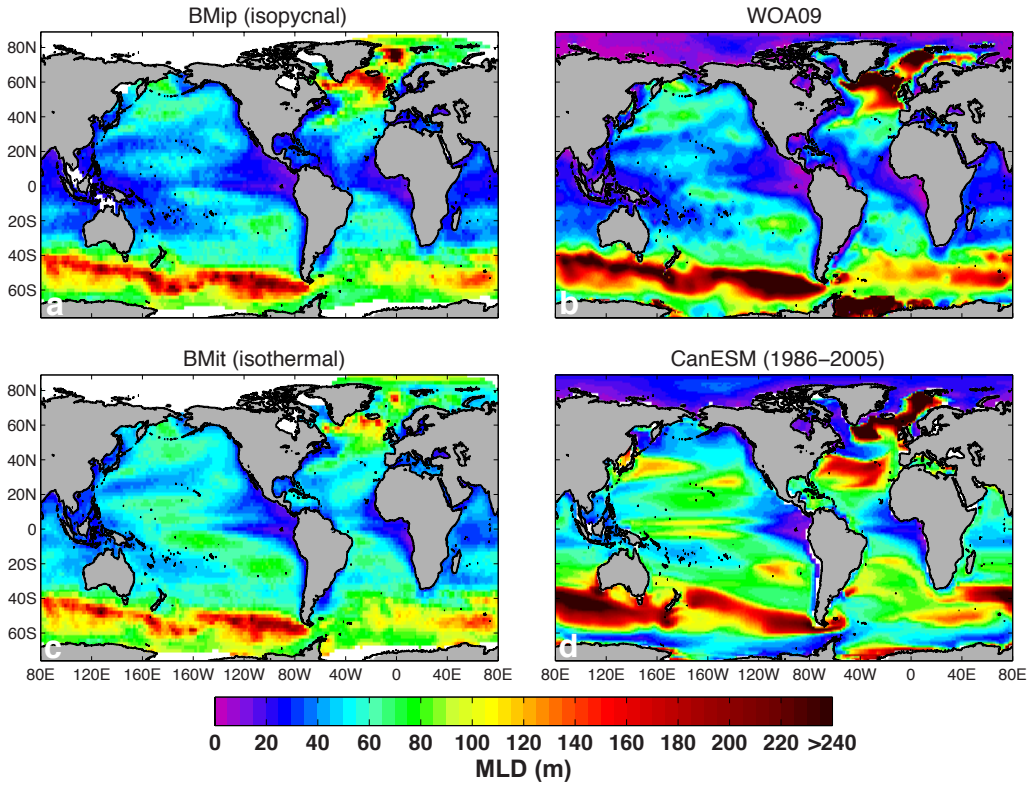

Figure 2.10: Various MLD products, observation-based (a, b, c) and model (d). Panels a, b and c represent MLD distributions derived from profile data (BMip, BMit and WOA09). Panel d represent simulated MLD from a global ocean model (CanESM).

observations. Figure 2.10 illustrates that differences between models are larger than differences between observational MLD products or different criteria (density versus temperature). When implementing MLD-based empirical algorithms for DMS into global ocean models, it should be considered that inter-model differences in simulated MLD tend to be large (Doney et al., 2004). In general, it can be assumed that inter-model differences in chlorophyll, nitrate, and MLD might generate differences in the DMS fields comparable in size to the differences between the observational and model fields.

Considering VS07, Lana et al. (2012) showed that the relationship between DMS and SRD is robust to different DMS data sources. The present study confirmed this robustness using different MLD products, as the coefficients of the regression line between SRD and DMS differed only marginally (Figure 2.5). Different irradiance fields were used to derive the SRD distribution: satellite-derived climatologies (CERES,

ISCCP) and top-of-atmosphere irradiance (Brock, 1981) reduced by 50% as in Vallina and Simó (2007). Interestingly, when all-sky surface irradiance fields obtained by CERES or ISCCP (which account for clouds) were used, binned SRD showed a more nonlinear relationship with binned DMS than when using the fields derived by equations from Brock (1981) (Figure 2.5 e and f). This finding suggests that the variation in MLD, rather than the variation in SRD, directly controls DMS, whereas irradiance helps to account for the general DMS seasonality (Miles et al., 2009). Similarly, for MI09, the linear relationship between UVRD and DMS is only observed when using clear-sky, as opposed to cloud-adjusted, surface UVA irradiance field (Figure 2.6).

For the rest of this study only one DMS concentration field is used for a given algorithm. A preliminary correlation analysis with all available input fields for AN01, BE04 (Table 2.4), SD02, AT04 (Table 2.5), VS07 (Table 2.6) and MI09 (Table 2.7) has been undertaken to evaluate the different combinations of input fields. For most algorithms, the differences in correlations are very small. For each algorithm, the DMS concentration field with the greatest Spearman correlation was chosen for further use in the intercomparison. The only exception is SD02 and AT04 for which the BM_{ip} MLD field was used to be consistent with previous studies.

Table 2.4: Correlations of different DMS fields derived from AN01 and BE04 with observations. Three different chlorophyll fields were used to obtain the different DMS fields. Correlations between observations and the original DMS fields (as presented in the original publication or obtained from the author) are also included. Observations were averaged in monthly $5^\circ \times 5^\circ$ bins. Correlation is given as Spearman correlation coefficient (and Pearson correlation coefficient in brackets).

Chlorophyll	AN01	BE04
merged climatology	0.46	-0.03
	(0.47)	(0.12)
SeaWiFS climatology	0.45	0.13
	(0.52)	(0.28)
SeaWiFS monthly fields	0.44	0.09
	(0.49)	(0.24)
original (as published)	0.40	0.15
	(0.46)	(0.31)

Table 2.5: Correlations of different SD02 and AT04 DMS fields with observations given different MLD fields. Observations were averaged in monthly $5° \times 5°$ bins. Correlation is given as Spearman correlation coefficient (and Pearson correlation coefficient in brackets).

MLD fields	SD02	AT04
BM_{it}	0.41	0.42
	(0.19)	(0.22)
BM_{ip}	0.35	0.36
	(0.19)	(0.22)
WOA09	0.26	0.26
	(0.08)	(0.03)
CanESM	0.25	0.25
	(0.24)	(0.19)

Table 2.6: Correlations of different VS07 DMS fields with observations. Observations were averaged in monthly $5° \times 5°$ bins. Correlation is given as Spearman correlation coefficient (and Pearson correlation coefficient in brackets).

	BM_{it}	$VS07_{it}$	BM_{ip}	WOA09	CanESM
TOA×0.5	0.49	0.45	0.46	0.38	0.40
	(0.27)	(0.21)	(0.24)	(0.14)	(0.31)
CERES (clear-sky)	0.50	0.45	0.47	0.39	0.41
	(0.28)	(0.22)	(0.25)	(0.15)	(0.32)
CERES (all-sky)	0.44	0.38	0.40	0.33	0.40
	(0.21)	(0.15)	(0.18)	(0.08)	(0.26)
ISCCP (all-sky)	0.43	0.37	0.39	0.33	0.40
	(0.19)	(0.14)	(0.16)	(0.08)	(0.26)

Table 2.7: Correlations of different MI09 DMS fields with observations. Observations were averaged in monthly $5° \times 5°$ bins. Correlation is given as Spearman correlation coefficient (and Pearson correlation coefficient in brackets).

	BM_{it}	$VS07_{it}$	BM_{ip}	WOA09	CanESM
UVA (clear-sky)	0.46	0.41	0.43	0.35	0.40
	(0.20)	(0.14)	(0.17)	(0.09)	(0.28)
UVA (all-sky)	0.37	0.32	0.34	0.30	0.39
	(0.08)	(0.03)	(0.05)	(0.01)	(0.21)

2.3.3 Spatial and temporal variations in the given DMS reconstructions

Figure 2.11 shows the annual mean fields of DMS from L10 along with those estimated by seven algorithms. The spatial pattern of annual mean DMS concentration fields show substantial differences from each other. However, some fields are clearly alike due to similarities in the algorithms and input fields. General similarities in the global distribution of annual mean DMS concentrations are seen between SD02 and AT04, as well as VS07 and MI09, all of which include MLD as a key parameter (Figure 2.11). Unlike SD02 and AT04, VS07 and MI09 do not show enhancement around the coastlines because they do not include chlorophyll as an input variable.

The annual mean DMS concentration field from AN01 shows patterns distinct from other reconstructions and primarily reflects the spatial pattern of chlorophyll and nitrate (Figure 2.11). Calculated DMS concentration increases with chlorophyll, irradiance, or nitrate and is uniform over large areas of the open ocean. High concentrations are mostly associated with high chlorophyll concentration, while many regions of low concentration correspond to regions with minimal nitrate concentrations. Large regions of the surface ocean in the tropics and subtropics are low in productivity, nitrate and chlorophyll (e.g., McClain et al., 2004). The original algorithm of Anderson et al. (2001) assigned a fixed minimum DMS concentration of 2.29 nM, resulting in vast regions of constant DMS concentration and relatively little spatial and temporal variability (Belviso et al., 2004a). The DMS field resulting from the updated AN01 algorithm discussed in Section 2.2.2.1 has no baseline value and provides more spatial variation (Figure 2.11).

Similar to AN01, BE04 estimates DMS concentration as a function of chlorophyll. However, since its functional form is very different from AN01, the annual mean fields and the seasonal variations, are very different from AN01 (Figures 2.11 and 2.12). BE04 generally predicts lower DMS than AN01 in coastal and other highly-productive regions. On the other hand, the subtropical regions, such as the Sargasso Sea and South Indian Ocean, have higher DMS concentration in BE04 relative to AN01 (Figure 2.11).

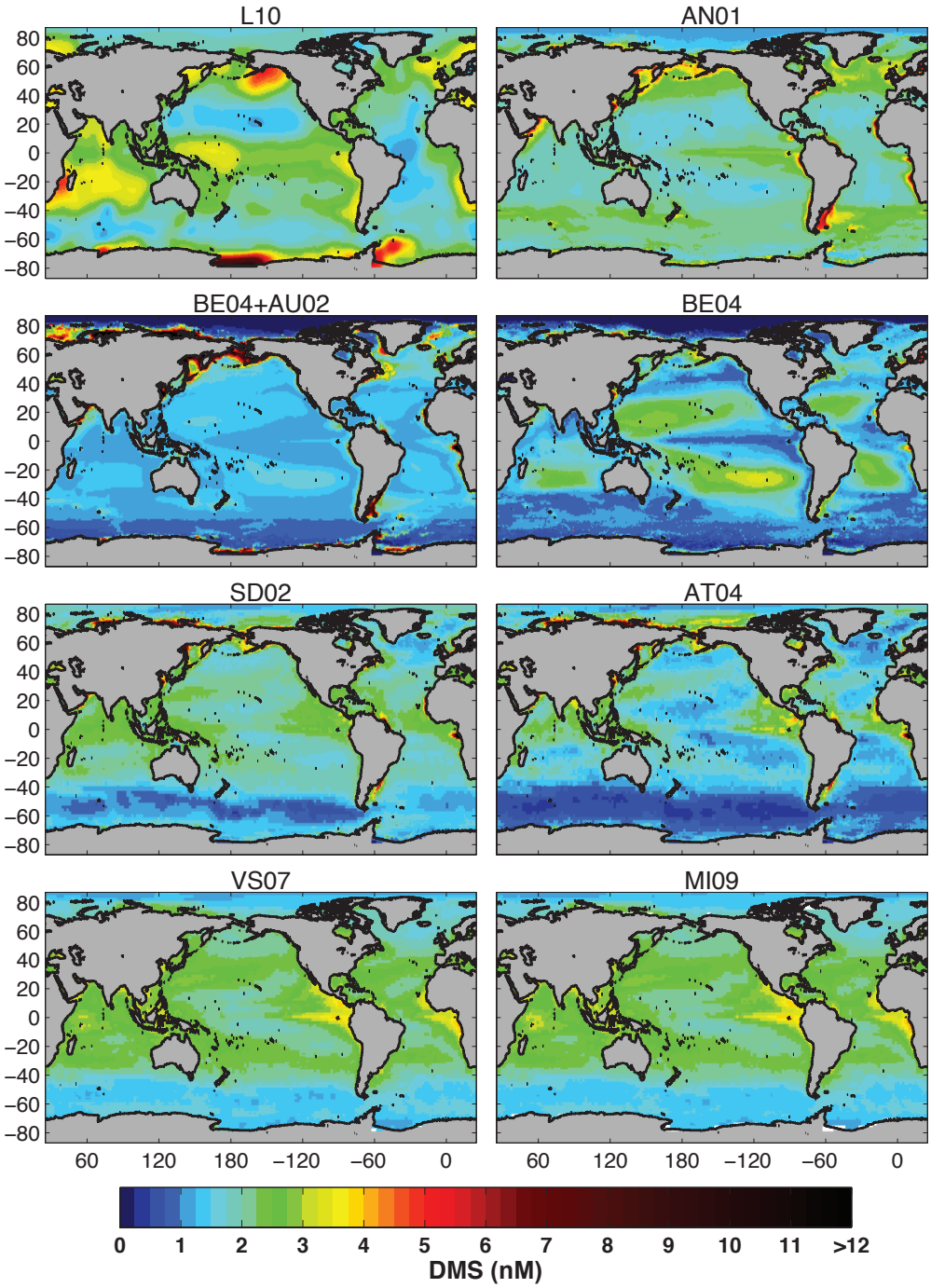

Figure 2.11: Global maps of the annual mean surface concentration of DMS (nM) from (a) L10 climatology, (b) AN01, (c) BE04+AU02, (d) BE04, (e) SD02, (f) AT04, (g) VS07 and (h) MI09 parameterizations. "BE04+AU02" indicates a combination of BE04 and AU02 algorithm: The Fp-ratio was derived using formulations as in BE04, while DMS concentrations was calculated with AU02.

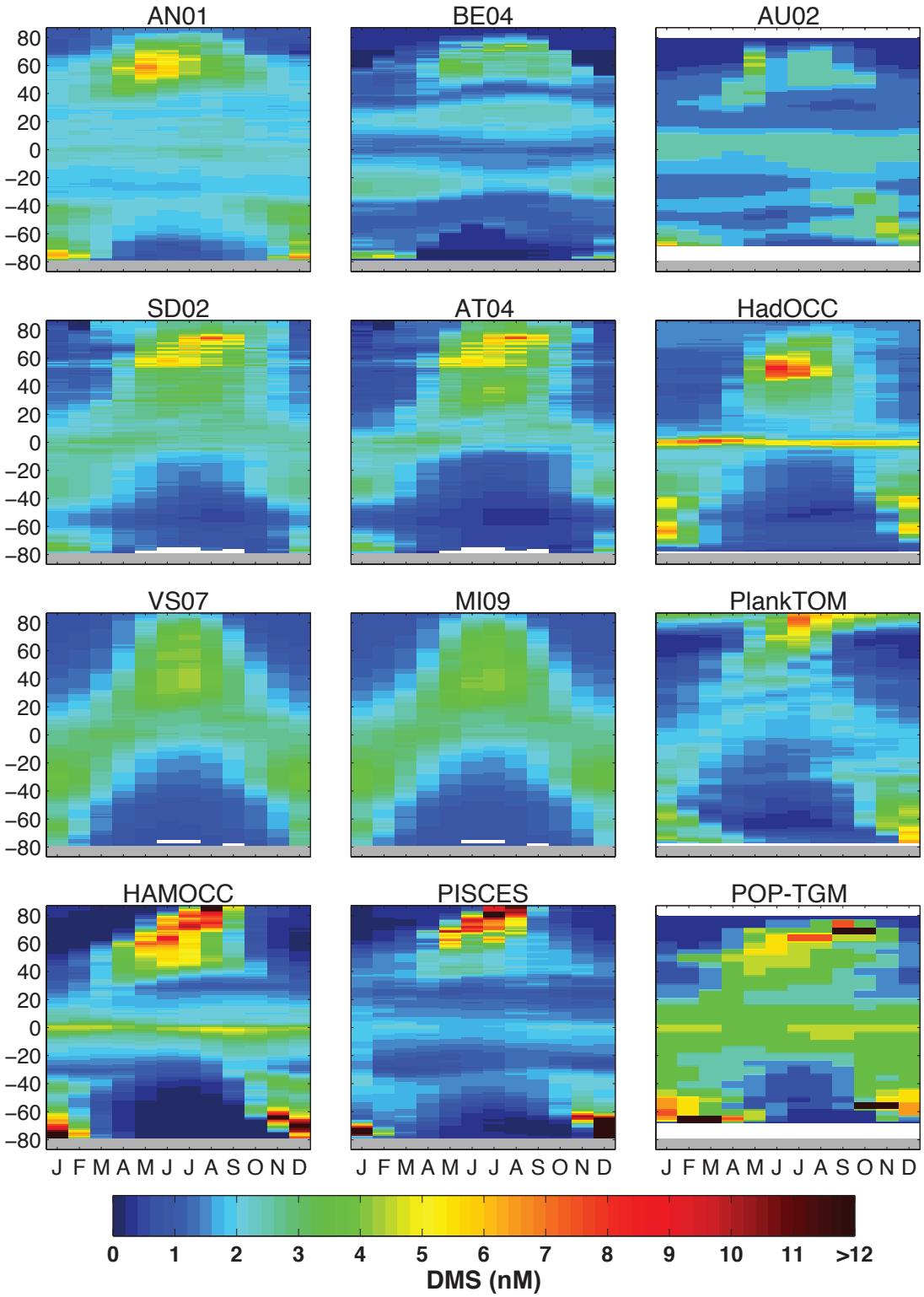

Figure 2.12: Latitude-time plots of the sea-surface concentration of DMS. For latitude-time plots of the observation-based climatologies see Figure 2.7.

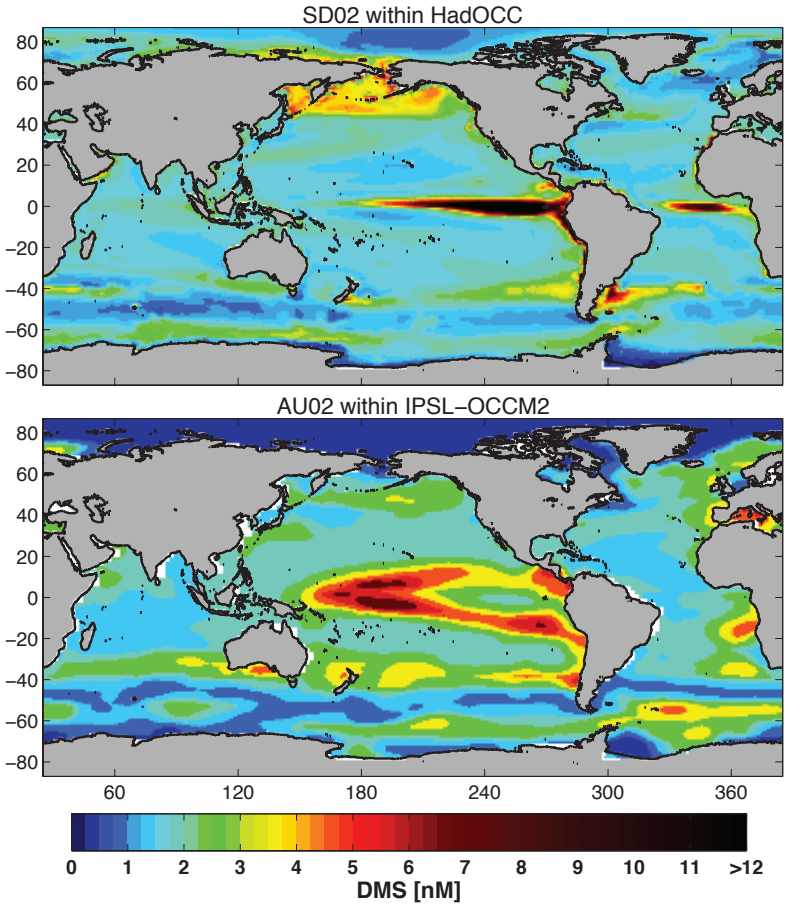

Figure 2.13: Global maps of annual mean surface concentration of DMS (nM) from the two diagnostic models (i.e., DMS based on algorithms implemented in a model).

Comparison of the different algorithms show that depending on how the DMS is parameterized, DMS distributions differ substantially in spatial and temporal structure (Figure 2.11 and 2.12). GCM-based DMS fields (Figure 2.13 and 2.14) also differ greatly from each other and do not share many features in common with L10 or empirically-derived DMS fields. It is striking how different the observationally-based fields of SD02 (Figure 2.11) are from the model output of HadOCC (Figure 2.13), which implements the SD02 algorithm in a global ocean carbon model. This difference illustrates the effect of model bias on the resulting DMS distribution. The same is true for the AU02 algorithm when it is implemented in the ocean carbon cycle model IPSL-OCCM2 versus the reconstruction with satellite-based chlorophyll. However, here the functional forms are slightly different, because the Fp ratio had to be derived form the chlorophyll fields using the formulation presented in Belviso et al. (2004b).

HAMOCC, PlankTOM, PISCES, and POP-TGM represent fully prognostic models

of DMS production and distribution. Some similarities are seen in the annual mean concentration fields of PISCES and HAMOCC (Figure 2.14), having patterns closer to general marine productivity than the ones from PlankTOM and POP-TGM. Inspection of the available reconstructions, demonstrates that DMS fields derived from algorithms with observationally-based input shows greatly reduced spatial variability relative to the observation-based climatologies (L10 and K00) and most of the GCM-based DMS fields (Figures 2.11, 2.13 and 2.14).

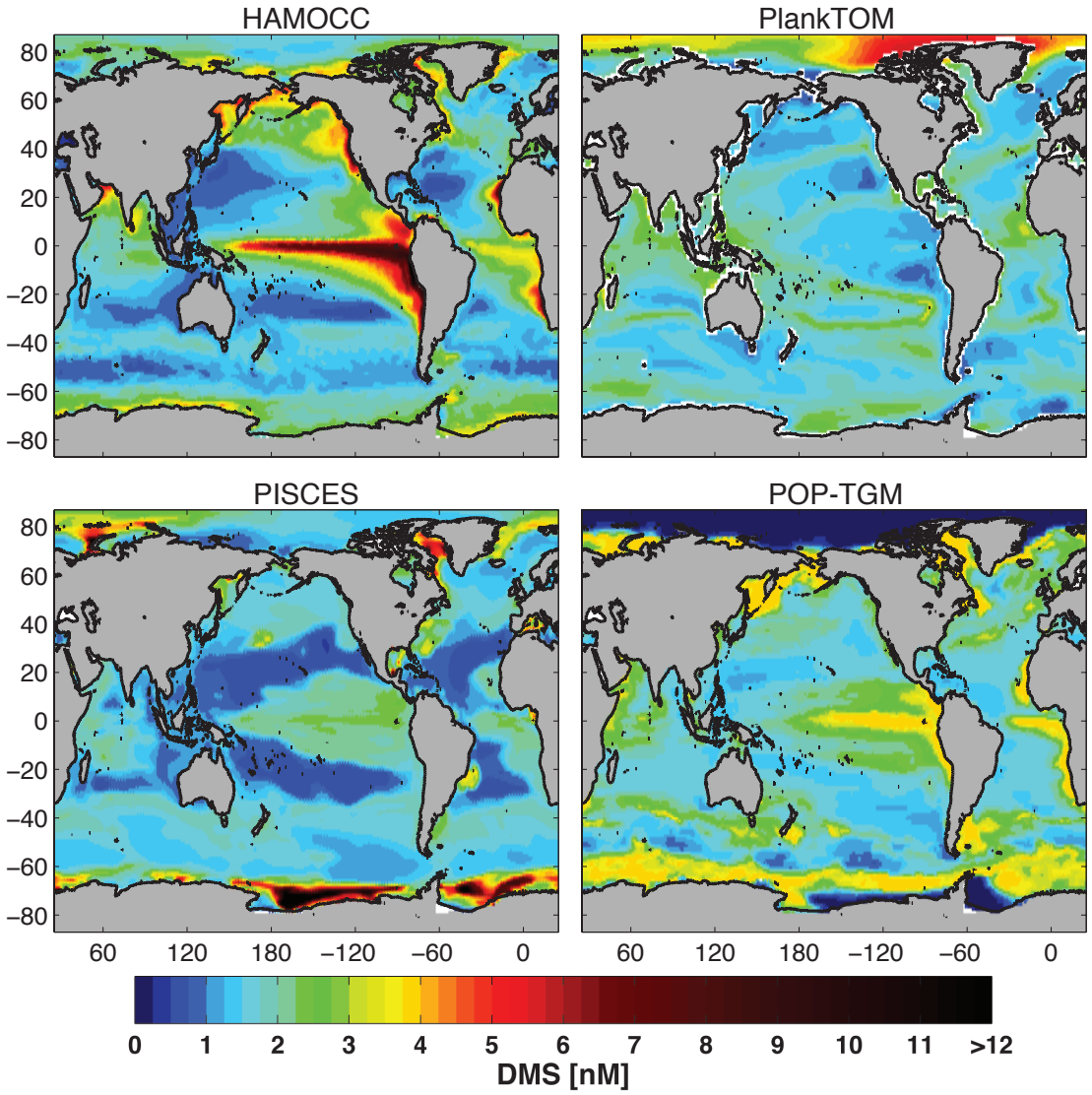

Figure 2.14: Global maps of annual mean surface concentration of DMS (nM) from four global models.

In many reconstructed or modeled fields, DMS concentrations in the eastern equatorial Pacific are enhanced (Figures 2.11, 2.13 and 2.14). MLD-derived climatologies (SD02, AT04, VS08, MI09, HadOCC) show low annual-mean concentrations in the North Atlantic relative to L10 (between 45°N to 60°N; Figures 2.11 and 2.13), likely because of the deep mixed layers in the winter and spring. The DMS fields of HAMOCC, PISCES, and PlankTOM, for which the source of DMS is not directly controlled by variation in MLD, also show lower DMS in that region. This is not the case with AN01, as the latter puts more weight on chlorophyll concentration.

A number of fields (L10, SD02, AT04, VS07, MI09, as well as model output from HadOCC and HAMOCC) show a band of low annual-mean DMS concentration between 40°S to 60°S (Figures 2.11, 2.13 and 2.14). This band is narrower in HAMOCC (Figure 2.14) and HadOCC (Figure 2.13) than in SD02, AT04, VS07 and MI09 (Figures 2.7 and 2.11). However, this band is not a consistent feature among reconstructions. AN01, for example, shows a pattern of generally elevated annual-mean DMS along this band (Figure 2.11). DMS concentrations in the Southern Ocean are lowest in AT04 and SD02, because of the strong dependence on MLD, which are deep in the Southern Ocean due to strong winds and surface heat loss. The Southern Ocean band of low DMS in mechanistic models (such as HAMOCC) (Figure 2.14) likely results from large MLD in concert with a predominance of diatoms (Cameron-Smith et al., 2011; Kloster et al., 2007). Elevated concentrations adjacent to Antarctica are present in some climatologies, but only PISCES estimates very high DMS concentrations similar to L10.

Considering the latitude–time plots (Figure 2.12), a greater seasonal variation in DMS concentrations at high latitudes compared to lower latitudes is a feature of most reconstructions and global simulations. Seasonal variation in the low to mid-latitudes is generally weaker, and its pattern varies greatly between the different reconstructions, and there is no general feature apparent among all the climatologies. The seasonal range varies substantially among the different reconstructions. In some of the prognostic models (e.g., HAMOCC, PISCES), concentrations can vary by almost two orders of magnitude over the year (Figure 2.12).

Patterns of seasonal variability of DMS in SD02, AT04, and VS07 are similar, although high-latitude summer concentrations in the Northern Hemisphere (NH) are much larger in SD02 and AT04 (Figure 2.12 and 2.15). AN01 exhibits high DMS concentration in the NH summer which is similar in its persistence compared to L10 (Figure 2.7 and 2.15). However, in AN01, there is a markedly smaller seasonal

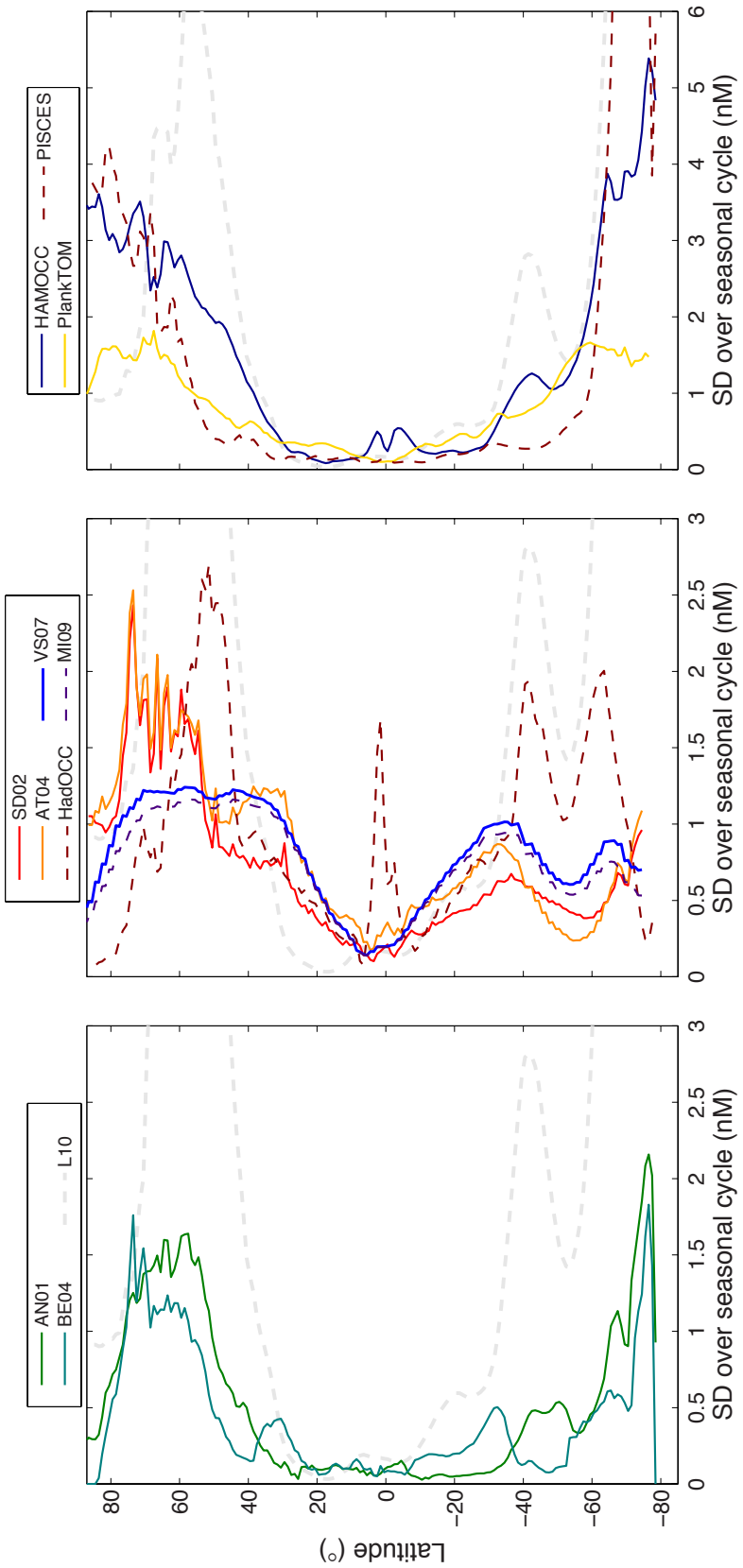

Figure 2.15: Zonal mean standard deviation of DMS distributions. Standard deviation (SD) over the seasonal cycle plotted against latitude. The SD of L10 is shown in all panels as a grey dashed line.

Table 2.8: Correlation matrix among DMS distributions. Correlation is given as Pearson correlation coefficient.

	L10	AN01	BE04	SD02	AT04	VS07	MI09	HadOCC	AU02	HAMOCC	PISCES	PlankTOM
L10	1.00											
AN01	0.43	1.00										
BE04	0.19	0.32	1.00									
SD02	0.30	0.36	0.40	1.00								
AT04	0.29	0.43	0.39	0.95	1.00							
VS07	0.45	0.32	0.41	0.62	0.61	1.00						
MI09	0.42	0.29	0.42	0.61	0.60	1.00	1.00					
HadOCC	0.31	0.32	0.10	0.33	0.33	0.51	0.50	1.00				
AU02	0.27	0.65	0.46	0.52	0.56	0.20	0.18	0.12	1.00			
HAMOCC	0.37	0.42	0.06	0.34	0.34	0.38	0.36	0.41	0.22	1.00		
PISCES	0.33	0.22	-0.01	0.11	0.12	0.11	0.07	0.05	0.12	0.42	1.00	
PlankTOM	0.31	0.16	0.01	0.33	0.32	0.35	0.30	0.17	0.09	0.46	0.31	1.00

variability, especially between 20°N and 40°N (Figure 2.12 and 2.15a). Globally, there is little seasonal variability between 40°S and 40°N in AN01 and BE04. Most other approaches show distinct seasonal variability in mid-latitude bands (between 20° and 40° N/S) and substantially less variability in the tropical latitudes (Figure 2.12 and 2.15). The constant moderate concentration in the tropics throughout the year is shared with the observational climatology L10 (Figure 2.7). BE04 shows a consistently low concentration, whereas HadOCC and HAMOCC show elevated DMS concentration throughout the year (Figure 2.12), with maximum concentrations in January to April and August to October. The only climatology where tropical latitudes are more seasonally variable is HadOCC (Figure 2.12 and 2.15) with maxima in spring and fall (Figure 2.12).

Table 2.8 confirms that none of the spatiotemporal distributions of DMS concentration strongly correlated with one another. Correlation is only high when approaches are similar. Correlation coefficients only exceed 0.60 when two models possess common key parameters, such as MLD in SD02 and VS07 (Table 2.8).

2.3.4 Assessing DMS reconstructions

2.3.4.1 Testing global fields of reconstructed DMS against the L10 climatology

Global space-time distributions Directly comparing gridded maps and zonal mean (latitude-time) plots allows a qualitative analysis of general patterns in the reconstructed distributions of DMS. As a more quantitative evaluation, the different fields can be compared together against a standard climatology using Taylor diagrams. Although it is not perfectly accurate, L10 is chosen as the standard climatology representing the spatial and temporal patterns most closely related to observations (Figure 2.8).

Figure 2.16 provides a concise demonstration that none of the parameterized (Panel A) or modeled (Panel B) DMS patterns match well globally with the L10 climatology. The prognostic models other than PlankTOM show similar or greater variability than L10. The older observation-based climatology (K00) also has a much greater variability than L10; this result shows how the incorporation of extra data has smoothed the interpolated DMS fields (Figure 2.7). All parameterized DMS distributions have lower variability than L10. Although the variability of SD02 and AT04 are close to L10, they demonstrate weak spatial correlation and high RMS error.

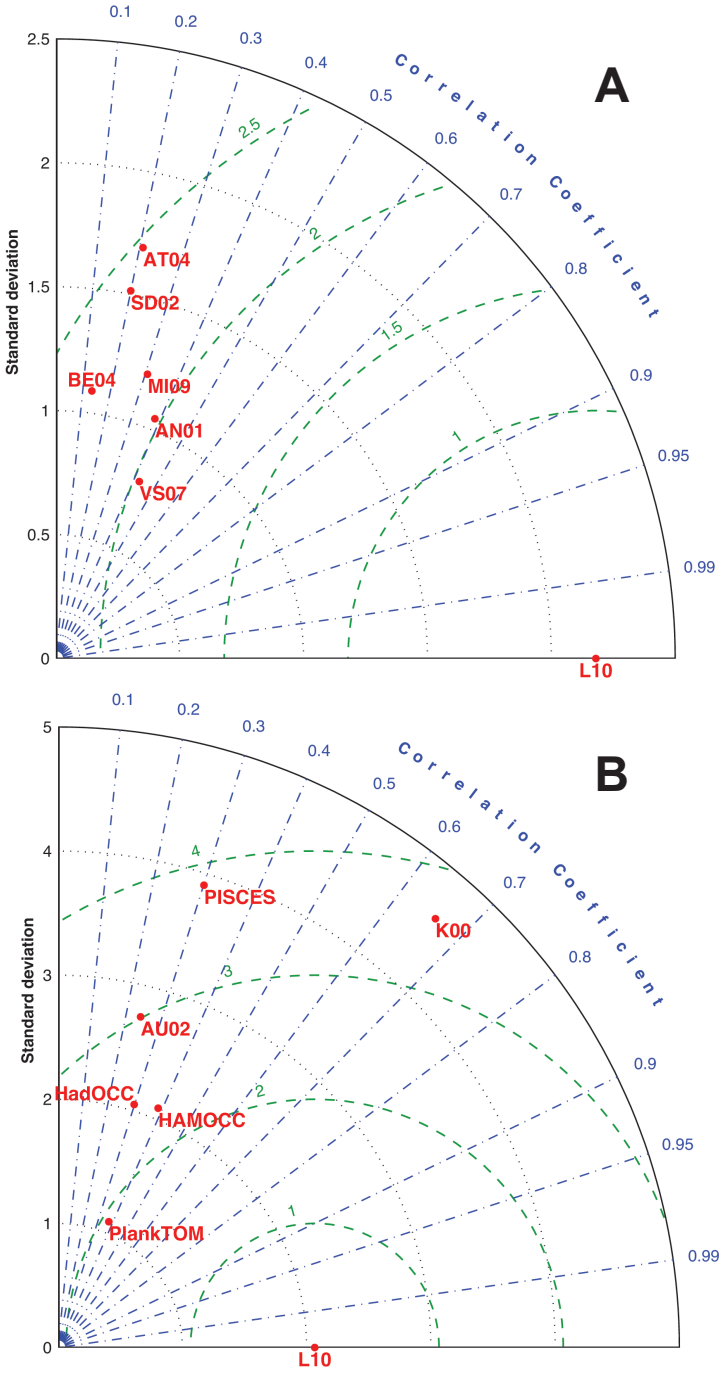

Figure 2.16: Taylor diagrams describing the total space-time variations of DMS concentration as obtained from 12 gridded data sets compared with L10, separated by ranges of variability. Panel A shows DMS concentrations estimated from empirical algorithms, which show generally low variability compared to L10. Panel B shows all remaining estimates including prognostic models and K00.

It can be argued that many features in L10 are based on localized observations that do not correspond to the monthly mean state and result in its relatively high spatial variability. Choosing only the low to medium concentration range of L10 (0 to 4.2 nM), corresponding to 90% of the data, and comparing it to the reconstructions improves the agreement in variance: most parameterized DMS fields now have variability similar to L10 (Figure 2.17). However, the correlations are still very weak. The only improvement can be seen with VS07 and MI09, which both improve by about 0.2 (compare Figure 2.16 Panel A with Figure 2.17). This indicates that the SRD regression accounts for variations in the medium concentration range. However, how important high concentrations are in determining the mean distribution remains unclear.

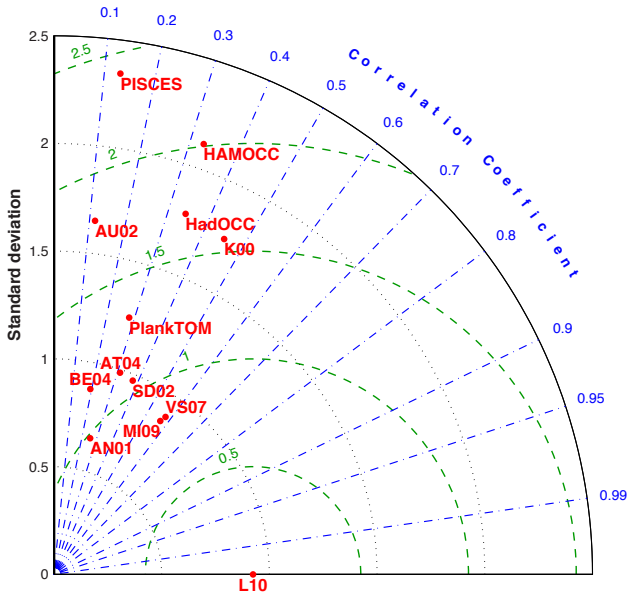

Figure 2.17: Taylor diagram as in Figure 2.16, but with L10 DMS only from 0 to 4.2 nM.

Seasonal cycles of global, hemispheric, and latitudinal means Seasonal cycles of DMS will now be considered globally, hemispherically, and in different latitude bands. The seasonal cycles of monthly global mean DMS concentration agree reasonably well in terms of overall magnitude (Figure 2.18a). Annual cycles of all parameterized DMS fields have a distinctly reduced seasonal range relative to those in the L10 climatology and simulated by GCMs. None of the approaches yields seasonal cycles with the same range as L10. Figure 2.18a shows that L10 produces a pronounced maximum in the time period between November to February which

is generally not reproduced by the parameterized DMS datasets. Although most DMS reconstructions and models generally capture the higher concentrations, it is much weaker than the maximum in the L10 dataset. The prognostic methods seem to produce a more realistic seasonal variation than the diagnostic data sets. The one reconstruction that comes closest to L10 global seasonality is HadOCC, which represents modeled DMS via the use of the SD02 parameterization. Additionally, the seasonal range in PlankTOM compared well to L10, but its global means are considerably lower compared to L10 global means (Figure 2.18a).

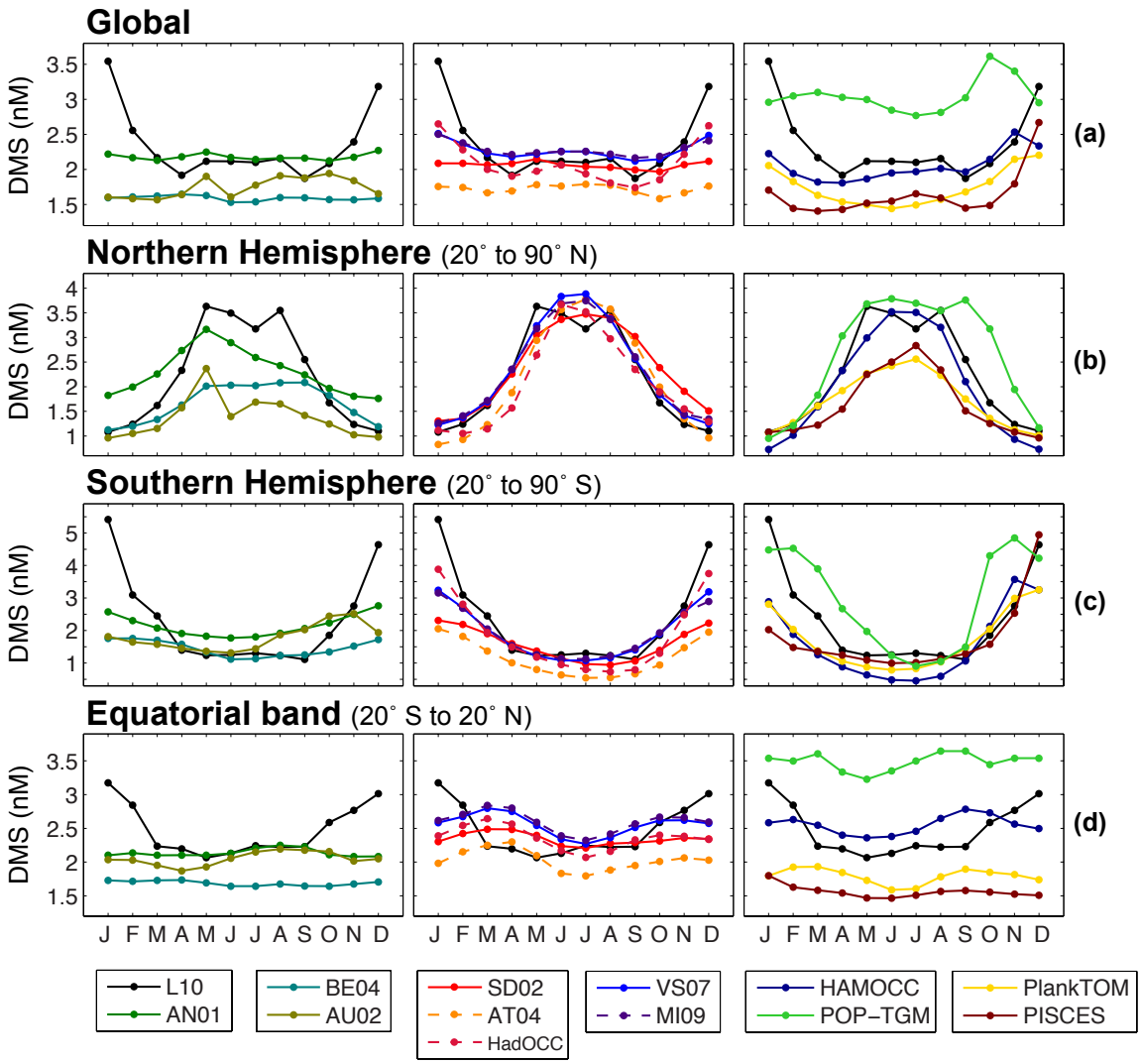

Figure 2.18: Annual cycles of monthly mean surface ocean DMS concentrations for (a) global mean, (b) the Northern Hemisphere (20°-90°N), (c) the Southern Hemisphere (30°-90°S) and (d) equatorial band (20°S-20°N). L10 is shown in black in all panels.

Extratropical seasonal cycles show better agreement between reconstructions and L10 in the Northern versus the Southern Hemisphere (SH), as shown in Figure 2.18b and 2.18c. The annual cycles in Figure 2.18c indicate that the lower agreement in the SH compared to NH seems to be mainly due to the reconstructions not producing the high mean concentration in the SH summer. Seasonal cycles in the lower latitudes are largely uncorrelated with each other, and none of the reconstructed seasonal cycles look like the seasonal cycle of L10. However, the seasonal amplitude is generally low (Figure 2.18d).

Averaging by 30° latitudinal bands permits comparison among the different approaches, highlighting approaches that agree better in particular latitude bands. Seasonal cycles are much larger in the mid and high latitudes where the different approaches also show a more constrained picture of the extent of seasonality. In particular, the waters close to Antarctica are where approaches mostly diverge in terms of seasonal variability. Models show seasonal cycles more comparable in amplitude to L10; PISCES and HAMOCC have the largest range (Figure 2.12). The latitude band from 30° to 60°S, which can be mostly associated with the Southern Ocean, shows less of a spread in variability among the schemes. Modeled DMS again has higher seasonal variability, which is similar to L10. The best agreement with L10 is provided by HadOCC, which modulates DMS via modeled MLD and shows a seasonal range closest to L10. DMS cycles that are parameterized via MLD also show good agreement in seasonal pattern but with significantly reduced variation. HAMOCC, and to a lesser extent PlankTOM, match L10 in terms of variation, but have generally lower mean DMS concentration (by ∼1 nM). Interestingly, the cycle given by PISCES is much reduced in this latitude band compared to cycles close to Antarctica and show a seasonal range that is comparable to the parameterizations.

Seasonality is much lower among all approaches near the equator, and seasonal cycles in the lower latitude bands show the weakest agreement (Figure 2.12 and 2.18d). L10, parameterizations and models differ on where the maxima and minima occur during the year. While L10 shows high concentrations in the NH winter and low concentrations in the summer, models like PlankTOM and HAMOCC show slight maxima in February/March and a greater peak in September. MLD derived DMS fields, including the one from HadOCC, show a large peak in the NH spring, a small peak in October and lows in the NH summer. Although these differences are clearly apparent, the very low seasonality in the equator needs to be considered, and most approaches match the mean values in the equatorial zone.

Annual cycles agree in the NH mid-latitudes, where the concentration peaks in NH mid-summer and shows a sharp decrease in fall to the NH winter low (Figure 2.12). The L10 cycle shows high values throughout the summer with two distinct peaks in May and August. The MLD derived fields, especially AT04, match this cycle well, with a single peak in July and a slightly sharper rise and fall at the beginning and end of the summer season. HAMOCC matches L10 with a single peak in May and an earlier decline in June/July. In this latitude band, there is no difference in seasonal range between parameterized and prognostic DMS. Indeed, PlankTOM and PISCES show low seasonal ranges in this latitude band; about half of that of L10 and most other approaches. The Arctic (60° to 90°N) is again a region where cycles diverge (Figure 2.12). Here, AN01, VS07, and MI09 provide the best match with L10. Prognostic models yielded much larger seasonal amplitude compared to the other approaches. Summer peaks, i.e., June/July, are around 6-8 nM, while L10 peaks earlier, in May, at around 4.5 nM. However, this latitude band is probably one in which little confidence can be placed in either models or the climatology.

Spatial patterns of temporal correlation with L10 The regions where algorithms and global models are consistent, or inconsistent, with the seasonal cycle of the observations in L10 can be identified by analysis of the spatial variations of the temporal correlation with L10 (Figure 2.19). Global distributions of Spearman's rank correlation coefficient (ρ) between L10 and the corresponding reconstructed DMS (Figure 2.19) further demonstrate that most reconstructed DMS variations match L10 in the northern and southern high latitudes. The northeastern Atlantic is a region where almost all approaches can reproduce L10 seasonality. Furthermore, this region has high observational data coverage, so it is where one can put more confidence in L10. The seasonality of DMS over most of the Southern Ocean is consistent between L10 and most reconstructions, with the exception of BE04. In much of the Southern Ocean, BE04 has a high degree of anticorrelation, which means that it has a similarly phased seasonal cycle, with opposite phase. PlankTOM and PISCES show slightly less correlation around the Southern Ocean region compared to HAMOCC, AN01 and all MLD-based approaches.

The strong correlation of SRD and L10 DMS has been shown by Vallina et al. (2007a) and Lana et al. (2012). However, although the phases of the DMS seasonal cycles from VS07 and MI09 match that of L10, they generally cannot match the seasonal amplitude (see for example Figure 2.18c). Furthermore, MLD- and SRD-

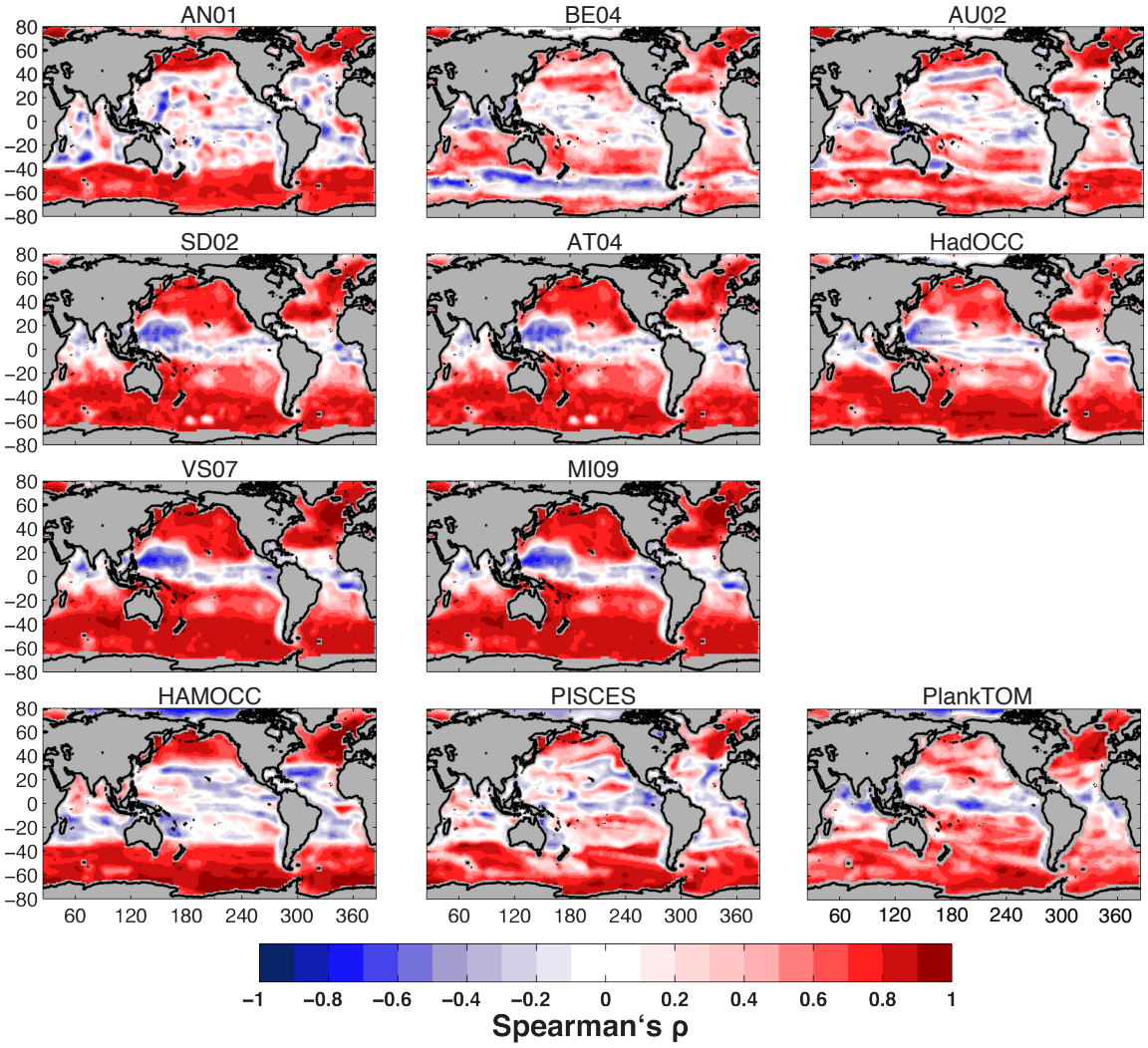

Figure 2.19: Global distribution of correlation (Spearmans rank correlation coefficient) between seasonal cycles of reconstructed or modelled DMS and climatological DMS from L10.

controlled fields clearly match with L10 seasonality in the Sargasso Sea. The process model HAMOCC, by contrast, clearly does not match with L10 seasonality in the Sargasso Sea. Other process models, such as PISCES and PlankTOM, show positive correlation with L10 in the Sargasso Sea, of varying strength (Figure 2.19).

Within the equatorial band, none of the approaches seem to represent a DMS seasonal cycle that matches L10. This finding agrees with the general divergence in modelled DMS distribution at low latitudes (Le Clainche et al., 2010). However, seasonal variability in the tropics is generally low (Figure 2.18d), so slight variations in the annual cycle can lead to weak or even negative correlations (Lana et al., 2012).

2.3.4.2 Testing gridded fields of DMS against observations

The extrapolated fields of L10 suffer from inhomogeneities in both geographic and temporal distribution of the data from which they are calculated. In order to circumvent L10 in the assessment of the algorithms and global model based DMS fields, reconstructions were also tested and compared against the database of available DMS observations. In testing the gridded DMS fields against observations, two spatial resolutions were considered. For the coarser resolution, available bottle data as given by the GSS database were binned into 5°×5° grid boxes. For the finer resolution, the un-extrapolated 1°×1° climatology as described in Lana et al. (2011) was used.

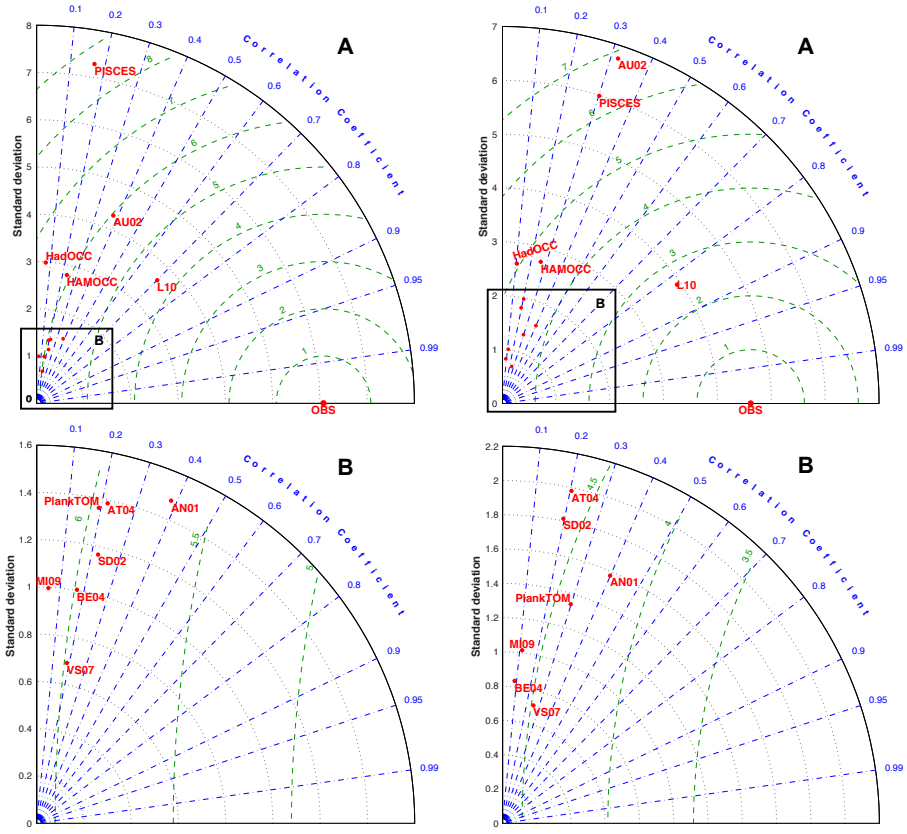

Figure 2.20: Taylor diagrams for surface ocean DMS concentration showing the summary statistics of the 12 reconstruction approaches and L10 compared to 1°×1° (left) and 5°×5° (right) monthly averages, of the GSS observational dataset. Climatologies are separated by variance due to very different ranges in different data sets. Panels A are Taylor diagrams containing DMS climatologies having similar or greater variability compared to the observations (OBS). Panels B are Taylor diagrams with all climatologies having significantly smaller variability compared to OBS.

Figure 2.20 (left) shows Taylor diagrams of reconstructed space-time distributions of DMS (12 times 1°×1° global fields for each reconstruction) with the un-extrapolated, gridded observational data as provided by Lana et al. (2011). The figure illustrates the spread in variability among the various schemes. The spread is so large that a second Taylor diagram is used to include DMS fields with much lower spatial variability than the observations (Figure 2.20 (left) Panel B). All DMS fields derived from parameterizations with observational input fields have less than half of the variability of the DMS observations (Figure 2.20 (left)). The Taylor diagrams demonstrate the relatively weak correlations between observations and climatologies. Even the L10 distribution, which is constructed from the same dataset as it is tested against, shows a correlation of only 0.70. Given the relatively great weight the AN01 algorithm places on chlorophyll as a predictor, correlation of AN01-derived DMS with observation is better than expected (r = 0.39), whereas algorithms that base their DMS distribution mostly on MLD do less well (r = 0.21) in this comparison. Biases are not distinctly smaller for more complex prognostic approaches. The prognostic formulation of PISCES yields variability comparable to observations. To a lesser extend, this is also true of HAMOCC and HadOCC.

Figure 2.20 (right) shows the same set of Taylor diagrams in which DMS grids, including the L10 climatology, are subsampled at 5°×5° resolution and tested against observational data binned with this resolution. The coarsening of the grid has been done to minimize the influence of mismatches of smaller scale features between the different datasets on the statistics. In fact, the results are very similar compared to Figure 2.20 (left). Correlations for some datasets are slightly stronger, but most remain essentially unchanged compared to the 1°×1° resolution. Most datasets showed a reduction in variance when 5°×5° were used instead of 1°×1°. Variability was reduced most for the observational reference dataset: the standard deviation decreased from 6 nM to 4.6 nM. These fairly minor shifts in statistics between 1°×1° and 5°×5° resolution demonstrates that the generally weak correlations are due not only to small-scale differences, but to a mismatch on larger scales.

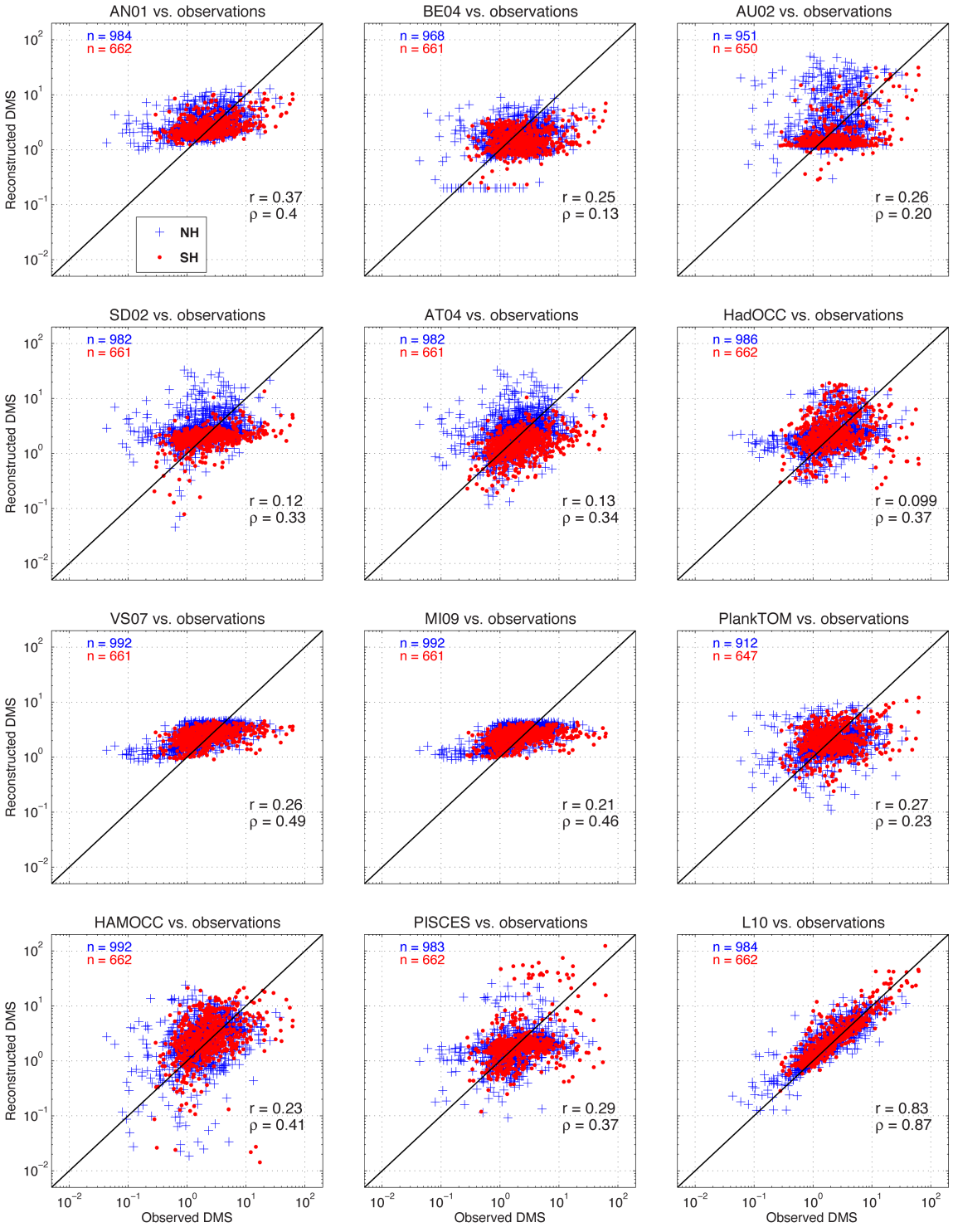

Figure 2.21: Scatter plots (log scale) of parameterized/modelled versus raw observed DMS concentration (nM). In-situ DMS concentration samples were averaged in monthly 5°×5° bins and compared to the corresponding 5°×5° monthly averaged value of each modelled/parameterized DMS field.

The relationships of the 5°×5° grids of parameterized or modelled DMS against the binned observations are also illustrated by spatial scatter plots (Figure 2.21). The scatter plots further demonstrate that while most algorithm or global model based DMS fields have a positive correlation with observations, none reproduce the observations convincingly. Even with the coarse spatial averaging to 5°×5° grid boxes, most parameterizations are unable to reproduce the range of variability seen in observations. Process-based modelling generally shows greater variability (not necessarily matching the observations). As the Taylor diagrams (Figure 2.16 and 2.20) already indicated, the main differences among parameterized and prognostically derived DMS is the extent of variability.

2.3.4.3 Annual cycles of sea-surface DMS concentrations in particular regions

The results of Section 2.3.4.2 demonstrate that none of the reconstructed or simulated DMS fields agree well with observations on a global scale. However, regional-scale analysis can provide more insight into the relative performance of the different approaches. While Kettle et al. (1999) and Lana et al. (2011) separated the ocean into biogeochemical provinces using the scheme of Longhurst et al. (1995), a different approach to defining the regions is used in the present study. Regions with fairly good observational coverage are chosen to characterize the observed seasonal cycles and then compared to the seasonal cycles of the different empirical and prognostic models in such regions. Investigating these seasonal cycles can help characterize model biases for specific regions, which in turn give insights into why a given model has certain biases. Because of the relatively small area of the chosen regions (about 20°-by-20°), a more meaningful variability, less affected by regional differences, can be obtained. Furthermore, the regional analysis allows evaluation of how the inherent variability of raw observations affects the fit with monthly means from models and climatology.

Two regions are considered in the North Pacific (Figure 2.22a and 2.22b): one around Ocean Station P in the Northeast Pacific (Figure 2.22a), extending from 40° to 55°N and 135° to 150°W, and the second in the Bering Sea (Figure 2.22b), extending from 55° to 65°N and 165° to 180°W. The Bering Sea is distinguished from the Aleutian Gyre region because it has broad continental shelves and a different seasonal cycle of productivity from the open North Pacific (Banse and English, 1999). The analysis is limited to the eastern half of the Bering Sea because of limited data coverage in the

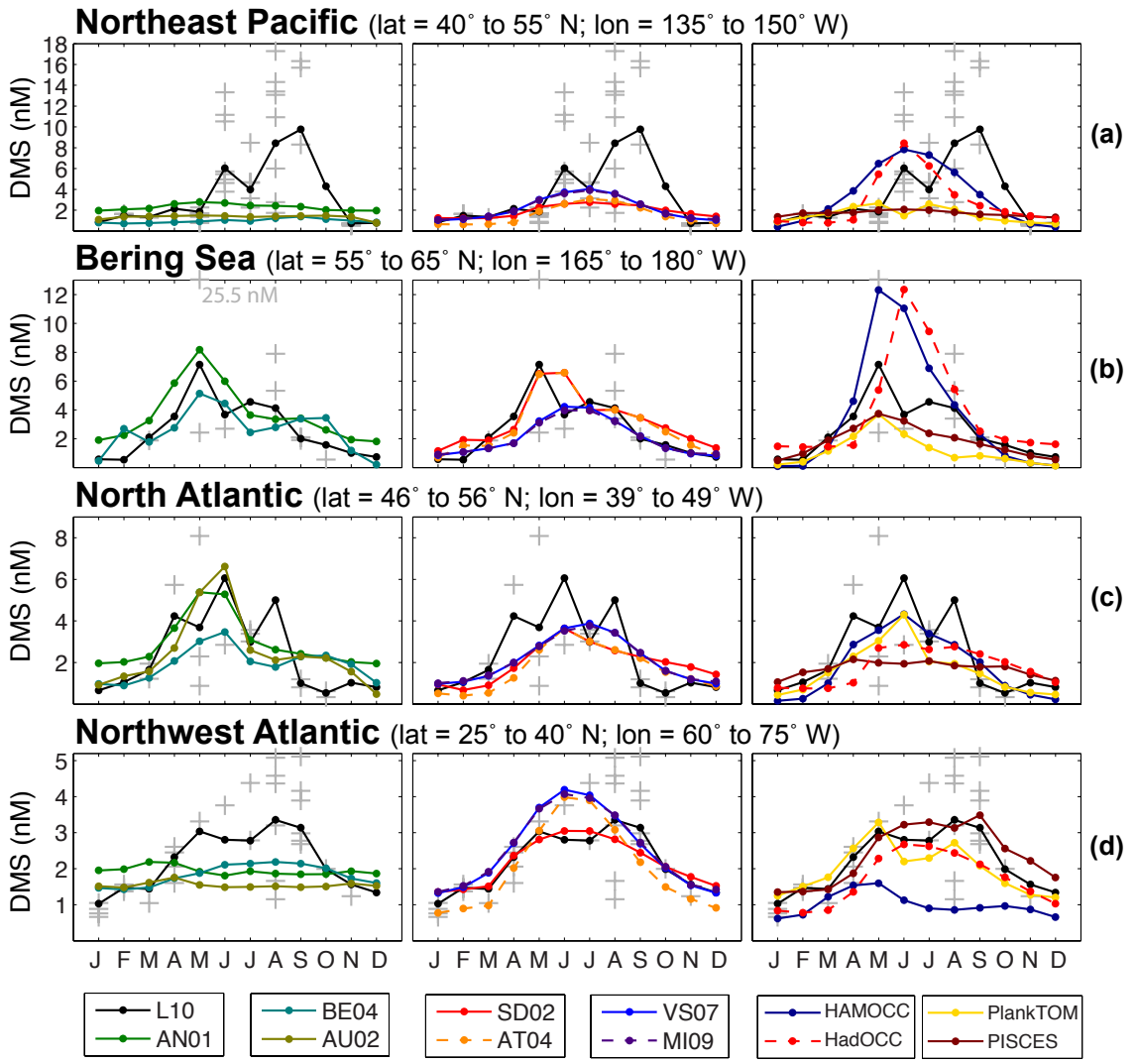

Figure 2.22: Annual cycles of monthly mean surface ocean DMS concentration in different regions. Grey crosses (+) are 5°×5° averages of in situ DMS observations extracted from the GSS database. (a) Northeastern Pacific near Ocean Station P (50°N, 145°W), (b) eastern Bering Sea, (c) North Atlantic (south of Greenland), (d) Northwest Atlantic (around BATS station), (e) Northeast Atlantic (east of the Azores), (f) Equatorial Pacific and (g) southern Indian Ocean.

western half and difference in productivity between the eastern and western regions (Springer et al., 1996).

The two selected regions in the North Pacific (Figures 2.22a and b) are relatively similar in the overall shape, except that in most cases the annual cycle of DMS concentration in the Bering Sea (Figure 2.22b) have an earlier summer maximum than those in the Northeastern Pacific (Figure 2.22a). Most reconstructions and

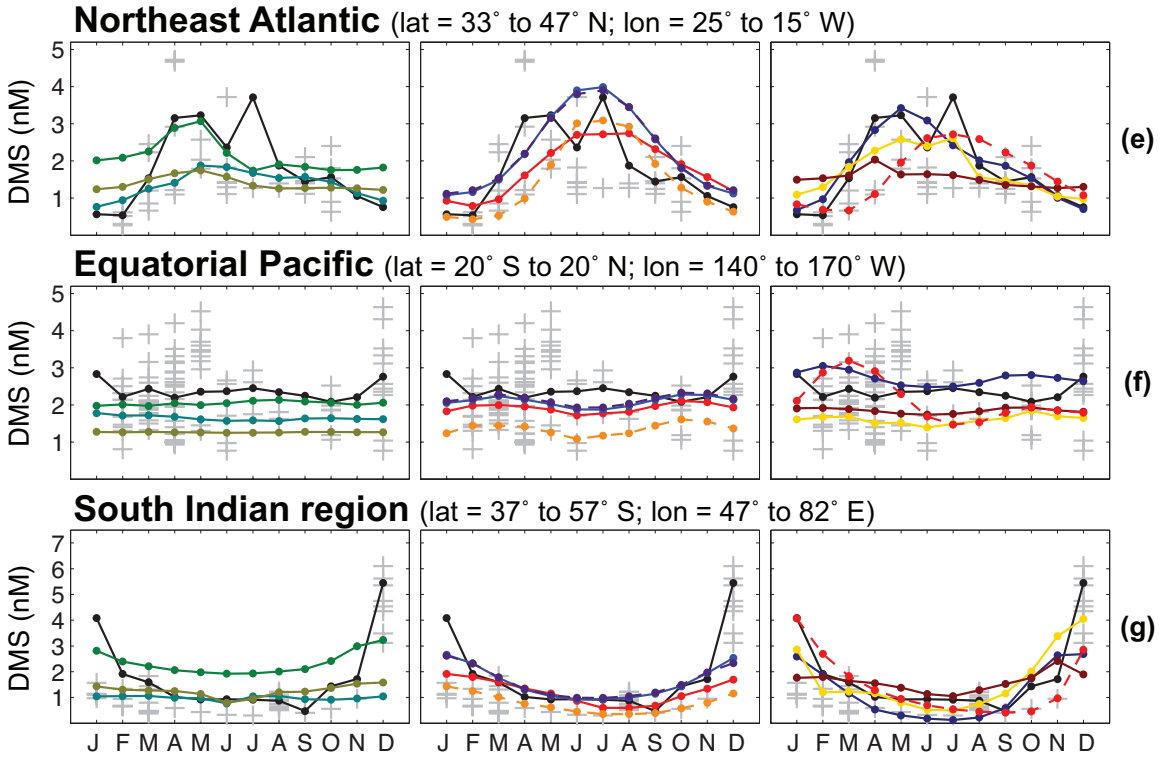

Figure 2.22 (continued).

models are unable to capture the seasonal cycle in the Northeast Pacific region. Only HadOCC and HAMOCC show high DMS concentrations in the summer as indicated by the observations (Figure 2.22a). Agreement between predicted and observed DMS seasonality is better in the Bering Sea. In both regions, the observations and L10 show the same general seasonal cycle, but with the observations having much more scatter. This is true for most of the regions examined in this study.

For the North Atlantic, three different regions are selected. The first one is an area south of Greenland with a similar range of latitudes as the Northeast Pacific: 46° to 56°N and 39° to 49°W (Figure 2.22c). The second is in the Subtropical North Atlantic around the Bermuda Atlantic Time-series Study (BATS) location and extends from 25° to 40°N and 60° to 75°W (Figure 2.22d). The third is the Northeast Atlantic east of the Azores and extends from 33° to 47°N to 15° to 25°W (Figure 2.22e).

The difference in DMS seasonality between the North Pacific (Figures 2.22a and b) and North Atlantic (Figure 2.22c) is similar in many reconstructions, especially HadOCC and HAMOCC, for which summer variations in chlorophyll and DMS are tightly coupled. These models do not produce the observed high concentrations

in either the North Atlantic (Figure 2.22c) or the North Pacific during summer (Figures 2.22a and b). In the Bering Sea, the MLD-/chlorophyll-based approaches perform slightly better than the SRD/UVRD-based approaches. The seasonal cycles of HadOCC-simulated DMS in the North Atlantic and North Pacific are similar, but the amplitudes are considerably reduced in the North Atlantic compared to the North Pacific. In the North Atlantic, strong phytoplankton blooms are generally observed during spring, and a deep mixed layer is present during winter. The intensity of North Atlantic spring blooms differs from that of North Pacific spring blooms, partly because of iron limitation and the permanent halocline, which does not allow deep mixing (Gargett, 1991). Therefore, not much entrainment of nutrients occurs during winter. This phenomenon seems to be reflected in SD02/AT04 (as well as in AN01), but not in HadOCC, where the reduced amplitude observed in summer DMS in the North Atlantic compared with the North Pacific seems counterintuitive.

The seasonal amplitude of observed DMS concentration in the Northwest Atlantic is best matched by SRD/UVRD-based models (VS07 and MI09), for which the DMS estimates exhibit even stronger seasonal variation than L10. This variation closely agrees with the raw observation averages in the summer months (Figure 2.22d). However, it is clearly different from the seasonality of chlorophyll (not shown), as can be deduced from the poor performance of approaches such as AN01 and HAMOCC. Chlorophyll is not necessarily a good proxy for productivity in the subtropics (Winn et al., 1995). The seasonality of DMS concentration in this region suggests a fundamental difference between the underlying mechanisms that control general biological productivity and DMS production. The good fit of SRD/UVRD-derived DMS with observations from the Northwest Atlantic suggests that an external environmental factor related to solar irradiance might be an appropriate proxy for DMS in that particular region.

The observed seasonal cycles suggest that the Northeast Atlantic region (Figure 2.22e) is a distinctly different regime compared with the Northwest Atlantic region. DMS concentration is observed to peak during spring or early summer and thus conforms more to a classic spring bloom pattern. Chlorophyll-based approaches such as AN01 and HAMOCC therefore perform well in matching with the raw observations and climatological seasonal cycle, while MLD- or SRD/UVRD-based methods (SD02, AT04, HadOCC, VS07 and MI09) incorrectly estimate the peak of DMS concentration later during summer.

The tropical Pacific is an interesting region because of the major differences in

the seasonal cycle among models and parameterizations, as well as in comparisons to climatology (L10) and observations. For the tropical Pacific, a region between 20° north and south and 140° to 170°W is chosen. In this region, observations indicate considerable variability compared with the overall amplitude of estimated seasonal cycles (Figure 2.22f). The seasonal cycle of DMS is not well captured in tropical latitudes. Most approaches agree on the generally low seasonality of DMS. MLD-dependent approaches, particularly HadOCC, show greater seasonality. However, the seasonal cycle is uncorrelated with that given by the climatology (Figure 2.22f).

The South Indian Ocean again shows a high degree in seasonality with DMS peaking in December (Figure 2.22g). While all of the global model and algorithm products show basically the same seasonal cycle, the amplitude is considerably underestimated by the algorithms. Consistent with observations, the algorithms and models show low DMS concentration in the Southern winter, although concentrations are too low during Southern summer. None of the methods obtain a seasonal cycle as large as the one suggested by the climatology. Only some of the global models, such as HadOCC, HAMOCC, and PlankTOM, get close to the observed and climatological seasonality.

2.4 Discussion

2.4.1 Application of empirical models as an alternative to fully prognostic schemes

Both prognostic and diagnostic approaches are currently being used to model sea-surface concentrations of DMS. Whereas diagnostic models use empirical relationships between environmental variables and DMS, prognostic modelling accounts for the processes controlling the sinks, sources and cycling of DMS and its precursor compound, DMSP. Despite their much greater complexity in comparison to relatively simple empirical models, prognostic models do not do much better in reproducing observations (Figures 2.16, 2.20, 2.21). Figure 2.21 suggests that prognostic approaches yield DMS distributions that on average agree slightly better with observations in terms of variance and correlation. However, the limited success of process-based models suggests that some biological or environmental factors contributing to the DMS budget are missing from prognostic modelling approaches, or that the factors that are incorporated are modelled incorrectly. Previous studies identified a major limitation of current prognostic approaches to be an overly strong coupling of the sulfur cycle and

ecosystem dynamics (Cropp et al., 2004; Le Clainche et al., 2010). As the use of DMS diagnostic formulations within ocean models is more computationally efficient than prognostic formulations, they may still be a good alternative. Their performance is not substantially worse in terms of correlation than the current (and far more complex) prognostic schemes.

This study has demonstrated that a clear shortcoming of empirical models using observed climatologies is that the spatial and seasonal variance of DMS is much lower than indicated by observations. This is not the case for DMS fields simulated by the empirical algorithms implemented within a model (e.g., HadOCC), where DMS is calculated with instantaneous simulated quantities (in the HadOCC case, chlorophyll and MLD). Monthly averaged DMS fields from such coupled diagnostic modelling seem to have variance much closer to the variance of the L10 climatology and of the raw observations. Although having a model bias, the modelled spatial and temporal fields have more similar variation to the observed DMS than similar algorithms using monthly averaged observation-based fields as inputs. Furthermore, there could also be issues with short-term and interannual variability in the input fields that is averaged out when applying the algorithms to derive DMS from climatological input fields. For example, the SD02 formulation, with MLD as an input, only uses the climatological monthly fields, because that is all that is available on a global scale. However, there can be strong anomalies relative to the climatological seasonal cycle. It is possible that the omission of such deviations from the mean state creates a bias. Again, the use of such algorithms in a model would not have this disadvantage, as the algorithms utilize instantaneous values of the input fields. However, the input fields will have model biases, and it is not clear by how much fidelity is affected by the use of climatological observation-based versus using instantaneous simulated input fields.

Algorithms trained on climatological data (e.g. of chlorophyll, MLD, or irradiance) cannot be expected to capture either sub-monthly or interannual variability. This problem is of particular concern when these algorithms are implemented within GCMs. A preferable approach would be to develop algorithms using instantaneous simultaneous observations of DMS and the predictor variables. This approach is not possible using existing datasets, but could guide the future collection of data.

It is also possible that many of the limitations of the parameterizations are due to differences in spatial and temporal coverage between the data used for developing the parameterization and the data against which the algorithms are tested. Regression analyses presented here (e.g., Figure 2.1 and 2.4) indicate that the apparent lack of

skill in the parameterizations is not just due to differences between the distributions of training and tested datasets. Reparameterizing the different algorithms for a more global coverage of data did not significantly improve the correlation when tested on a global scale. However, in tuning an algorithm for a specific region, its performance in reproducing observations might be significantly improved for a particular region, such that the applicability of an algorithm might vary extensively depending on the region.

However, it seems that empirical algorithms for DMS cannot be universally applied. If an empirical algorithm is trained on data collected at certain times and in certain places and then tested against data collected at other times and places, the space/time difference alone will affect the skill of the algorithm. One reason for the lack of skill is the sampling bias. This is an inherent concern with empirical models, as an empirical model is only as good as the data that it is trained on. However, if there is true generality in the formulations in the models, this should not matter. It should be able to be trained in the Atlantic and applied in the Pacific (Friedrichs et al., 2007). If this does not work, then the algorithm is lacking in generality. This seems to be the case in all of the DMS empirical algorithms that were tested in this study.

Given such considerations, it is important to keep in mind the limitations of the empirical DMS algorithms (Halloran et al., 2010). Belviso et al. (2012) raised concern regarding the generality of the parameters influencing the global distribution of DMS. The functional form of an empirical model can not be easily adjusted to a specific region or ocean regime, nor is there great opportunity to resolve phytoplankton taxonomic composition, which is an important factor in DMS production. As an example, the Fp ratio, as a community structure index, represents a simple shortcut to account for the different source strength of DMSP/DMS among phytoplankton types, but it is too simple to account for species specific DMS production. A focus on specific phytoplankton taxa is only possible with the development of explicit models. The use of algorithms in global estimation of DMS may be an option for climate modelling purposes. In terms of studying the underlying mechanisms of the DMS production, research needs to be focused on the further development of mechanistic models.

2.4.2 Representativeness of DMS variations in climatologies versus models: The problem with using climatologies as a reference

When comparing empirical DMS reconstructions or simulations with L10, it is important to consider the essential difference in methodology between these. In the case of L10, the fields are directly derived from *in situ* observations by interpolation and extrapolation of data points that are localized in space and time. Localized high concentrations, which may not be representative of the local space- or time-mean, are extrapolated across data-sparse regions in L10. The main disadvantage of L10 and its precursors (K99 and K00) is thus that small-scale features are transformed into large-scale ones by the interpolation procedure. In contrast, the spatial scales of parameterized and model-derived DMS fields are derived from the input fields or the global model dynamics. Disagreement between L10 and such fields cannot necessarily be interpreted as errors of the reconstructed or simulated fields.

Furthermore, extrapolation of a relatively small number of data points in L10 can lead to unrealistic distributions that do not conform to ocean biophysical features. The construction of a climatology from raw data leads to a significant reduction in spatial variance. Where there are regions with generally low DMS concentration and 'hot spots' of high concentration, L10 shows a generally higher values, and these high concentrations are generally more spread out. The lack of coverage in space and time limits the reliability of the climatologies. For example, the equatorial Pacific upwelling region in L10 is characterised by large 'bulb' of high concentration that do not conform any obvious geophysical mechanisms. In the development of gridded DMS climatologies, it is important to assess if such features are based on something realistic, or if they occur simply because there are certain times of year, or certain years, that samples were taken there.

The Kettle climatologies (K99 and K00) have data up to 1999 and 2000, respectively. Using data collected after 2000 as an independent dataset, Halloran et al. (2010) showed that the mismatch between K99 and the post-2000 observational database is as bad or worse as that of algorithms. The data collected after 2000 most likely have a different space/time distribution than the data collected before 2000. To some extent, this should explain the weak correlation with K99 presented by Halloran et al. (2010). The high correlation between observations and L10 shows that sampling significantly improves climatologies (particularly in data-rich regions). However, using

new observations, independent of L10, to test L10, might lead to a similar mismatch as demonstrated by Halloran et al. (2010) with K99.

Sparse sampling affects the temporal structure of the climatologies as well as the spatial structure. Finding appropriate estimates of monthly mean DMS concentration is difficult given the high temporal variability of DMS in most of the ocean (Asher et al., 2011; Tortell et al., 2011; Tortell, 2005). This might be particular problematic for the assessment of seasonality in high latitudes. In the construction of monthly climatologies, undersampled regions such as the Southern Ocean will be influenced by large individual point measurements that are not representative of the whole month. Furthermore, there are many regions that have large interannual variability (Halloran et al., 2010), which by construction is disregarded in the design of the climatological maps but may have a dynamical relevance. The tropical Pacific might be especially a problematic region when ignoring interannual variability (Figure 2.22f).

2.4.3 Further developments in understanding what controls DMS in the ocean

This study clearly shows that current models (both empirical and prognostic) are not strongly correlated with the DMS observational database. However, the relatively sparse observational data coverage prevents a truly global assessment of the reconstructed and simulated DMS fields. Furthermore, the presence of interannual variability results in differences between reconstructed and simulated DMS fields and the raw observations, as outlined in the above section.

The general disagreement of the different approaches with raw observations underscores the high spatial and temporal variability and the complexity of the underlying ecosystem processes. Given the complexity of marine DMS production/consumption mechanisms, involving various pathways of sinks and sources for DMS, it is understandable that it is difficult to find a universal relationship between DMS seawater concentration and any other parameters such as chlorophyll concentration, MLD, or irradiance. Earlier studies suggested that linking DMS to key parameters is possible on a local to regional scale for a specific time of the year (e.g., Aranami and Tsunogai, 2004; Kameyama et al., 2013; Miles et al., 2012). However, doing so for large spatial and temporal scales has not been successful to this point.

Historically, oceanic concentrations of DMS was mainly related to plankton biomass since phytoplankton and algae are known to generate the precursor compound DMSP.

However, it is now known that many other factors, such as nutrient conditions, the level of incident UV solar radiation, and various other stress factors have an effect on DMSP production. On top of these complexities, the formation of DMS from DMSP is a complex process controlled by different mechanisms. As a result, DMS is only indirectly related to DMSP and, in turn, DMS and DMSP are often weakly (or not at all) correlated with parameters such as chlorophyll or phytoplankton biomass.

A recent study conducted in the Northwest Atlantic region by Lizotte et al. (2012) made a clear distinction between those parameters correlated with DMS production and those parameters affecting DMSP release. While DMSP production is more associated with biological parameters such as chlorophyll, community structure, and bacterial biomass, DMS is clearly less correlated to such parameters and more linked to physical factors such as MLD and solar irradiance. The development of DMS ecosystem models based on experimental and field work should provide better representation of the mechanisms responsible for DMS concentrations in the ocean. In this regard, recent studies have emphasized the decoupling of DMS production from the productivity of the underlying ecosystem (Cropp et al., 2004; Le Clainche et al., 2010).

Given the complexity of the marine DMS(P) cycle, it is useful to distinguish different regimes based on differences in physical and ecological factors. Toole and Siegel (2004) argued for the existence of two different types of regimes with distinct factors controlling DMSP production and DMSP to DMS conversion: the "bloom-dominated" and "stress-dominated" regimes. DMS production is more directly linked to phytoplankton productivity in a bloom-dominated regime, while stress factors such as UV radiation and nutrient limitation are the key variables determining DMS production in a stress-dominated case. The notion of stress-induced production of DMS is the main explanation for observations of elevated DMS concentration, uncoupled from algal biomass (called the DMS summer paradox). For example, Vallina et al. (2008) presumed a mechanism for an independent source of DMS directly from phytoplankton cells during the summer due to enhanced solar radiation stress. Understanding this mechanism requires further experimental and *in situ* observational studies.

A recent review by Liss et al. (2014) categorized DMS cycling in the ocean by species composition, i.e., dominated either by a high DMSP producer (e.g., coccolithophores) or low DMSP producer (e.g., diatoms). Furthermore, these systems can then be classified into high stress or low stress conditions. For each of these four categories, specific mechanisms can be identified that control the extent of DMSP production and

DMS yield. Such classifications represent a possible avenue of investigation to improve empirical models as well as mechanistic modelling of DMS in ocean ecosystem models.

Chapter 3

Sensitivity of DMS flux

3.1 Introduction

In this chapter the DMS concentration fields that were compared in Chapter 2 are used to estimate the global flux of DMS to the atmosphere. Furthermore, as with the intercomparison of DMS concentration fields, a similar analysis is made for flux fields. Rather than seawater concentrations of DMS, it is the air-sea flux of DMS that ultimately controls how much DMS enters the atmosphere where it potentially influences aerosols, CCN and climate. In order to derive the flux of DMS, we need to know not just the surface concentration of DMS, but also the transfer velocity. In general, the air-sea flux of a gas is derived by multiplying its difference in concentration between air and water phases with the gas transfer velocity (also known as piston velocity). In the case of DMS, the concentration difference is largely defined by the ocean surface concentration because the atmospheric concentration is known to be orders of magnitude smaller. The gas transfer velocity (k_T) is estimated from a simple two-layer gas exchange model (Liss and Slater, 1974). For gases like DMS, it is often argued that water transfer velocity is the controlling factor, so that k_T is just equal to the water-side transfer velocity (k_w), while the air-side transfer velocity (k_a) can be neglected.

The magnitude of k_w is influenced by a number of factors, but is believed to be controlled mainly by physical quantities such as wind speed (through its influence on mixed-layer turbulence and surface wave breaking) and sea surface temperature (SST). There is, however, no unique method to derive the transfer velocity, and there remains considerable uncertainty as to its value or how it should be parameterized.

Parameterizing k_w is difficult, partly because there are so many potentially influential factors to consider. Transfer parameterizations in ocean models generally rely on wind speed and water temperature alone to estimate k_w. In this analysis, it was decided to focus on three of the most commonly used relationships in the DMS flux literature, each of which use reference height (10 m) wind speed (u_{10}) and SST.

Past sensitivity studies have generated estimates of DMS flux by using different transfer velocity formulations, DMS climatologies, and wind/SST fields. Kettle and Andreae (2000) used the K00 data-based DMS climatology to come up with a range of fluxes resulting from different piston velocity formulations and wind fields. This study was global in scale, but used only their climatology. Archer et al. (2002) used a local DMS model to derive a range of flux estimates with different formulations of piston velocity. This study used a process-based approach to derive DMS concentration and flux, but was local in scale (in the northern North Sea). Elliott (2009) used both the K00 DMS climatology and the POP-TGM prognostic model (within CCSM) to derive global DMS flux estimates using piston velocity schemes from Nightingale et al. (2000), Liss and Merlivat (1986), and Wanninkhof (1992) as well as a hybrid of the latter two. The Elliott (2009) sensitivity study was wider in scale than Kettle and Andreae (2000) because it not only used the climatology but also simulated DMS, thereby allowing for a comparison to be made between fluxes calculated using both climatological and instantaneous DMS concentration values. However, the author only considered POP-TGM and K00 as possible representations of the DMS sea surface distribution.

Here, the sensitivity of DMS flux is tested with a range of DMS concentration fields and transfer parameterizations. The differences in DMS concentration among raw observations, data-based climatologies, empirical reconstructions, and simulations is an important indication of the uncertainties of DMS concentration fields. This chapter addresses the influence of the differences among DMS concentration fields on air-sea fluxes of DMS.

3.2 Methods

3.2.1 Air-sea gas exchange parameterizations

The ocean-atmosphere flux of DMS is computed as the product of the gas transfer velocity (k_T) and concentration difference (ΔC) (Liss and Slater, 1974):

$$F_{DMS} = k_T \Delta C \tag{6}$$

where ΔC is the difference between ocean and atmosphere concentrations of DMS. $\Delta C = C_w - C_a/H$, where C_w and C_a are the gas concentrations in water and air, respectively, and H is the dimensionless Henry's law constant. The atmospheric DMS concentrations are usually several orders of magnitude lower than the DMS concentrations in the surface ocean, and can be taken to be negligible, such that $\Delta C = C_w$. The total gas transfer velocity, k_T, can be expressed in terms of resistances on both sides of the air-sea interface. As such we have:

$$\frac{1}{k_T} = \frac{1}{(\epsilon k_w)} + \frac{1}{(H k_a)} \tag{7}$$

where k_w and k_a are the individual transfer velocities for water and air, respectively; ϵ is a dimensionless factor that accounts for any enhancement of the water-side transfer due to chemical reactions (Liss and Merlivat, 1986).

The air-side resistance is often assumed to be small enough to be negligible. This assumption, however, may not hold true at low temperatures and high wind speeds, as demonstrated by McGillis et al. (2000). This study considers both cases: where air resistance is ignored and where it is accounted for. When air resistance is ignored, k_T is just equal to k_w. When air resistance is accounted for, k_T is calculated using the atmospheric gradient fraction (γ_a), such that $k_T = k_w(1 - \gamma_a)$, where $\gamma_a = 1/(1 + k_a/(\alpha k_w))$ (Lana et al., 2011; McGillis et al., 2000). The dimensionless quantity γ_a is the fractional contribution of the gas concentration gradient across the air side boundary layer to the total air-water concentration gradient. The airside transfer coefficient (k_a) is based on the study by Kondo (1975) and calculated as:

$$k_a = 659 u_{10} \left(\frac{M_{DMS}}{M_{H_2O}} \right)^{-1/2} \tag{8}$$

where M_{DMS} and M_{H_2O} are the molecular weights of DMS and water, respectively.

u_{10} is given in $\mathrm{m\,s^{-1}}$, while k_w is expressed in $\mathrm{cm\,h^{-1}}$. The DMS solubility (α) is taken from Dacey et al. (1984) as a function of SST:

$$\alpha = e^{3525/SST - 9.464} \tag{9}$$

where SST is given in Kelvin (K).

Three different formulations of the waterside transfer velocity (k_w) are considered: those of Liss and Merlivat (1986), Wanninkhof (1992), and Nightingale et al. (2000). Hereafter the three formulations are referred to as LM86, W92 and N00, respectively. Liss and Merlivat (1986) developed a piston velocity parameterization originally for CO_2. Equations are developed for three wind regimes based on u_{10}: below or equal to 3.6 $\mathrm{m\,s^{-1}}$ (smooth), between 3.6 and 13 $\mathrm{m\,s^{-1}}$ (rough surface), and higher than 13 $\mathrm{m\,s^{-1}}$ (breaking wave). The latter was found to involve bubble development, which enhanced transfer rates (Table 3.1). This study, however, was based mainly on data from lake experiments (Wanninkhof et al., 1985), which might not be representative for conditions in the ocean. Wanninkhof (1992) developed a quadratic function for wind speed and gas transfer for global winds (Table 3.1). The study by Wanninkhof also demonstrated that different formulations need to be used whether instantaneous (short-term) or time averaged long-term (e.g., monthly mean) wind speeds are used. In the current study, the relationship based on the W92 formulation for short-term winds is utilized since reanalysis fields with instantaneous winds are used.

The piston velocities given by the formulation of Liss and Merlivat (1986) are everywhere lower than those of Wanninkhof (1992), as illustrated in Figure 3.1. Nightingale et al. (2000) proposed a parameterization intermediate between these two, obtained using aspects of both LM86 and W92. The Nightingale et al. (2000) study described four expeditions using volatile and non-volatile tracers in the North Sea to measure sea-air gas transfer rates. The data from all four of these expeditions were combined and used to test the available published relationships for the transfer velocity. While these data showed a dependence of piston velocity on wind speed, the considerable scatter around this relationship indicated that gas transfer was influenced by additional factors. As the data scatter fell between the LM86 and W92 estimates, N00 (Table 3.1) is intermediate between LM86 and W92. Subsequent studies have identified N00 as the best available choice for DMS (e.g., Boucher et al., 2003; Marandino et al., 2009).

Table 3.1: Piston velocity formulations applied in the present work.*

Scheme	k_w as a function of u_{10} and Sc	Reference Sc	Data	Reference
LM86	$0.17 \cdot u_{10} \left(\frac{600}{Sc}\right)^{2/3}$ for $u_{10} \leq 3.6$ $(2.85 \cdot u_{10} - 9.65) \cdot \left(\frac{600}{Sc}\right)^{1/2}$ for $3.6 < u_{10} \leq 13$ $(5.90 \cdot u_{10} - 49.3) \cdot \left(\frac{600}{Sc}\right)^{1/2}$ for $u_{10} > 13$	CO_2 in freshwater at 20°C	Theory, lake data and tunnel experiment	Liss and Merlivat (1986)
W92	$0.31 \cdot u_{10}^2 \left(\frac{660}{Sc}\right)^{1/2}$	CO_2 in seawater at 20°C	Large-scale bomb and radiocarbon	Wanninkhof (1992)
N00	$(0.333 \cdot u_{10} + 0.222 \cdot u_{10}^2) \cdot \left(\frac{600}{Sc}\right)^{1/2}$	CO_2 in freshwater at 20°C	He, SF_6 and an inert, involatile dilution tracer	Nightingale et al. (2000)

* Definitions: Scheme abbreviations are as indicated in the text. u_{10} is wind speed referenced to the 10 m level and expressed in $\mathrm{m\,s^{-1}}$. The piston velocity (k_w) is expressed in $\mathrm{cm\,h^{-1}}$. The Schmidt number (Sc) is a function of SST as given in Saltzman et al. (1993) and is dimensionless.

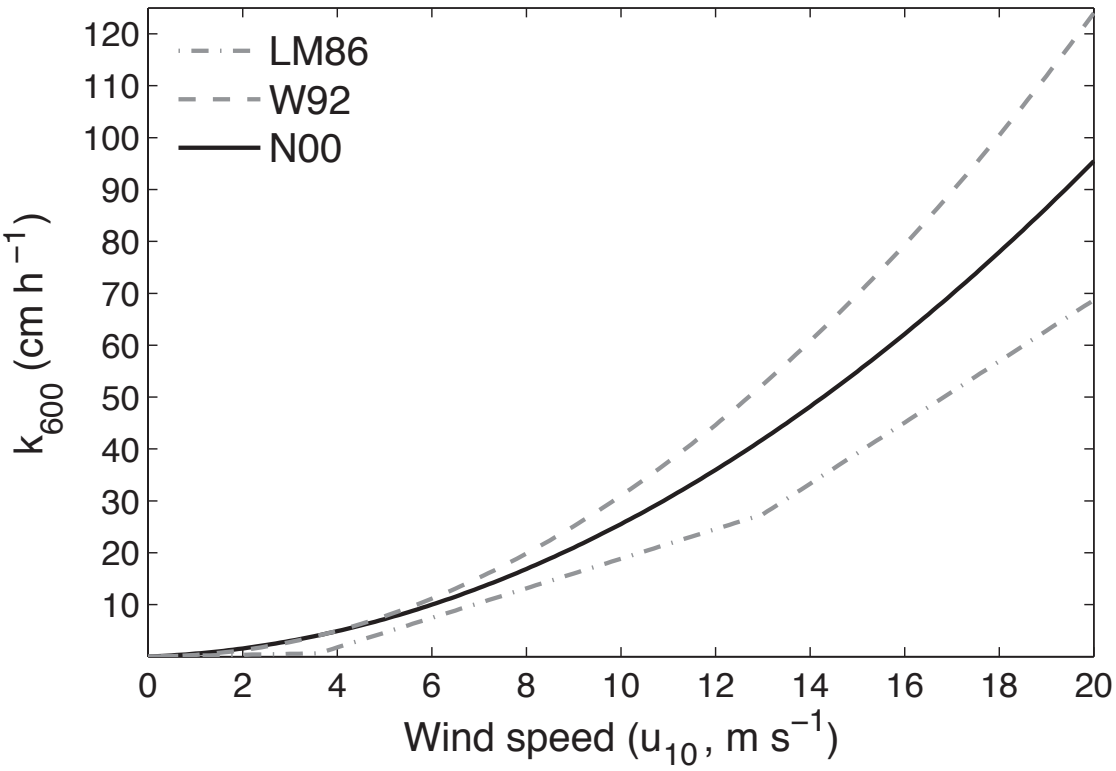

Figure 3.1: Gas transfer velocity (k_{600}) as a function of wind speed for the three gas transfer wind speed relationships used in this study: LM86 (Liss and Merlivat, 1986), W92 (Wanninkhof, 1992) and N00 (Nightingale et al., 2000). k_{600} indicates that the gas transfer velocity is normalized to a Schmidt number (Sc) of 600 which corresponds to Sc of CO_2 in freshwater at 20℃.

Figure 3.1 is a graphical representation of the k_{600} piston velocity (i.e., k_w normalized to a Schmidt number of 600) versus wind speed relationship for the three formulations. The piston velocities are Schmidt number corrected, after the equations of Saltzman et al. (1993), to account for molecular diffusivity. Under LM86, the Schmidt number dependence varies according to wind speed from negative two thirds power (smooth surfaces) to negative one half (rough surface and breaking wave). For W92 and N00, the Schmidt number dependence is negative one half power, which is likely inaccurate for very low wind speeds (Elliott, 2009). Unlike LM86 and N00, the Schmidt number reference value for W92 is chosen for CO_2 in seawater (Sc=660) rather than freshwater (Sc=600).

3.2.2 Data

The transfer velocity k_T was calculated using wind speed, sea surface temperature (SST), and sea-ice cover from ERA-Interim, the global atmospheric reanalysis produced by the European Centre for Medium-Range Weather Forecasts (ECMWF). These data were obtained from the ECMWF website (http://apps.ecmwf.int/datasets/data/interim_full_daily/) and are described in Dee et al. (2011). Kettle and Andreae (2000) considered the sensitivity of estimated fluxes to different global-scale wind and SST climatologies. As sea surface wind fields from modern reanalyses are robust and agree well with observations (Monahan, 2006), this study will use only ERA-Interim reanalysis products.

Climatological air-sea fluxes of DMS were derived by using the 12 monthly fields of a given DMS climatology and a given 12-month climatology of k_T. To derive the k_T climatologies, daily instantaneous (0:00 GMT) wind speed, SST and sea ice cover for the period of 1979 to 2011 were used to derive global fields of daily instantaneous k_T. Different k_T climatologies were derived depending on the wind parameterization scheme (LM86, W92 or N00) and whether air resistance was considered or not. The reduction in flux due to sea ice was incorporated into the calculation of k_T, such that the final transfer coefficient was taken as k_T (1-f_{ice}), where f_{ice} is the ice-covered fraction. The daily fields of the final transfer coefficient were then averaged by month to create a 12-month climatology. In order to derive DMS flux fields from the concentration fields, the transfer coefficient climatology was converted from the ERA grid (1.5°×1.5°) to that of the DMS concentration climatology (1°×1°) by linear interpolation.

The DMS datasets that were used to derive the flux field do not have complete global and seasonal coverage. When comparing integrated flux, it is necessary that data coverage between different DMS climatologies is comparable so that comparisons can be made without biasing flux estimates from regions with limited temporal and/or spatial coverage. The de Boyer Montégut MLD climatology (de Boyer Montégut et al., 2004) is used for all of the MLD-derived DMS algorithms (SD02, AT04, VS07 and MI09), in which there are data missing in the northern high latitudes during the boreal winter (December, January and February). These data are likely missing due to sea ice cover during that time. However, other fields such as L10 or model fields of DMS have data in those regions. To compare all of the fields together, missing values in the high latitude Northern Hemisphere winter were replaced with a near-zero concentration (0.001 nM) (assuming very low concentration during winter). For the

few cases where there were missing data values during summer (which would likely have higher concentrations of DMS), DMS was calculated from the CanESM2 MLD field.

In addition to climatological flux fields, the ERA-Interim data were also used to derive fluxes corresponding to each individual DMS measurement in the GSS database (see Section 2.2.1.1). ERA-Interim datasets for wind velocity, SST and ice cover were subsampled at the location, date and time of the corresponding GSS concentration, and used to derive an instantaneous value of the gas transfer coefficient, which could then be used to derive an estimate of flux. In order to compare these observational estimates with climatological flux, the resulting GSS fluxes were averaged for each month over the period 1979 to 2010 to yield a $1^{\circ}\times1^{\circ}$, 12-month climatology of observed flux.

3.3 Results

3.3.1 Ranges of global annual total flux given available DMS fields and wind parameterizations

Table 3.2 lists the range of possible global integrated DMS flux for each concentration field and piston velocity parameterization, ranked in order of increasing transfer coefficient (LM86, N00 and W92). All flux estimates in Table 3.2 were derived without accounting for air-side resistance. Use of LM86 produces the lowest fluxes, while W92 produces the highest fluxes. In the case of empirical algorithms, there is additional uncertainty associated with the different input fields. The ranges in Table 3.2 clearly demonstrate a substantial divergence among global DMS flux estimates obtained using piston velocity parameterizations and concentration fields commonly found in the literature. Given the uncertainty of both piston velocity parameterizations and DMS reconstructions, the range of potential fluxes is quite large (8 to 33 TgS y^{-1}; Table 3.2).

Figure 3.2 presents a graphical representation of the results in Table 3.2 and provides a comparison of global flux using the N00 scheme both with and without consideration of air resistance. Among the various DMS climatologies, the largest fluxes are produced by L10, VS07, MI09, and AN01; while the smallest fluxes are produced by AT04, PlankTOM and PISCES. For the N00 scheme, it is found that flux decreases by 7% on average when air resistance is considered (solid diamonds),

Table 3.2: Global total DMS flux estimates computed for available DMS concentration fields and various piston velocity formulations.*

	Piston schemes			
DMS fields	LM86	N00	W92	Total range
K99	16.0	22.6	28.0	16.0-28.0
K00	15.4	21.8	26.9	15.4-26.9
L10	17.9	25.3	31.2	17.9-31.2
AN01	17.8-18.1	25.1-25.3	31.3-31.8	17.8-31.8
BE04	12.6-13.6	17.7-19.1	21.9-23.6	12.6-23.6
AU02	13.2	18.6	23.1	13.2-23.1
SD02	12.6-18.7	17.8-26.5	22.0-32.7	12.6-32.7
HadOCC	15.2	21.6	26.6	15.2-26.6
AT04	8.8-17.8	12.5-25.3	15.4-31.1	8.8-31.1
VS07	16.0-19.0	22.7-27.0	28.0-33.2	16.0-33.2
MI09	16.9-19.3	24.0-27.3	29.5-33.6	16.9-33.6
HAMOCC	15.0	21.2	26.1	15.0-26.1
PlankTOM	12.3	17.4	21.6	12.3-21.6
PISCES	12.4	17.5	21.7	12.4-21.7
Total range	8.8-19.3	12.5-27.3	15.4-33.6	8.8-33.6

* Units are TgS y^{-1}. The acronyms of the DMS fields and piston velocity formulations are defined in Chapter 2 and 3, respectively. For empirical algorithms, a range of possible integrated fluxes were chosen instead of a single value given different input fields. All flux estimates were derived without accounting for air-side resistance.

with little variation among concentration fields. In contrast, considerable variability is associated with the choice of piston scheme or DMS concentration field. In Figure 3.2, the grey shaded band illustrates the wide range of fluxes for a single piston scheme (the N00 & γ_a scheme) across the available DMS concentration fields. The range of fluxes among the available piston schemes for any given DMS concentration climatology is similar or larger.

The grey band darkens toward the flux produced by L10 so that flux estimates can be seen in relation to this climatology, which this study considers to be the observation-based standard. From the results in Chapter 2, it can be argued that greater confidence can be placed on the L10-derived flux estimate than any of the others. Flux estimates differing more from L10 value therefore might be interpreted with greater skepticism. Note that L10 is also the field that yields the greatest flux when the N00 & γ_a scheme is used.

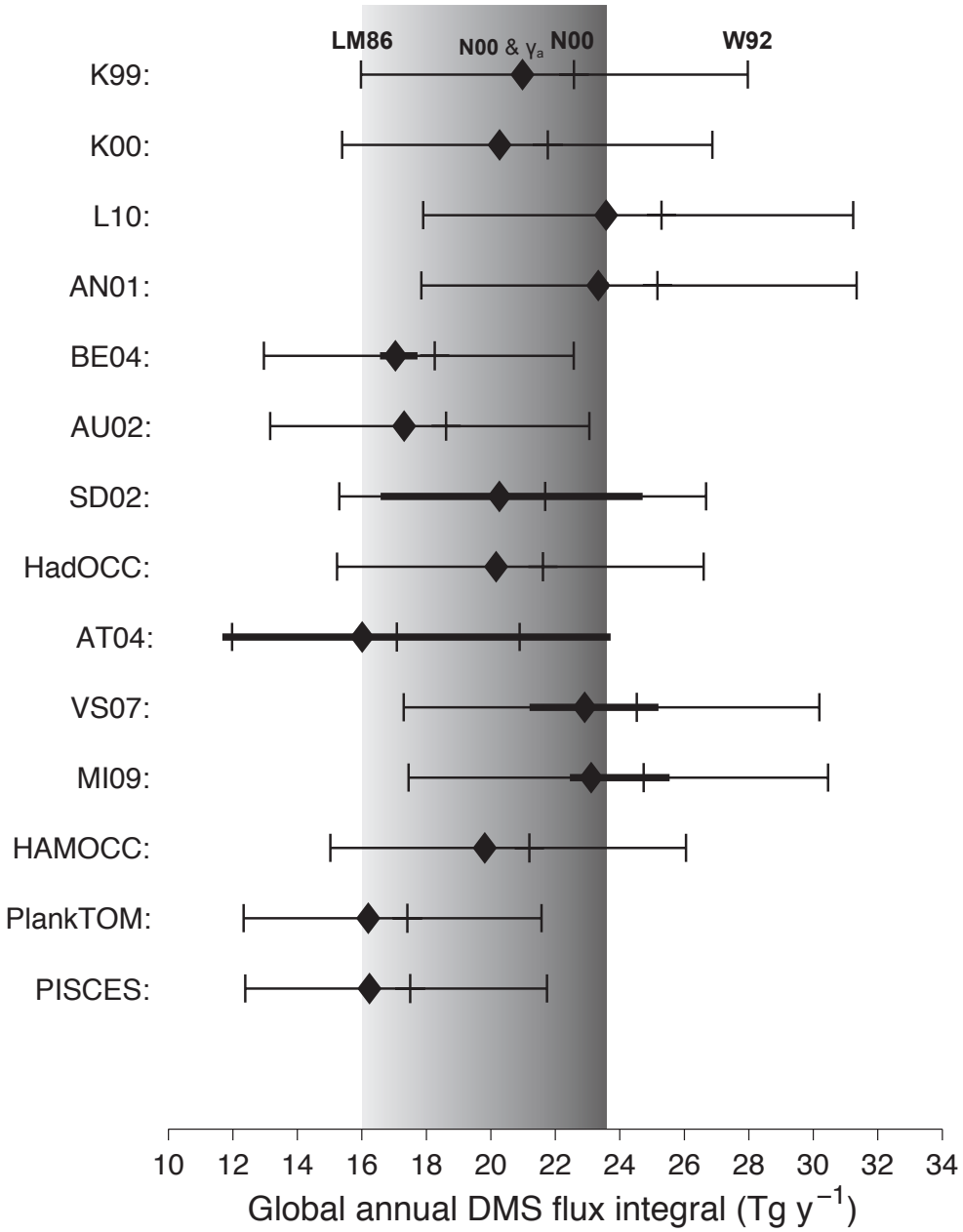

Figure 3.2: Global annual integrated DMS flux ranges resulting from the wind parameterizations of LM86, W92, and N00 for each of the DMS concentration fields. The vertical ticks of the horizontal lines denote the global flux estimate for each of the three wind parameterizations (without air resistance). The diamond denotes the flux estimate given N00 with consideration of air resistance (N00 & γ_a, as described in Section 3.2.1). Bold lines around the diamond of algorithm-based DMS fields represent the range of flux estimate given various input fields. The gray shaded band displays the range of fluxes for N00 & γ_a across the available DMS concentration fields.

In the present study, the re-estimation of AN01 algorithm parameters with new data (Figure 2.1), did not appreciably change the correlations between the original AN01 DMS concentration field and the observations (GSS database) or L10 (see Table 2.4). The new AN01 algorithm does, however, yield a flux estimate that is very close to the L10 estimate, mostly because the high baseline value of 2.29 nM has been eliminated. Woodhouse et al. (2010) used the original AN01 (among other fields) to simulate DMS flux, noting the particularly high fluxes that were produced with the original AN01 algorithm. With the new AN01 algorithm, flux estimates are improved in the global total flux, though not in spatial pattern.

For the empirical algorithms, thicker lines around the diamonds in Figure 3.2 denote ranges in DMS flux (obtained using N00 & γ_a) resulting from different input fields for the DMS algorithm. SD02 and AT04 yield the greatest range in annual flux estimates. The smallest flux estimates from these algorithms occur when CanESM2 MLD is used as an input field. However, this low estimate could partly be due to the use of regression parameters estimated for the observation-based MLD by de Boyer Montégut et al. (2004). Refitting the AT04 formulation to the CanESM2 MLD data result in a flux that is greater by $\sim$20% (not shown). However, for consistency the same equation (MLD$\times$DMS = 56) was applied for AT04, irrespective of what input fields are used. This is also true for the SD02 algorithm.

Using the same equation with different inputs has been done in previous studies (e.g., Halloran et al., 2010). In HadOCC, the SD02 algorithm is used to derive DMS from simulated MLD and chlorophyll. Originally, the SD02 algorithm was constructed using observational data. However, there was no retuning of the SD02 regression within the HadOCC model, as explained in Section 2.2.2.3. Parameterizations that had their parameters retuned to the specific input fields used (VS07, MI09) give generally a more constrained range in flux estimates than those that did not (SD02, AT04). As noted above, retuning the parameters also increases the flux somewhat for AT04. These large deviations in flux estimates just due to the use of unoptimized algorithms should be considered when using algorithms such as SD02 or AT04 in a model.

A scatterplot of integrated flux (calculated using N00 & γ_a) versus global- and annual mean DMS concentrations shows a roughly linear relationship between these two quantities (Figure 3.3). The small deviations demonstrate that the spatial and temporal structure of the concentration fields has some influence on the fluxes. For example, the fact that AN01 yields roughly the same flux as L10, despite having lower

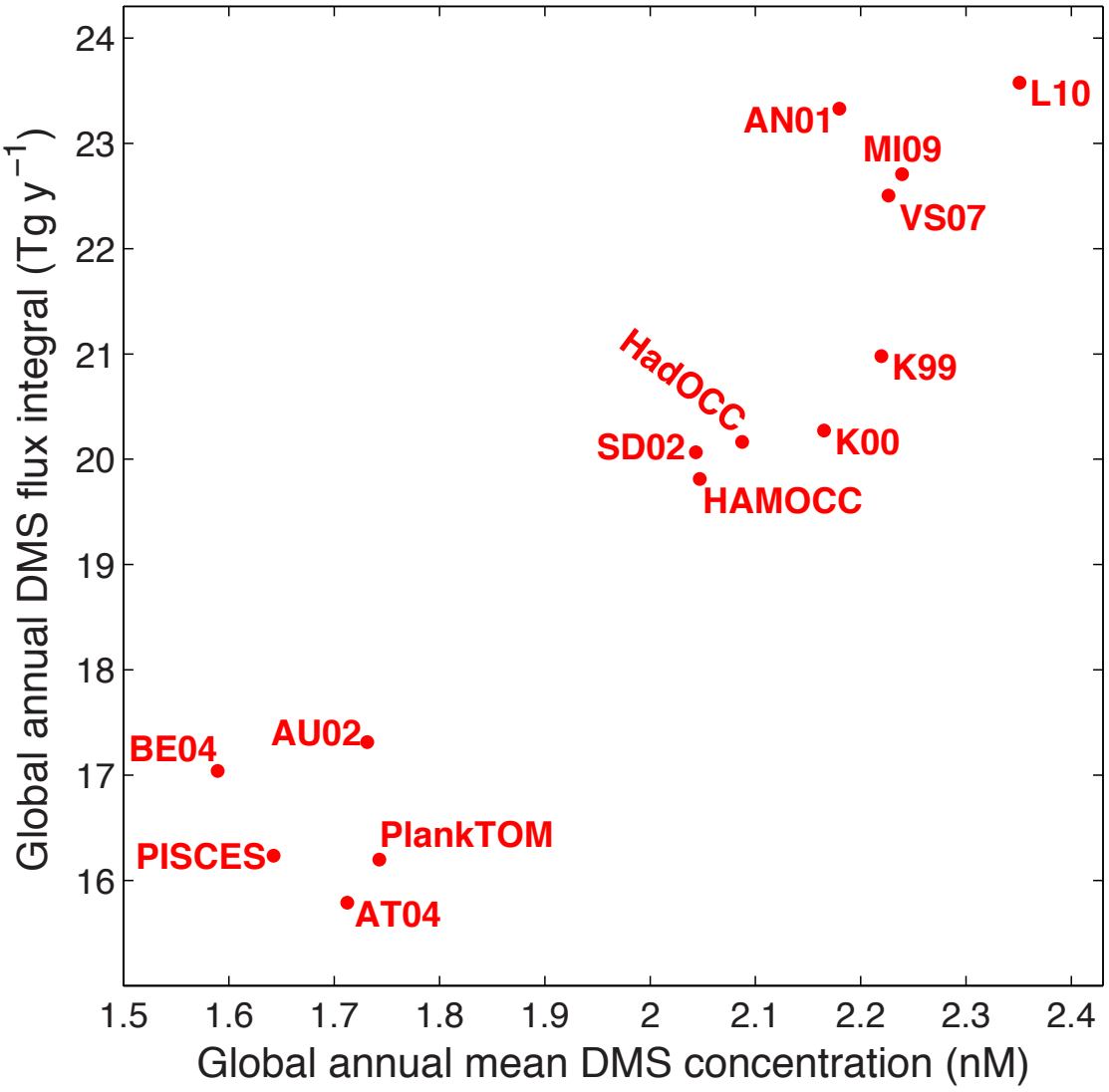

Figure 3.3: Global integrated DMS flux versus annual mean concentration as computed from different DMS concentration fields. All fluxes are calculated using the N00 & γ_a scheme.

mean concentration, implies that high concentrations and high wind speeds co-occur in AN01 more often than they do in L10. In general, however, the influence of spatial (and temporal) structure in the DMS concentration climatologies on global total flux appears to be minor.

Figure 3.4 depicts the relationship between annual- and global-mean DMS concentration and flux, for the different piston velocity schemes (LM86, N00, W92). The relationships are found to be qualitatively similar for the three schemes. The

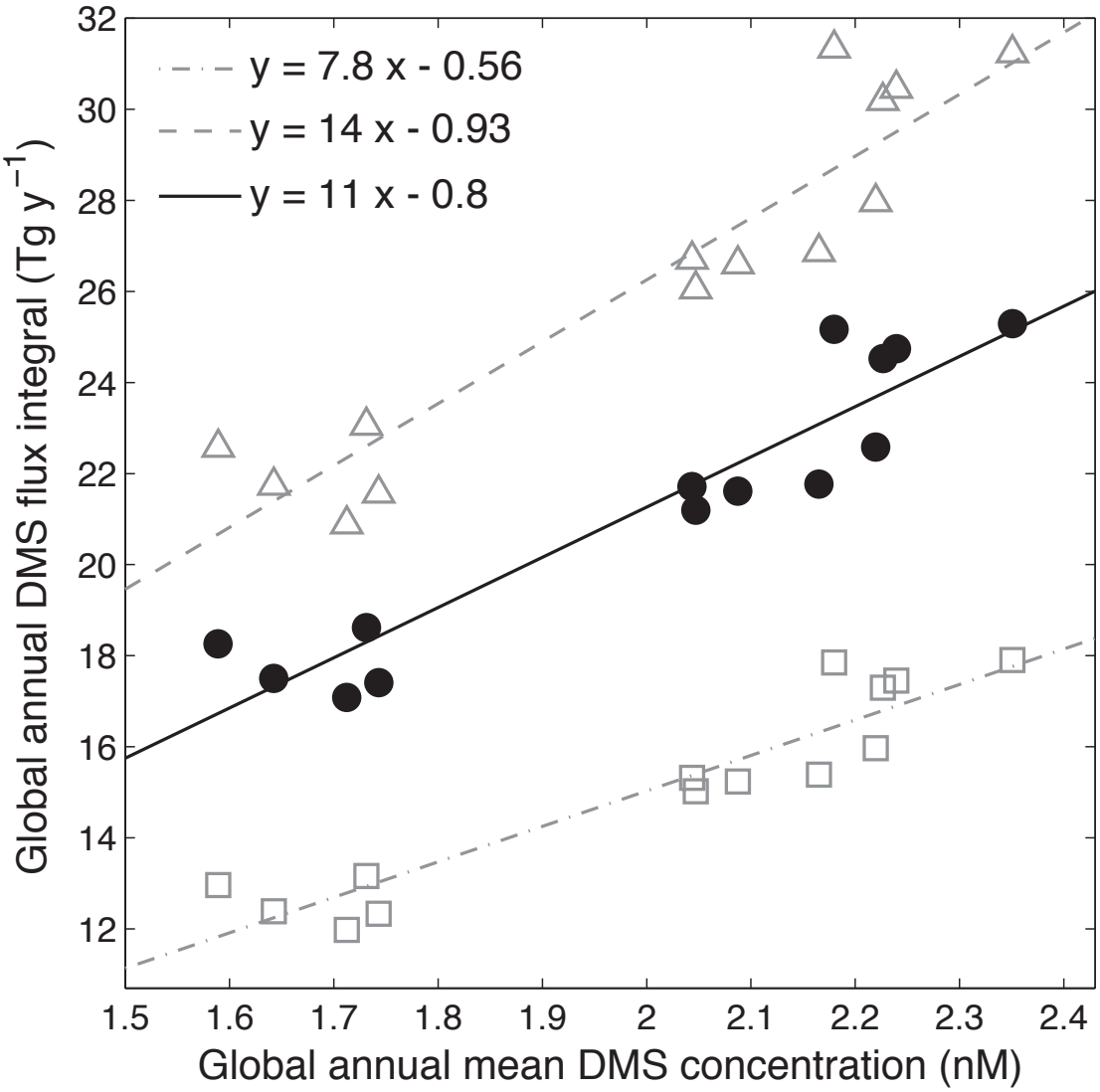

Figure 3.4: Global integrated DMS flux versus annual mean concentration as computed from different DMS concentration fields for the gas transfer parameterizations of LM86 (squares), W92 (triangles), and N00 (circles). All three cases ignore the effect of air resistance. Each case also includes a regression line showing the relationship between the different DMS concentration fields.

relationship is positive and linear in each case, but slopes vary from 7.8 (LM86) to 14 (W92). Fluxes increase per unit change in concentration most for W92 and least for LM86. Not only do flux integrals differ depending on which piston velocity formulation is used, these differences increase with DMS concentration.

Section 3.1 looked at flux variations occurring both due to difference in piston velocity parameterization and DMS concentration. The next sections in this chapter

focus on the intercomparison of flux fields derived from the concentration climatologies discussed in Chapter 2, such that the piston velocity parameterization can be held fixed. N00 & γ_a was chosen as the standard formulation since it can be considered most appropriate for DMS. First, N00 is the current choice for most DMS flux studies found in the literature, and secondly, air-side resistance should be considered when deriving DMS fluxes (McGillis et al., 2000).

3.3.2 The spatial distribution of annual mean flux derived from the different concentration fields

The flux of DMS to the atmosphere is computed as the product of the concentration of DMS and the gas transfer velocity, which is largely determined by wind speed and SST. Therefore spatial variability in the flux (Figure 3.5) results from variability in both the DMS concentrations and piston velocity. The concentration of DMS varies widely across different areas of the ocean (Chapter 2) accounting for a great deal of the variability of flux. For example, fluxes in the subtropics tend to be relatively small (except for BE04), whereas in the central equatorial Pacific, fluxes tend to be elevated (except for BE04, AU02 and PlankTOM). Although greater similarity is evident among flux fields than concentration fields, there are still considerable areas of disagreement. Broad regions such as the Subpolar North Atlantic and Pacific, the Eastern Equatorial Pacific, and the Southern Ocean show great differences in fluxes depending on what concentration field is used (Figure 3.5). HAMOCC and HadOCC are clear outliers with extreme annual mean values in the central and east equatorial Pacific.

Fluxes computed from L10 are clearly less patchy than those from the other observationally-based climatologies (K00 and K99). AN01 yields an annual mean flux field that is more homogenous than L10 and most of the prognostic models. AN01 shows a broad band of elevated flux between 40 and 60°S that likely is due to the presence of persistent high winds and elevated concentrations (relative to other climatologies). Similarly, VS07 and MI09 yield flux fields with broad regions of elevated annual mean fluxes. Comparing annual mean concentration maps in Figures 2.11 through 2.14 and flux fields in Figure 3.5, it can be observed that most regions of high concentration are also regions of high flux. However, high concentration adjacent to Antarctica (as seen in L10, AN01 or PISCES) does not yield high annual mean fluxes due to the presence of ice cover suppressing the flux for much of the year.

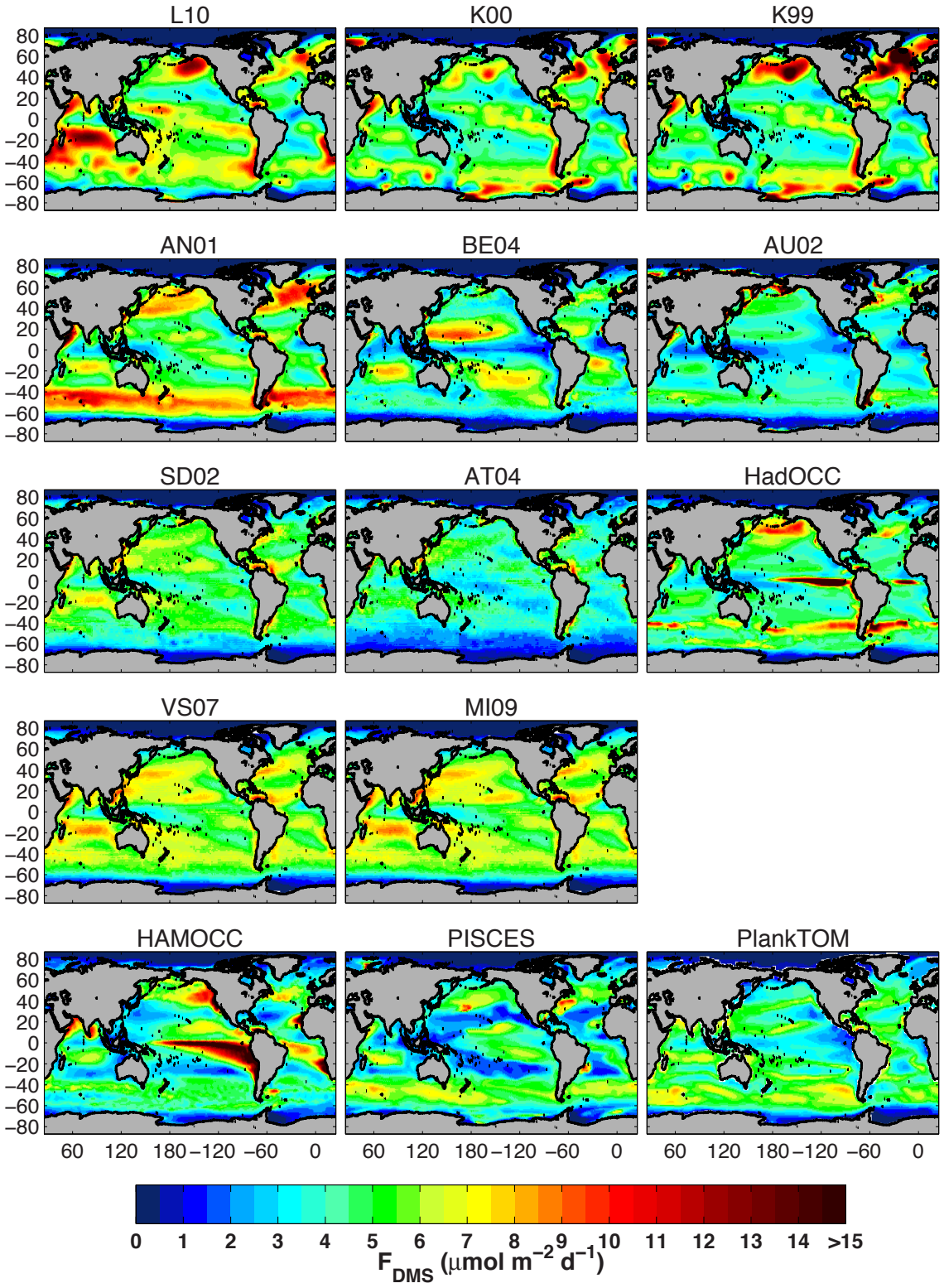

Figure 3.5: Global maps of the annual mean flux of DMS from each of the DMS concentration fields using N00 & γ_a.

The chlorophyll-based climatologies (AN01, AU02, SD02, AT04) seem to show greater fluxes in coastal upwelling regions and on the continental shelves (Figure 3.5). However, these areas constitute only a small percentage of the whole ocean surface, so even with these larger concentrations the contribution of DMS from continental shelves to the global total flux is relatively small. The observational climatology, L10, gives no indication that either DMS concentration or flux is higher in coastal regions as compared to the open ocean.

3.3.3 Comparison of DMS flux fields versus L10 and observations

A Taylor diagram of flux fields with L10 as a reference (Figure 3.6a) shows that the disagreement in spatial and temporal pattern with L10 (as measured by pattern correlation) is similar for both the flux and concentration fields. However, the variance does not differ by orders of magnitude as was the case with the concentration fields (see Section 2.3.4). In terms of correlation and RMS error, the DMS flux fields that are derived from the earlier observation-based climatologies (K99 and K00) agree no better with L10 than the flux fields that are derived from most of the reconstructions and models (Figure 3.6a). This is striking given that the data used to create K99/K00 makes up close to one-third of the data that were used to construct L10.

Figure 3.6b displays a Taylor diagram with DMS flux derived from the GSS database as the reference. In comparison with GSS derived flux estimates, L10 clearly outperforms the other fields, but there is still some disagreement ($r = 0.7$). K99 and K00, on the other hand, do not clearly outperform any of the fields using either L10 or the observations as the reference. The relatively good performance of L10 is not surprising given that it was obtained from the GSS data.

Figure 3.7 shows relative frequency distributions (as percentage of ocean surface area) of DMS concentration and flux for L10, K00, K99, AN01, AT04 and VS07. For each field, the upper panel shows the frequency distribution of DMS concentration, while the lower panel shows the frequency distribution of the computed flux. The frequency distributions of the individual observations (GSS) are represented with a black line in each panel. The subset of DMS concentration climatologies was chosen to represent the range of differences between the observational data set and the climatologies for both concentration and flux distribution.

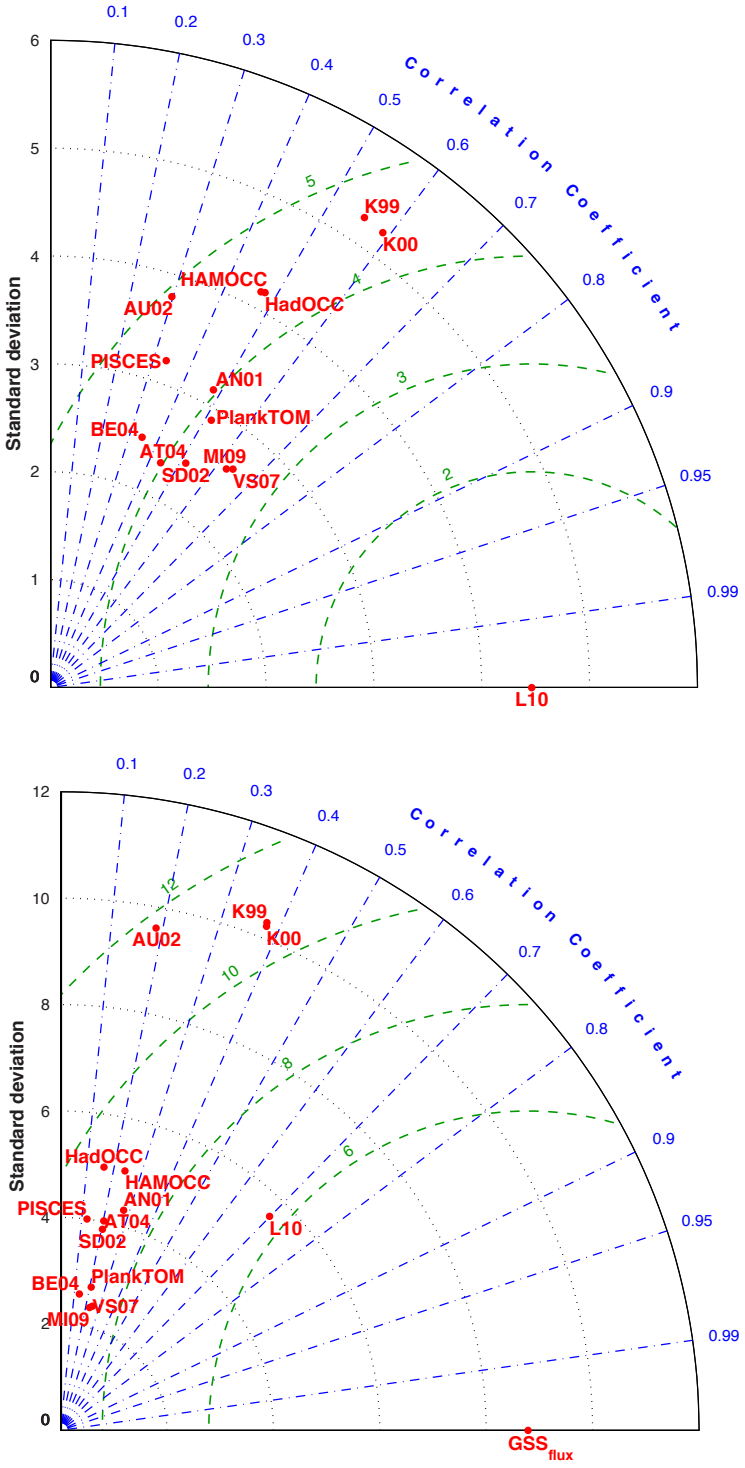

Figure 3.6: Taylor diagrams describing the total space-time variations of DMS flux fields obtained from each of the DMS concentration fields, tested against (a) the L10 flux field and (b) the flux dataset derived from the GSS observations. All fluxes are calculated using the N00 & γ_a scheme.

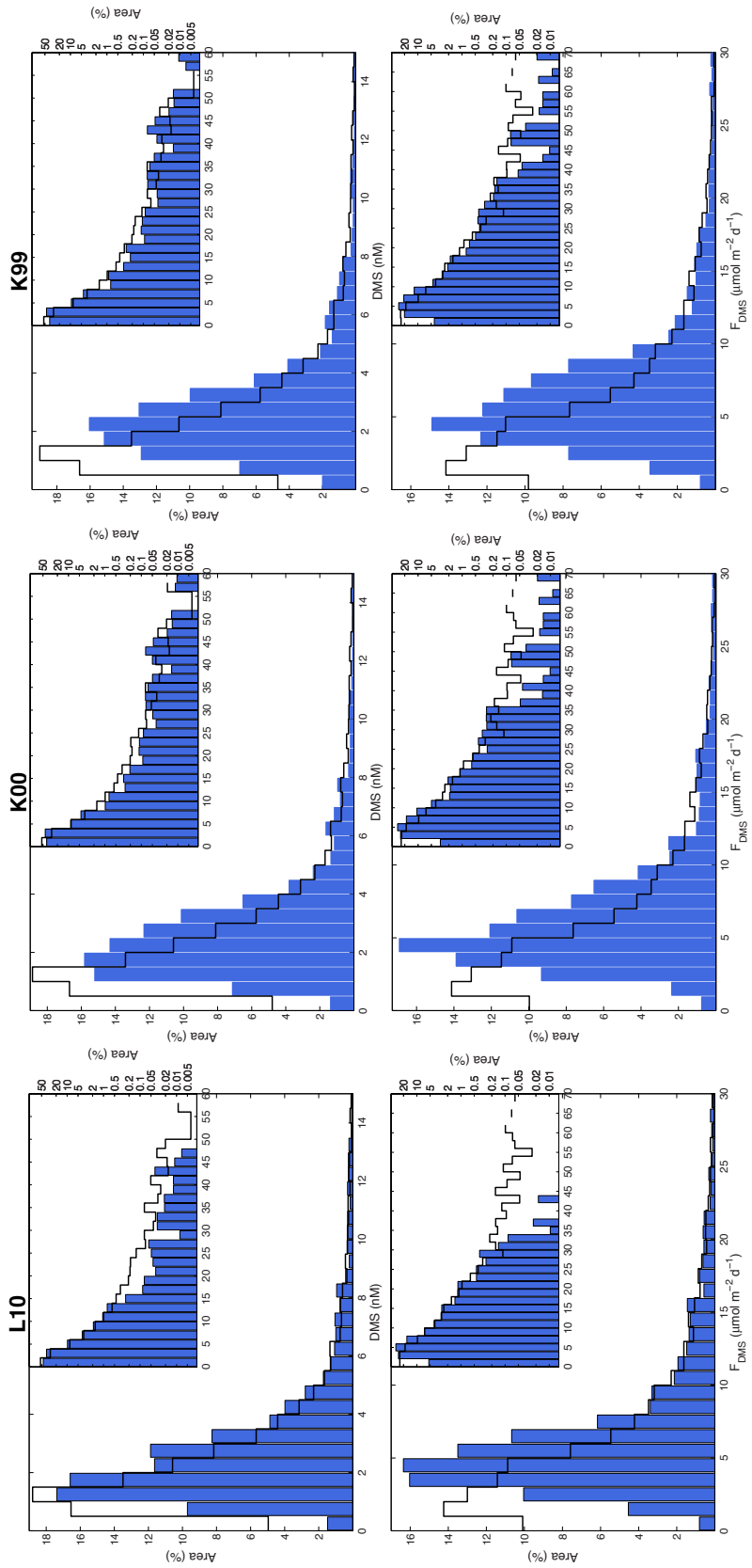

Figure 3.7: Frequency distributions of DMS concentration and DMS flux as a percentage of surface area for a subset of DMS climatologies. For each field, the upper panel depicts the distribution of DMS concentration. The lower panel depicts the distribution of DMS flux, calculated under the N00 & γ_a scheme. Note that only data is shown from grids where observations are available. The blue bars outline the histogram of the concentration/flux as given by the dataset stated in the title. In each panel, the corresponding frequency distribution of the observational dataset is shown by the black line. Also, the insets of each panel are redrawn such that the vertical axes are scaled logarithmically and the horizontal axes and bars are widened. For the upper panel, main and inset bars have width of 0.5 and 2 nM, respectively. For the lower panel, main and inset bars have width of 1 and 2 μmol m^{-2} s^{-1}, respectively.

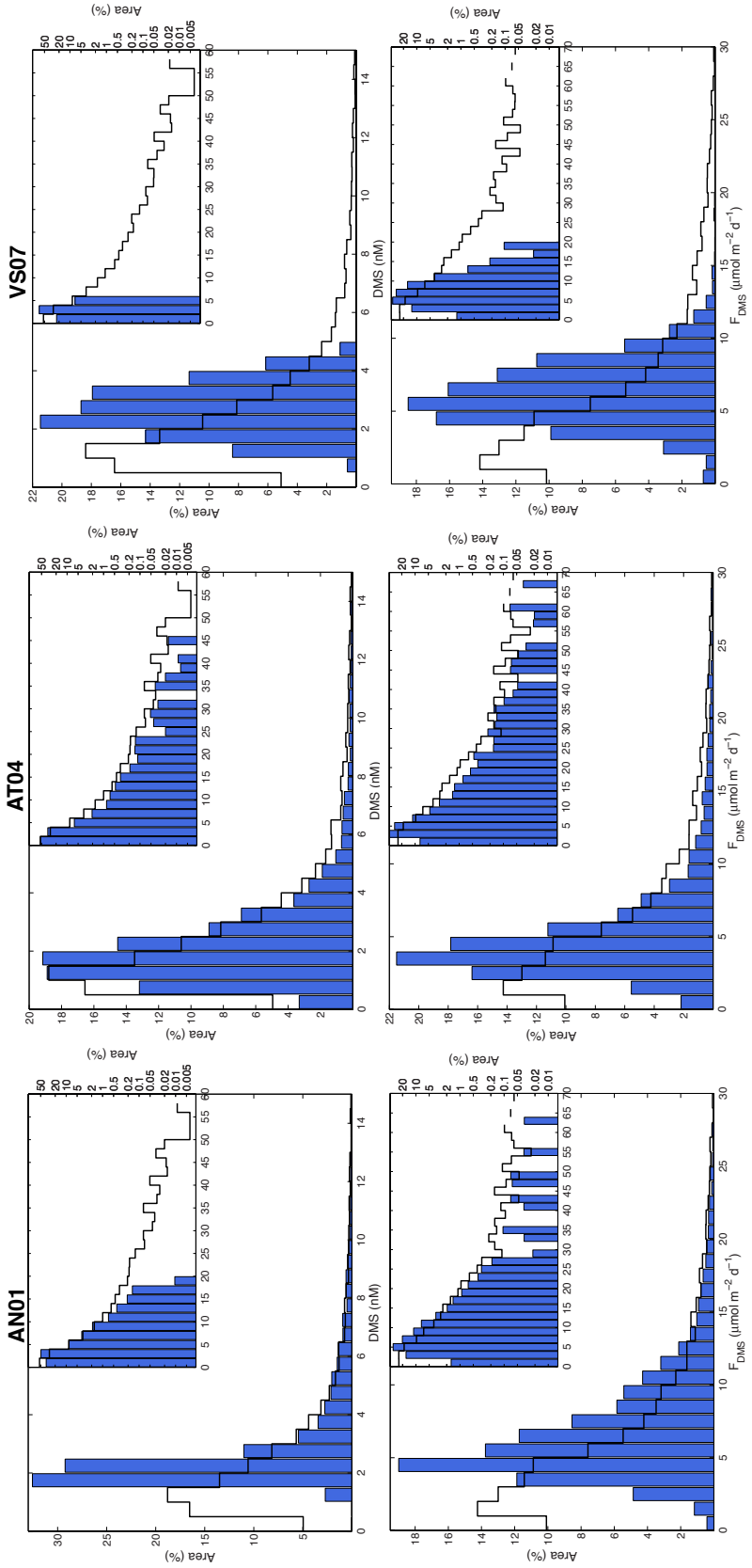

Figure 3.7 (continued).

The climatologies have narrower distributions than the individual observations. For example, L10 underestimates the frequency of occurrence of concentrations of 0 to 1.5 nM and 14 to 60 nM, while in the mid-range, 1.5 to 5 nM, L10 overestimates the frequency of occurrence of DMS concentrations in this range. This reduction in range might partly be explained by data extrapolation techniques that average low and high concentrations, and concentrate the data toward the middle of the range. These differences are more pronounced for the flux distributions. The L10 distribution clearly peaks at a higher flux (4-5 μmol m^{-2} d^{-1}) than the flux derived from the observations (1-2 μmol m^{-2} d^{-1}).

The narrowing of concentration and flux ranges is greatest for AN01 and VS07 which both fail to capture a large portion of the range that is seen in the observations. The frequency distribution of AN01 derived DMS matches with observations for intermediate concentrations between 3 nM and 10 nM, but fails to produce concentrations below 1 nM or above 20 nM. The parameterized DMS concentration of VS07 does not show concentrations higher than 5 nM, but does not show such a narrow peak in DMS as shown in AN01 (Figure 3.7). The narrow frequency distribution for AN01 and VS07 are consistent with the high degree of spatial homogeneity shown in the concentration maps (Figure 2.11). Among the algorithms, AT04 best matches the observations, but the match with the flux distribution is not as good. In all cases, the mismatch between climatology/reconstruction and observed distributions is greater for fluxes than for concentration (Figure 3.7).

Comparing the frequency distributions for concentration and flux is also useful for understanding the representativeness of regions with relatively large concentrations. The observational dataset includes very high concentrations that are usually linked to brief events, such as phytoplankton blooms. None of the DMS fields (except K99 and K00) show such extreme values (Figure 3.7 insets). Similarly, extreme fluxes are not reproduced. The best match between the observations and the climatology is given, not surprisingly, by L10, though it does not capture observed extremes as well as K00 and K99 do, particularly for fluxes. Comparing the top and bottom panels for each climatology, the overall shape of the frequency distributions are similar between concentration and flux.

Note that the frequency distributions characterize only the range and relative frequency of concentrations and fluxes, and not the spatial or temporal patterns. While the AT04 distribution matches the observations relatively well, the correlation is no better than for other climatologies (Figures 2.16, 2.20 and 3.6). Although L10 best

matches the observations (Chapter 2), Figure 3.7 shows that L10 still underestimates the frequency of occurence of high concentrations as compared to the observational dataset.

3.4 Discussion

As discussed in the previous chapter, one of the limitations of L10 is its relatively coarse spatial resolution. DMS concentration measured in the ocean is highly spatially variable. However, L10 clearly has spatial concentration features that spread out over hundreds of kilometres. Essentially, climatologies tend to have a lot of extreme values in places where observations have been made. Actual DMS distributions are likely to be highly spatially (as well as temporally) variable and show variability even at very fine scales (Asher et al., 2011). Estimating the global flux of DMS from spatially and temporally variable observations of DMS remains a significant challenge. The use of climatological averages and extrapolations into data-sparse regions might affect the ability of climatological fields to estimate the global DMS flux (Figure 3.7). In order to assess the skill of DMS concentration derived global flux estimates, one needs to test these with actual measurements of DMS flux.

Figure 3.3 suggests that to first order it is the global mean concentration of DMS that primarily determines the global mean flux, while the spatial and temporal distribution of DMS is of secondary importance. The climatologies (K99, K00 and L10) show a pronounced seasonality, which none of the reconstruction approaches reproduce. As well, the DMS distributions from most of the empirical algorithms have much less spatial variability than the climatologies (Figure 2.11). In terms of the global atmospheric sulfur budget, it is an important result that these spatial and seasonal differences have a small effect on global mean estimates of flux (Figure 3.3). However, the spatial structure of DMS flux influences global climate through local changes in CCN concentration (Woodhouse et al., 2013). In the next chapter, a global atmospheric model will be used to test what effect the variation in spatial and temporal distribution of DMS concentration has on sulfate aerosol burdens and radiative fluxes (and thus climate).

Considering all available DMS concentration fields (reconstructed and modelled), a wide range of global mean flux estimates was derived (Table 3.2 and Figure 3.2) which can be used to define boundary conditions for an atmospheric GCM. It is noteworthy that L10 is at the high end of the range of DMS flux estimates. This

result has implications for the interpretation of previous sensitivity studies that used K00 or simulated/parameterized DMS concentration. Using L10 versus other DMS fields, one should expect a greater sensitivity to changes in wind patterns, for example (Figure 3.4). Consequently, the importance of DMS for climate might be greater than was previously estimated. Given the variable global annual mean concentrations of the different climatologies, future projections of global climate will depend on which climatology is used.

The sensitivity of the integral flux to differences in the input fields and to the reestimation of algorithm parameters when using different input fields indicates potential problems if algorithms are used with input fields other than those on which the parameter estimates were based. For example, in the case of MLD, this study has shown that it is problematic to apply the same equation (estimating DMS as a function of MLD) irrespective of which MLD climatology is used.

It is important to call attention to the need for more realistic gas transfer formulations in climate models. There is a lot of uncertainty concerning the sea-air transfer of DMS. The formulations used in this study are generally empirical and better models are needed that are based on actual physical processes (Elliott, 2009; Fairall et al., 2000, 2011; Garbe et al., 2014; Hare et al., 2004; Johnson, 2010; Yang et al., 2011). Transfer velocity formulations are empirical formulations based on observations, and are only as good as the observational data that was used to construct them. A more realistic way to derive DMS fluxes is to have a more physical approach, meaning that processes are actually modelled (with no direct dependency on observations). However, the implementation of such physical models (instead of the empirical transfer parameterizations) is still preliminary and not really feasible for global DMS simulations. Nonetheless, using such physical approaches is the ultimate goal in terms of modelling the DMS flux. Elliott (2009) argues that a piecewise composite between LM86 and W92 is a first step towards a more physical representation of the transfer of DMS through the air-sea interface, because it conforms better to novel eddy covariance studies on DMS (e.g., Blomquist et al., 2006; Huebert et al., 2004).

Chapter 4

Simulation of DMS fluxes: Model sensitivity

4.1 Introduction

The previous chapters demonstrated that there are large differences in DMS sea surface concentration between different climatologies (Chapter 2), and that these differences can cause substantial variation in flux (Chapter 3). The next question is the implication of these differences for the global climate. Although DMS fields show large differences in spatial pattern and seasonality, the differences in global and annual mean fluxes are considerably smaller and the climate impacts may also be smaller. Such a question is naturally addressed using a climate model. Using different DMS concentration fields as boundary conditions, the resulting changes in tropospheric chemistry and radiative forcing can be assessed and differences between different DMS flux estimates can be put in a climate perspective. Previous modelling studies focused on the effect of DMS on aerosol, CCN and radiative forcing by scaling a single DMS field (e.g., Gunson et al. (2006); Thomas et al. (2011)). However, there has not been much discussion on the climatic effect of spatial and temporal variations of DMS flux (Woodhouse et al., 2013). Part of this chapter evaluates the importance of spatial and temporal structure of a DMS concentration field to model climate forcing.

Prior to this work, the operational version of the Canadian GCM still derived ocean emissions of DMS using the old K99 climatology. Integrating the updated L10 climatology into the latest version of the Canadian Earth System Model (CanESM2) provides the opportunity to contrast the older model configuration with K99 to new

model boundary conditions and new gas transfer formulations. For this study, several AGCM runs were done using different DMS concentration fields including L10 as the control field. Simulations with different transfer velocities were also performed.

The K99 climatology (and to some extent L10) shows large scale features and "bulls-eye" maxima that may reflect incomplete sampling rather than physical or biogeochemical processes. However, whether these fine scale features are important in a global climate simulation remains uncertain, given the large-scale structure of the winds which drive the fluxes and the subsequent transport and oxidation to sulfate aerosol. Alternate DMS concentration fields were also designed for this study to shed light on the importance of spatial and temporal structure in DMS in determining effects on the marine aerosol burden and radiative fluxes. In order to test the effect of seasonality the L10 field was replaced by an annual-mean climatology. This study also examines the effect of spatial variability within the DMS concentration by replacing spatially variable fields with their spatial means. Analyzing the effects of seasonal and spatial variations in DMS opens up a new perspective on climate sensitivity to DMS.

4.2 Methods

4.2.1 Model description

All model simulations presented in this study were made with the fourth generation Canadian Atmosphere Model (CanAM4.1). CanAM4.1 is a slightly newer version of CanAM4, which is described in von Salzen et al. (2013). Differences between the two model versions are mainly due to improved diagnostic capabilities in CanAM4.1. The model has a horizontal resolution that is defined spectrally with a triangular truncation at wave number 63 (T63) for dynamic transport (i.e. advection) and with a 128-by-64 linear grid for computing physical terms. The vertical domain of the model has 49 layers extending from the surface to 1 hPa. The vertical grid spacing is about 100 m at the surface and then monotonically increases at higher altitudes.

Figure 4.1 presents a schematic of the sulfur cycle and the radiative effects of sulfate aerosols in CanAM4.1. The ocean efflux of DMS is a source of aerosols via oxidation to sulfur dioxide (SO_2), which in turn is oxidized to form sulfuric acid (H_2SO_4) and sulfate (SO_4^{2-}). The air-sea gas transfer of DMS is calculated with SST, ice cover, and wind speed from the model. Ice cover and SST are specified in all model runs used here with a climatological dataset from the Atmospheric Model Intercomparison

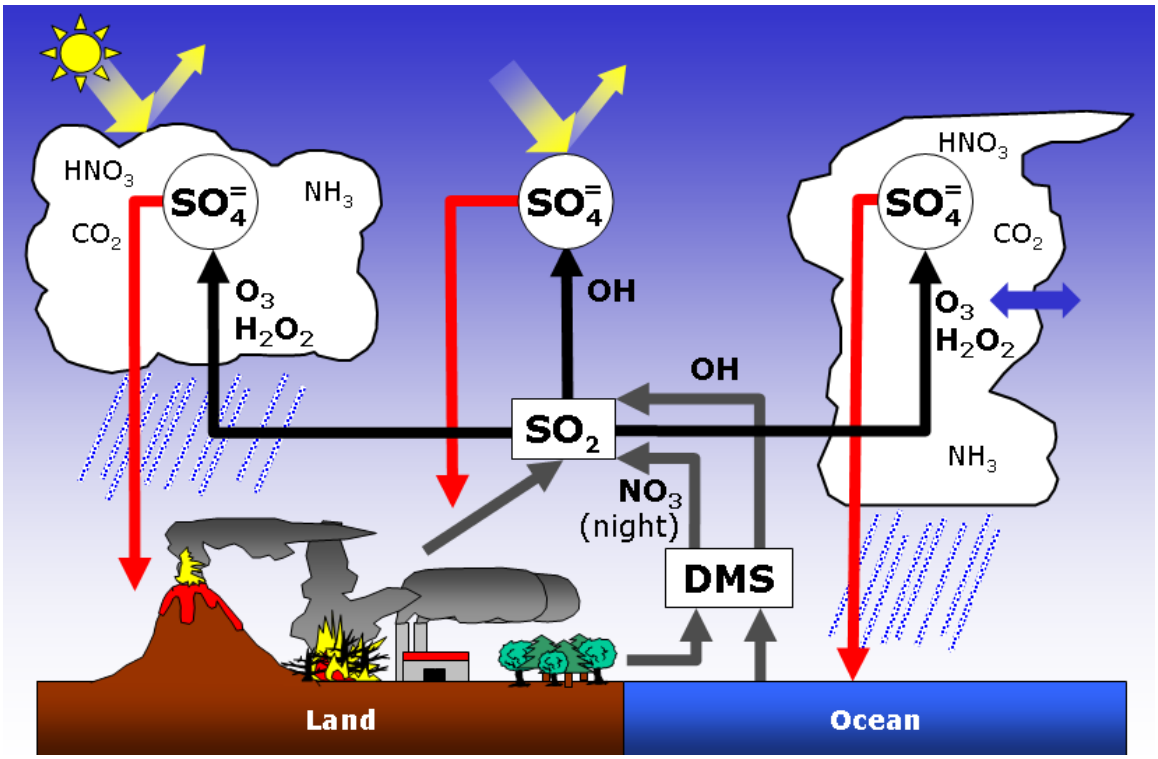

Figure 4.1: Schematic representation of the sulfur cycle and radiative effects of sulfate aerosols in CanAM4.1 (courtesy of Knut von Salzen). In each grid cell, the model accounts for sources and sinks of sulfate aerosol (SO_4^{2-}), SO_2 and DMS. SO_2 is emitted from volcanos, fires, and anthropogenic sources. DMS is mainly emitted from the oceans but there are also some terrestrial sources. DMS is oxidized to SO_2 by OH during the day and by NO_3 during the night. In clear-sky conditions, SO_2 is oxidized to sulfuric acid which can either form new sulfate particles by nucleation or condense onto existing particles. In clouds, sulfate is produced from in-cloud oxidation of SO_2. In-cloud oxidation of sulfur and wet deposition is treated separately for layer (i.e., stratiform) and convective clouds. For both types of clouds, the oxidation occurs via ozone (O_3) and hydrogen peroxide (H_2O_2). The oxidation rates depend on the pH of the cloud water which depends on the concentrations of nitric acid (HNO_3), ammonia (NH_3), and carbon dioxide (CO_2). Sulfate aerosols are mainly removed by wet deposition, with dry deposition being only a minor sink term.

Project (AMIP) (Hurrell et al., 2008). In addition to the ocean efflux, the model also accounts for DMS fluxes from the terrestrial biosphere, which are given as monthly mean fields (Spiro et al., 1992). DMS is oxidized to SO_2 by hydroxyl radicals (OH) during daylight hours and by nitrate radicals (NO_3) at night. Besides DMS, the model also includes additional terrestrial sources of sulfur to the atmosphere (Figure 4.1): monthly mean emissions of gas phase SO_2 from fires (i.e., biomass burning) and

anthropogenic sources (Lamarque et al., 2010), as well as from volcanic emissions (Dentener et al., 2006).

Transport, dry and wet deposition, as well as chemical transformations of the constituents are all calculated by CanAM4.1. In terms of the production of sulfate aerosol (SO_4^{2-}), there is in-cloud and gas-phase (clear-sky) oxidation of SO_2. However the main source of sulfate aerosols in the atmosphere is in-cloud oxidation, which differs in some ways for layer (i.e., stratiform) and convective clouds. The presence of ozone (O_3) and hydrogen peroxide (H_2O_2) as oxidants is a requirement for both types of clouds (von Salzen et al., 2000). As seen in Table 4.1, the concentrations of nitric acid (HNO_3), ammonia (NH_3) and carbon dioxide (CO_2) affect the pH of cloud water and as a consequence the oxidation rates (von Salzen et al., 2000). The formulation from Slingo (1987) is used, which calculates the fraction for in-cloud oxidation in the condensed phase via the precipitation flux. Under clear-sky conditions, OH radical is the only oxidant of SO_2. There is no fully interactive chemical transport module, so that CanAM4.1 uses specified oxidant concentrations (OH, NO_3, O_3, H_2O_2) from the Model for Ozone and Related Chemical Tracers (MOZART) as presented by Brasseur et al. (1998). CanAM4.1 also specifies ammonia (NH_3) and ammonium (NH_4^+) concentration (Dentener and Crutzen, 1994), which are used for the calculation of pH. Table 4.1 summarizes the relevant chemical reactions included in CanAM4.1 (von Salzen et al., 2013).

The removal of sulfate aerosol takes place through wet and dry deposition. The dry deposition flux of sulfate simply depends on the concentration within the model layer adjacent to the surface along with a defined dry deposition velocity (Lohmann et al., 1999). Wet deposition, as with the in-cloud oxidation outlined above, is treated individually for layer and convective clouds. For convection there is scavenging within clouds, which is a function of precipitation Giorgi and Chameides (1986), as well as scavenging underneath clouds by falling rain droplets, which is parameterized using a mean collection efficiency (Berge, 1993). Wet deposition is the main and more efficient process in removing sulfate aerosol, so precipitation is an important control on the sink of sulfate.

CanAM4.1 uses a bulk aerosol scheme, which means that there is no information on aerosol size distribution, but only the total mass. The model defines sulfate, organic carbon, black carbon, sea salt, and dust as separate aerosol species (Croft et al., 2005; Lohmann et al., 1999). CanAM4.1 includes data by the Aerosol Comparisons between Observations and Models (AeroCom) project for natural and anthropogenic aerosol

Table 4.1: Chemical reactions included in the model (from von Salzen et al. (2013)).

Reaction	Rate Coefficient or Equilibrium Constant†	Unit	Reference
	Gas Phase Reactions		
$DMS + OH \longrightarrow SO_2$	$9.6 \times 10^{-12} \exp(-234/T)$	$cm^3\ molec^{-1}\ s^{-1}$	Atkinson et al. (1989)
$DMS + NO_3 \longrightarrow SO_2$	$1.9 \times 10^{-13} \exp(500/T)$	$cm^3\ molec^{-1}\ s^{-1}$	DeMore et al. (1992)
$SO_2 + OH \longrightarrow H_2SO_4$	$a_0 \times m/(1 + a_0 \times m/a_\infty) \times 0.6^{[1./(1.+\log(a_0 m)/a_\infty)^2]}$ with $a_0 = 3 \times 10^{-31} \times (300/T)^{3.3}$ and $a_\infty = 1.5 \times 10^{-12}$	$cm^3\ molec^{-1}\ s^{-1}$	Pham et al. (1995)
	Equilibrium Reactions		
$SO_2(g) + H_2O(aq) \longleftrightarrow SO_2(aq)$	$1.23 \times 3120(1/T - 1/298)$	$M\ atm^{-1}$	Chameides (1984)
$SO_2(aq) \longleftrightarrow H^+ + HSO_3^-$	$35.53(1/T - 1/298)$	$M\ atm^{-1}$	Chameides (1984)
$HSO_3^- \longleftrightarrow H^+ + SO_3^{2-}$	6.72×10^{-5}	$M\ atm^{-1}$	Chameides (1984)
$O_3(g) + H_2O(aq) \longleftrightarrow O_3(aq)$	$29.44(1/T - 1/298)$	$M\ atm^{-1}$	Chameides (1984)
$H_2O_2(g) + H_2O(aq) \longleftrightarrow H_2O_2(aq)$	6.4×10^8	$M\ atm^{-1}$	Chameides (1984)
	Aqueous Phase Reactions		
$S(IV) + H_2O_2 \longrightarrow S(VI) + H_2O$	$8 \times 10^4 \exp[-3650(1/T - 1/298)](0.1 + [H^+])^{-1}$	$M\ s^{-1}$	Martin (1984)
$S(IV) + O_3 \longrightarrow S(VI) + O_2$	$4.4 \times 10^1 \exp(-4131/T) + 2.6 \times 10^3 \exp(-966/T)[H^+]^{-1}$	$M\ s^{-1}$	Maahs (1983)

† T: temperature in K, m: air density in molec cm^{-3}.

emissions (e.g., Kinne et al., 2006; Textor et al., 2006). In the CanAM4.1 version used in this study the cloud droplet number concentration (CDNC) depends only on the local concentration of sulfate. The empirical parameterization by Dufresne et al. (2005) is used which relates CDNC to the concentration of sulfate as:

$$CDNC = 60(SO_4^{2-})^{0.2} \tag{10}$$

where CDNC is in number cm^{-3} and SO_4^{2-} in $\mu g\ m^{-3}$. For this relationship, a lower bound on CDNC of 1 cm^{-3} is used.

CanAM4.1 calculates the direct radiative effect of scattering by aerosols and the first indirect radiative effect due to interactions with clouds, influencing cloud optical properties. Effects of aerosols on the conversion of cloud water to precipitation (second indirect effect) are not considered in the current version of CanAM4.1. In terms of the direct effect, calculations account for scattering and absorption using the Mie solution approach. The main input parameters for the calculations are aerosol mass and relative humidity. Sulfate aerosols scatter radiation more efficiently at higher relative humidity because aerosols swell in size with relative humidity to establish thermodynamic equilibrium according to Raoult's law. The overall efficiency of the scattering effect also varies with wavelength and concentration of aerosol. In general, the net clear-sky radiative effect should be roughly proportional to the aerosol burden. The first indirect effect uses the relationship between sulfate aerosol and cloud droplet number concentration (CDNC) as described above, which is used to determine the effective radius of cloud droplets. Smaller droplets are more efficient at scattering solar radiation than larger droplets. Given the much greater cloud fraction of stratiform clouds compared to convective clouds, the indirect effect only is applied in layer clouds. Within each grid cell, the cloud forcing is determined as the difference between the all-sky forcing and clear-sky forcing.

4.2.2 Description of the model experiments

A series of experiments was conducted to investigate the impacts of different seawater DMS climatologies and different gas transfer formulations on atmospheric burden of DMS, SO_2, sulfate aerosol burden and radiative forcing (Table 4.2). The control simulation was carried out using the L10 DMS concentration field with the N00 wind parameterization scheme and considering air resistance (L10 & N00 & γ_a). The model experiments can be classified relative to the control in three different ways: (1) different

flux parameterizations, (2) different DMS concentration fields or (3) different DMS concentration pattern but scaled to yield the same global mean flux as the control. In the subsequent evaluation of the model experiments, results are always compared against the control run. All DMS concentration field were prepared offline before implementation in the model. This study used only the AGCM CanAM4.1 and not the coupled CanESM, so that the algorithm-derived DMS field considered (AN01) was obtained using observed chlorophyll, light, and nutrient fields (as outlined in Section 2.2.2.1). Observed rather than simulated fields were used to avoid uncertainty from model bias. Differences among the model runs are due to either changing the DMS concentration (spatial pattern or total amount) or the air-sea gas transfer formulation. Other aspects of the model, such as oxidation pathways and cloud microphysics, are the same for all model experiments.

Table 4.2: List of model sensitivity experiments.

Name	Description
L10 & N00 & γ_a	Control experiment
L10 & N00	No air resistance
L10 & LM86	LM86 flux scheme, no air resistance
K99 & LM86	Older K99 climatology instead of L10 climatology, LM86 flux scheme, no air resistance
K99 & N00 & γ_a	As control, but with K99 climatology
K00 & N00 & γ_a	As control, but with K00 climatology
K99* & N00 & γ_a	As control, but with K99 scaled to L10 global flux
AN01* & N00 & γ_a	As control, but with AN01 scaled to L10 global flux
Temporally invariant	L10 annual mean field for all months scaled to the original L10 global flux
Spatially uniform	Spatially uniform fields with monthly global mean of L10 as concentration and scaled to the original L10 global flux
No ocean DMS	No DMS emissions from ocean

For each model configuration (as listed in Table 4.2), an ensemble of three 5-year long runs were produced. Each ensemble member uses the exact same model configuration but a different seed was used in the random number generator used in the radiation code. The three model runs for each configuration were produced to assess the internal variability of the model. The ensemble-mean result will be a statistically more robust estimate of the climate influence of DMS than the result of any individual member of the ensemble. In fact, the results of the 3-member ensemble mean is likely more robust than from a single 15-year long simulation, given that

the ensemble members are statistically independent of each other, so that there is no autocorrelation from one 5 year period to the next. The spread among realizations will indicate how large the response to changes in DMS fluxes is relative to internal variability. All experiments are run with present-day climate, for the period from January 2003 to December 2008. The first year was a spin-up period, so that the time period of the analyzed data is January 2004 to December 2008. The model output fields considered in this study are listed in Table 4.3.

Table 4.3: List of model output fields used in this study.

Variable name	Description	Units
DMS and other sulfur species		
EDSO	DMS emissions over ocean	kg m^{-2} s^{-1}
EDSL	DMS emissions over land	kg m^{-2} s^{-1}
DOXD	Oxidation rate for reaction of DMS with OH during daytime	kg m^{-2} s^{-1}
NOXD	Oxidation rate for reaction of DMS with NO_3 during nighttime	kg m^{-2} s^{-1}
VI11	Atmospheric burden of DMS	kg m^{-2}
VI12	Atmospheric burden of SO_2	kg m^{-2}
VI13	Atmospheric burden of SO_4^{2-}	kg m^{-2}
Radiative flux		
BALT	Net radiation at TOA	W m^{-2}
FSR	Reflected solar flux at TOA	W m^{-2}
FSRC	Clear-sky reflected solar flux at TOA	W m^{-2}
CFST	Solar cloud forcing at TOA	W m^{-2}

4.2.3 Scaling DMS concentration fields to L10 flux

In order to evaluate the importance of spatial and temporal structure of the DMS distribution, this study included model runs with DMS concentration fields that either had no seasonality (temporally invariant) or no spatial structure (spatially uniform). For the temporally invariant field, the annual mean field of L10 was used for all the months of the year. For the spatially uniform case, the global mean annual cycle was preserved, but each monthly field was replaced with the global mean for that month. The flux associated with these annual mean or global mean concentrations is not generally equal the global mean flux associated with the spatially or temporally varying concentration. In order to ensure that the total flux remains the same when

the spatial or temporal variability is suppressed, the temporally invariant or spatially uniform DMS concentration field was changed by a constant scaling factor. This factor was determined with offline calculations using ERA reanalysis wind and SST data. The scaling factor was a single constant for the temporally invariant run (c = 0.96). For the spatial uniform case a scaling factor had to be determined for each monthly field, in order to preserve the global mean annual cycle of the L10-derived flux.

Two additional model runs were conducted with spatial and temporal patterns given by climatologies other than L10 (K99 and AN01), but scaled to have the same global mean flux as L10 (Table 4.2). In order to remove the effect of the change in global total flux of DMS on model results, K99 and AN01 were scaled by a single factor, so that they will produce about the same global flux as in the control (L10).

4.3 Results

4.3.1 Comparison between model and reanalysis flux estimates

Before analyzing the model results, the simulated DMS flux from the model was compared to the DMS flux calculated with the ERA-Interim reanalysis SST, sea ice, and wind speed fields. The calculations with the ERA-Interim product were redone for the same time period as the model simulations (January 2004 to December 2008). The global- and annual-mean flux is generally higher in the CanAM4.1 simulation than when derived offline with the reanalysis fields (Table 4.4). The global mean flux is 20-22% larger in the model when N00 is used (with or without air resistance) and 12% larger when LM86 is used. These differences must primarily result from the winds, because SST and sea ice cover are specified in all simulations with the AMIP boundary conditions, which should be very similar to the ERA-Interim fields. The winds are overall somewhat stronger in the model than in the reanalysis fields. The probability distribution and seasonality of the winds are also slightly different between the model and the reanalysis product. A preliminary comparison between model and ERA-Interim wind velocity fields shows that the annual mean surface level wind velocity is 17% higher on average in CanAM4.1 (control run). Fluxes are particularly sensitive to high winds, and slight changes in the wind distribution can be magnified in the DMS flux.

Despite the differences in flux estimates between model and offline calculations, the sensitivity of DMS flux to changes in DMS climatology and gas transfer formulation

Table 4.4: Ocean emissions of DMS from CanAM4.1 and offline calculations with reanalysis fields. DMS flux is derived for the time period of the model simulations (January 2004 to December 2008).

Model runs	CanAM4.1			ERA-Interim		
	Global mean μmol m^{-2} s^{-1}	SD (spatial) μmol m^{-2} s^{-1}	Total flux TgS y^{-1}	Global mean μmol m^{-2} s^{-1}	SD (spatial) μmol m^{-2} s^{-1}	Total flux TgS y^{-1}
L10 & N00 & γ_a	7.02	4.56	28.9	5.72	3.65	23.6
L10 & N00	7.60	4.88	31.3	6.13	3.87	25.3
L10 & LM86	4.94	3.27	20.4	4.34	2.80	17.9
K99 & LM86	4.44	2.84	18.3	3.89	2.38	16.0
K99 & N00 & γ_a	6.31	3.97	25.9	5.11	3.08	21.0
K00 & N00 & γ_a	6.02	3.55	24.7	4.90	2.81	20.3

are similar (Table 4.5). This similarity in relative sensitivity is important since the offline calculations using reanalysis fields are used to determine the scaling factors described in the previous section. The magnitude of change is slightly higher in the model, because of the greater total flux. Given the similar sensitivities, the use of reanalysis-derived scaling factors in the GCM runs is a reasonable approximation.

Table 4.5: Difference in total ocean DMS efflux (in TgS y^{-1}) relative to control (L10 & N00 & γ_a) for both CanAM4.1 and offline calculations with reanalysis data. The corresponding percentage change is given in brackets. DMS flux is derived for the time period of the model simulations (January 2004 to December 2008).

Model runs	CanAM4.1	ERA-Interim
L10 & N00	+2.4 (8%)	+1.7 (7%)
L10 & LM86	-8.5 (30%)	-5.7 (24%)
K99 & LM86	-10.7 (37%)	-7.7 (32%)
K99 & N00 & γ_a	-3.0 (10%)	-2.7 (11%)
K00 & N00 & γ_a	-4.2 (14%)	-3.4 (14%)

4.3.2 Fluxes and atmospheric sulfur burdens

Table 4.6 presents the simulated sulfur sources, sinks, and atmospheric burdens. The simulated sulfur budget is in equilibrium: the total oxidation (by OH and NO_3) matches the total emission of DMS for all model runs. Consistent with the results in Chapter 3, the DMS flux calculated with the L10 DMS concentration field is higher than that calculated with K99 or K00, independent of which gas transfer formulation is used. Between L10 to K99, the reduction in DMS emission results in a reduction in oxidation by OH, while nighttime oxidation by NO_3 does not change much. So the change in spatial pattern between K99 to L10 mostly affects daytime oxidation rate. However, in the case of K00 and L10, both daytime and nighttime oxidation is affected equally. The responses of oxidation rates to changes in DMS concentration patterns are likely a function of the distribution of the oxidants OH and NO_3, which are specified in CanAM4.1. Table 4.6 also confirms that the scaling of DMS fields to

control flux works well. All modified concentration fields yield the same global total flux as the control.

There is an approximately linear response in atmospheric sulfur burdens to changes in DMS flux (Table 4.6). The largest changes occur in the DMS burden, with the greatest difference of ∼0.1 TgS (61%) between L10 & N00 and K99 & LM86, which almost corresponds to a 1:1 response with the change in DMS flux (68%) between these two end points. The burdens of SO_2 and sulfate are less sensitive, because of the large background value for SO_2 and sulfate from other sources (anthropogenic and volcanic). The only case where global atmospheric budgets of SO_2 and sulfate show a substantial change is when ocean DMS is turned off as an extreme scenario. In that case the SO_2 and sulfate burdens are slightly more than half that in the control run.

Figure 4.2 shows clear linear relationships between DMS, SO_2, and SO_4^{2-} burden and DMS flux. One can see in this figure a natural partition of the runs depending on what DMS field is used. Two separate regression lines were computed for runs with L10 (blue) and with K99 (purple). These two sets of regression lines are almost parallel, indicating an approximately constant offset in burden between the K99 and L10 simulations. Consistent with the flux results in Chapter 3, Figure 4.2 shows that spatial and temporal structure of DMS does not have a strong influence on total atmospheric sulfur burden. The structure in the DMS distribution does affect the oxidation pathway slightly in the step from SO_2 to sulfate, where the linear relationships differ slightly more than in other cases.

4.3.3 Relationship between radiative forcing, sulfate and DMS

In general, the response of radiative forcing follows the variation in the global mean flux of DMS linearly (Figure 4.3). However, there are some deviations from that linear relationship that can be attributed to differences in spatial and temporal pattern among the DMS fields. The relationship between the radiation fields and DMS flux can be roughly divided in two cases: L10 (blue) and K99 (purple). The response of the radiative forcing to differences in flux (e.g., from different wind parameterizations), is smaller for K99 fields than for L10.

Figure 4.3 shows that there is considerable spread in top of the atmosphere (TOA) radiative forcing depending on the strength of the ocean DMS source. Across all experiments considered the range in ensemble-mean response is 0.67 W m^{-2}. In the extreme end-member case of removing ocean DMS emission completely, a radiative

Table 4.6: Annual DMS emissions, oxidation rates and atmospheric burdens of DMS, SO_2 and SO_4^{2-}.

Model runs	Fluxes and oxidation rates (TgS y^{-1})			Atmospheric burdens (TgS)		
	Emissions†	Oxidation by OH	Oxidation by NO_3	DMS	SO_2	SO_4^{2-}
L10 & N00 & γ_a	29.8	18.1	11.7	0.24	0.40	0.67
L10 & N00	32.2	19.6	12.6	0.26	0.42	0.69
L10 & LM86	21.2	12.9	8.31	0.17	0.35	0.59
K99 & LM86	19.1	11.2	7.98	0.16	0.34	0.55
K99 & N00 & γ_a	26.8	15.6	11.2	0.22	0.38	0.62
K00 & N00 & γ_a	25.6	15.8	9.86	0.22	0.38	0.61
K99* & N00 & γ_a	29.9	17.4	12.5	0.25	0.40	0.65
AN01* & N00 & γ_a	29.9	16.6	13.3	0.25	0.40	0.64
Temporally invariant	29.7	16.2	13.6	0.24	0.41	0.65
Spatially uniform	29.9	16.3	13.6	0.25	0.41	0.64
No ocean DMS	0.87	0.52	0.35	0.00	0.25	0.38

† Includes terrestrial emissions

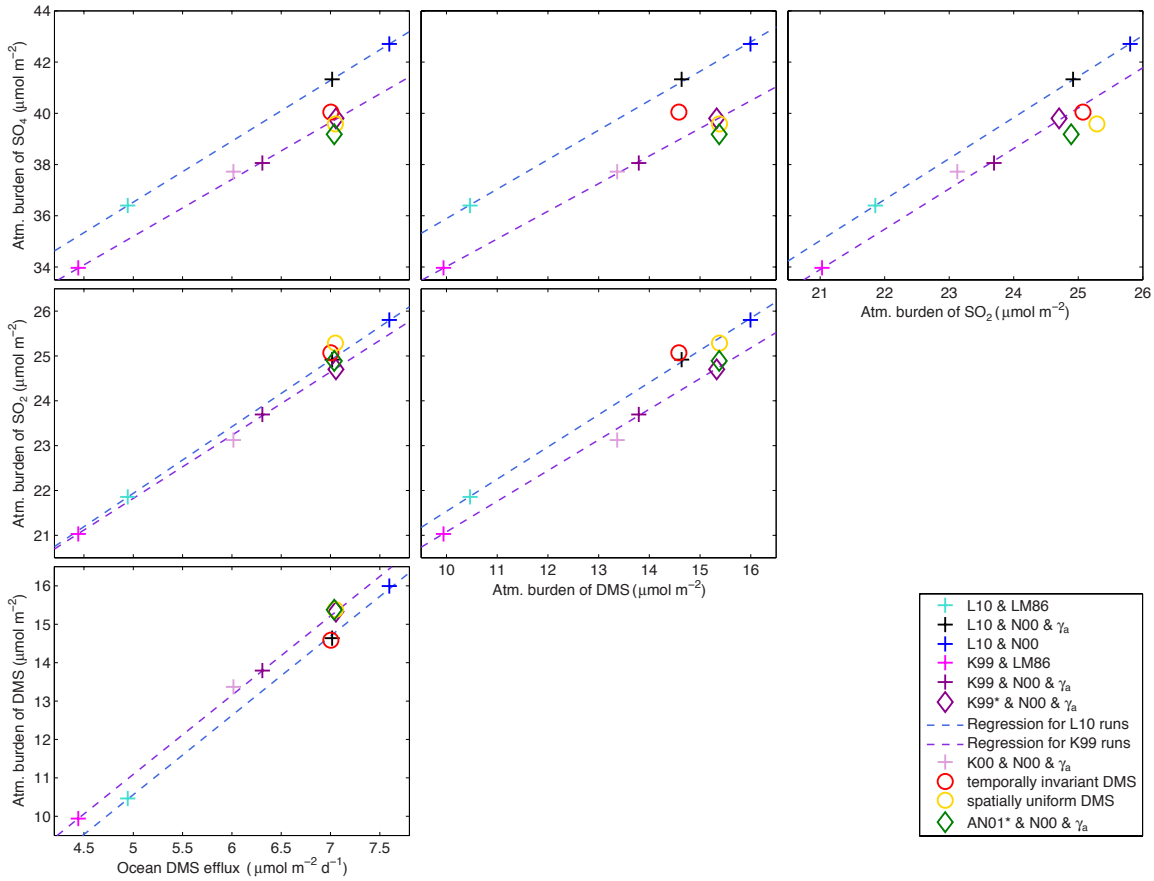

Figure 4.2: Scatterplots of atmospheric burdens of sulfur species vs. other species and ocean DMS emissions. Each data point represents the ensemble mean of a model experiment and shows the global annual mean value. The experiment names are listed in the legend and are described in Table 4.2. Crosses represent regular runs with unmodified DMS fields, and are the only data points used for the corresponding regression lines. The first column shows atmospheric burdens of sulfur species (SO_4^{2-}, SO_2, DMS) against ocean emission of DMS, the second column shows atmospheric burdens of SO_4^{2-} and SO_2 against DMS burden and the third column shows atmospheric burden of SO_4^{2-} plotted against the SO_2 burden.

forcing of +2.27 W m^{-2} resulted (not shown). Thus, the range for the given selection of DMS fields and flux parameterizations (0.67 W m^{-2}) is almost 30% of the total radiative forcing by ocean DMS in the model. Using LM86 or N00 causes a greater response in flux and thus in radiative forcing than varying the DMS field. The DMS concentration fields considered in this analysis form a relatively similar subset compared to the range discussed in Chapter 3. Use of some of these very different concentration fields could result in substantially different radiative forcings.

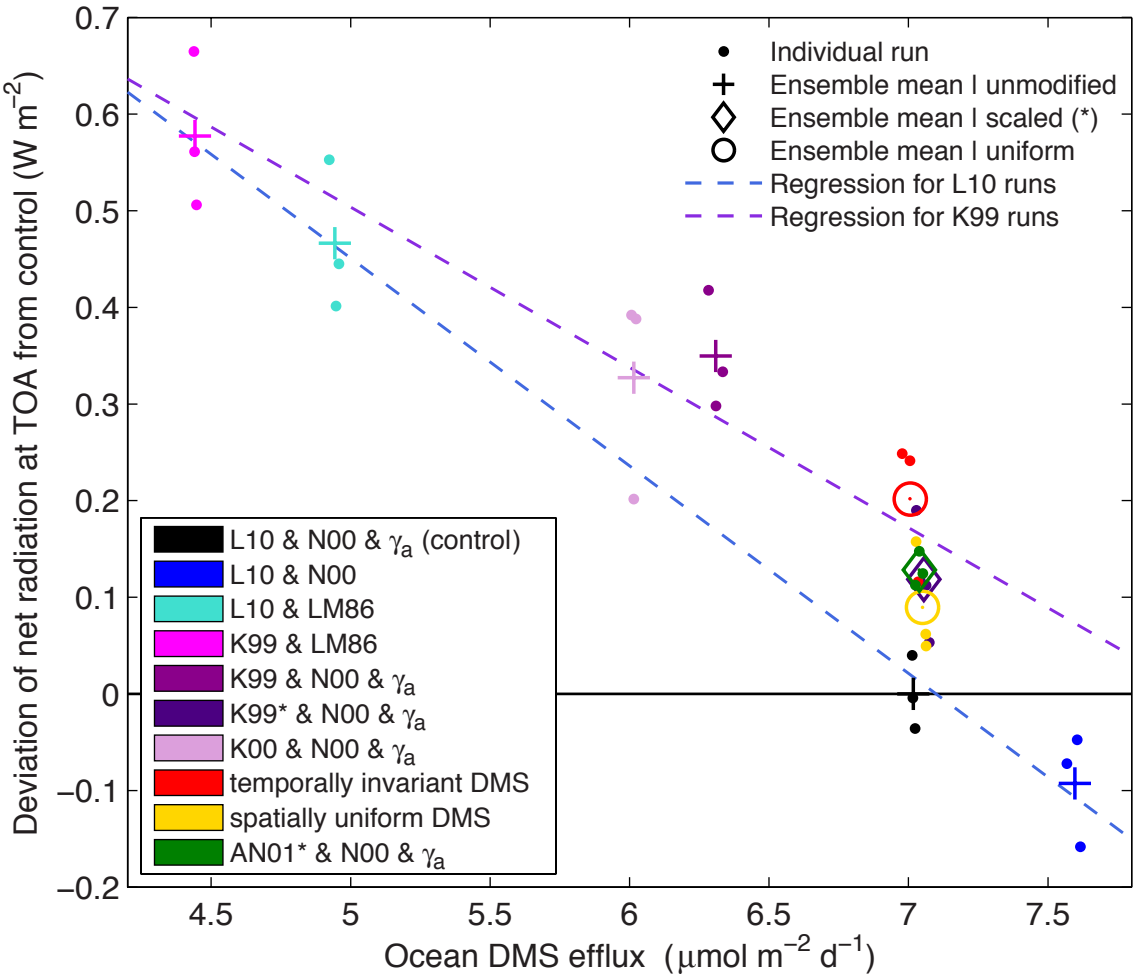

Figure 4.3: Radiative forcing difference (change in global annual mean net radiation at the top of the atmosphere (TOA)) between model experiments and control experiment relative to the global annual mean flux of ocean DMS. The experiment names are listed in the legend and are described in Table 4.2. Crosses represent the ensemble mean of regular runs with unscaled DMS fields; individual runs for each experiment are shown as dots of the same colour. Open circles denote ensemble mean of model experiments with seasonality (red) or spatial pattern (yellow) removed. Open diamonds denote model runs with DMS fields different from L10 but scaled to give the same global mean flux as L10. Only data from individual runs with unmodified K99 (purple) or L10 (blue) DMS emissions are used for the corresponding regression lines.

The spread of the individual ensemble members (Figure 4.3) indicates the range of variability in radiative forcing that one can expect simply from model internal variability (i.e. variability among ensemble members). These uncertainties arise from the fact that the model generates its own variability independent of the boundary conditions. It is worth noting that this spread is on average 0.12 W m^{-2} (ranging

from 0.04 to 0.19 W m^{-2}), which is non-trivial compared to the range of the ensemble means (0.67 W m^{-2}).

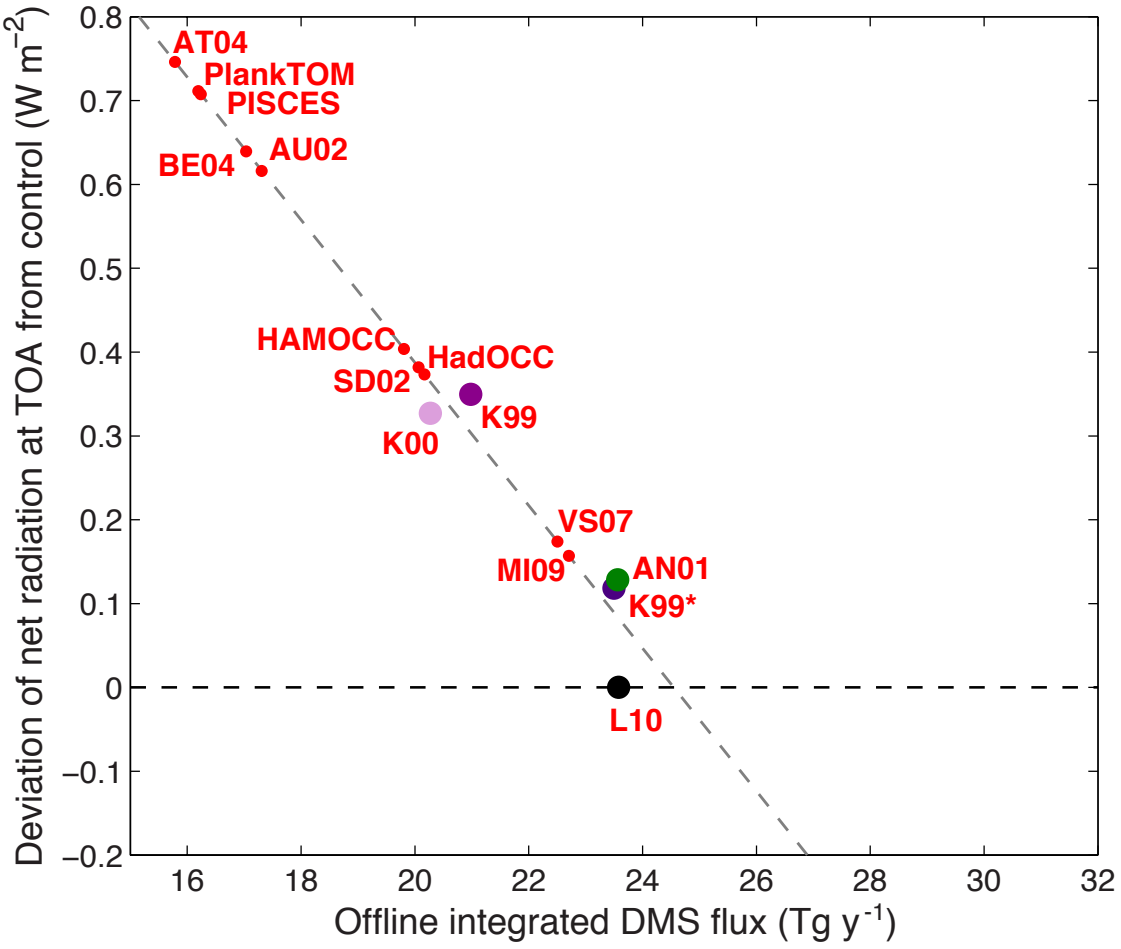

Figure 4.4: Difference in global annual mean net radiation at the top of the atmosphere (TOA) between model experiments and control plotted against the global ocean efflux of DMS. Deviations in net radiation at TOA from the control are plotted against the global total flux derived from the ERA-Interim reanalysis product (as described in Chapter 3) for model runs using N00 & γ_a as the air-sea transfer scheme (large filled circles). A linear regression for these runs only (grey dashed line) is used to derive estimates for other experiments (small red dots on regression line).

In order to obtain a rough estimate of the possible range in radiative forcing corresponding to the entire range of DMS climatologies, a linear regression model was constructed from the subset of model runs using N00 & γ_a as the flux scheme (Figure 4.4). As DMS fluxes from CanAM4.1 are not available for all DMS climatologies, offline reanalysis-based DMS fluxes are used to calculate a regression of radiative

forcing on DMS flux (Figure 4.4). Estimates of radiative forcing from the different DMS climatologies yields a range of 0.75 W m^{-2} with L10 representing the lower end since it has the greatest flux. This spread in net radiation is comparable to the total spread of model runs of 0.67 W m^{-2} (excluding the no ocean DMS flux case).

A similar estimate can be made for variation among the available piston velocity schemes. In this case, the linear regression is constructed only with model runs that have the same DMS field, but different flux parameterizations (not shown). Taking L10 as the DMS field and only considering the variation in flux estimates from changing the piston velocity schemes (LM86 to W92) gives a range of 1.04 W m^{-2} in radiative forcing. However, this estimate can be considered an upper limit, since the choice of W92 as the flux parameterization likely leads to an overestimate of the DMS flux and the choice of LM86 likely an underestimate. Nonetheless, this analysis puts the model results in perspective relative to the overall range of flux estimates (Chapter 3).

Figure 4.3 shows that the response of global mean radiative forcing to variation in the global mean flux is linear to first order. The relationship between radiative forcing and atmospheric sulfate burden shows near linearity, irrespective of differences in the spatial/temporal pattern of the DMS concentration field (Figure 4.5). In this scatterplot, there is no evidence of distinct relationships depending on use of the L10 or K99 climatologies. Thus, the deviation from linearity seems to be mainly due to changes in the oxidation pathway that occur because the spatial and temporal pattern affects the way in which DMS is transformed into sulfate (Figure 4.2).

Figure 4.6 shows global means of individual radiation fields (cloud forcing, clear-sky reflected and total reflected flux at TOA) plotted against global mean DMS flux and global mean sulfate burden. The top and middle panels differentiate the total reflected radiation into cloud forcing (i.e. reflected radiation due to clouds) and clear-sky reflection, i.e., the indirect and direct aerosol radiative effects. As with total radiative forcing, the two groups corresponding to the two DMS climatologies are evident in the scatterplots of cloud forcing and clear-sky reflection. These two populations are not evident in the scatterplots with the atmospheric sulfate burden, indicating a direct relationship between burden and radiative forcing (Figure 4.6).

An interesting difference is evident between scaled fields with spatial and temporal structure, such as K99* and AN01*, and the spatially uniform and temporally invariant DMS field. There is no change in cloud forcing (relative to the baseline simulation) for the spatially uniform and temporally invariant cases despite reductions in the global mean sulfate burden (Figure 4.6). This is also seen to some extent in AN01*. On the

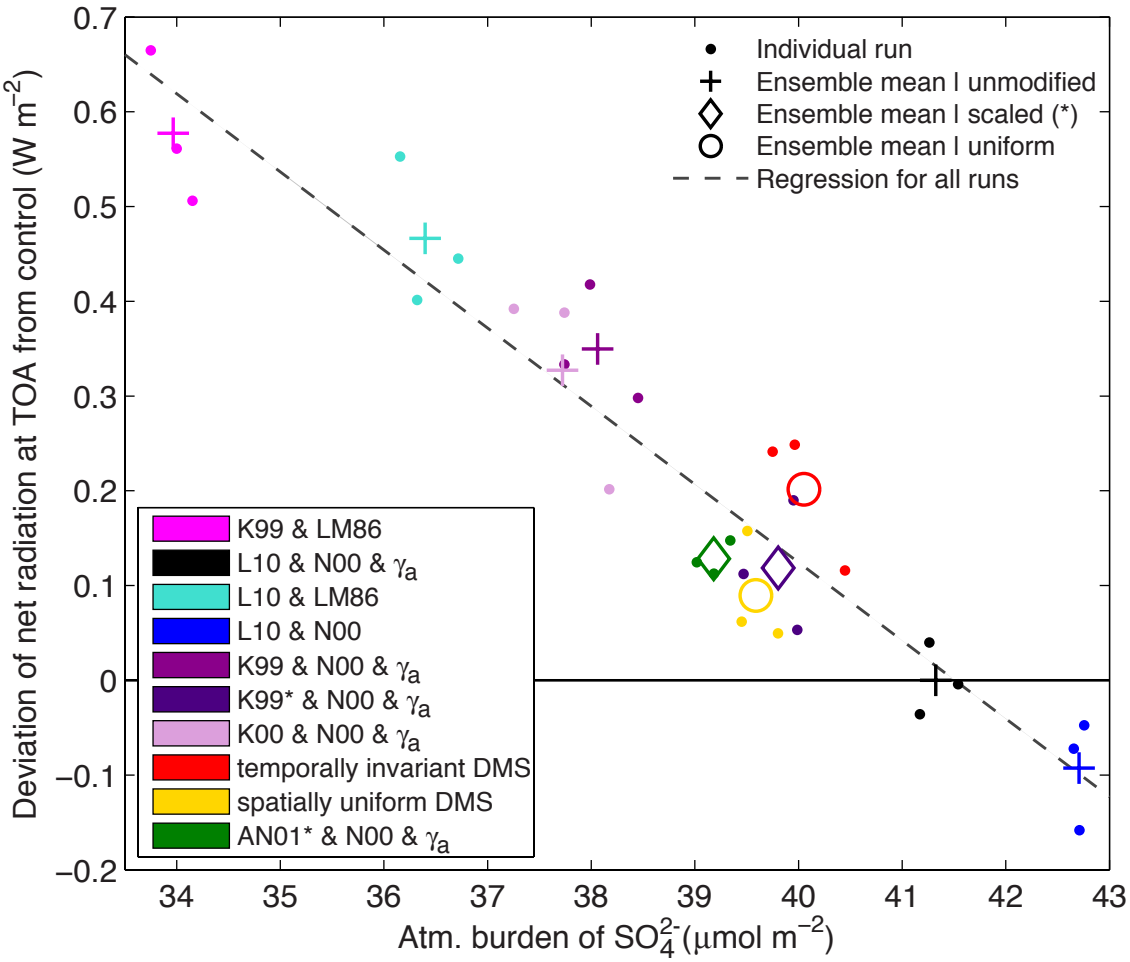

Figure 4.5: Deviation in global annual mean net radiation at TOA from control plotted against the global annual mean atmospheric burden of SO_4^{2-}. The experiment names are listed in the legend and are described in Table 4.2. Crosses represent the ensemble mean of regular runs with unmodified DMS fields. The three individual runs for each experiment are shown as dots of the same colour. Open circles denote ensemble mean of model experiments with seasonality (red) or spatial pattern (yellow) removed. Open diamonds denote model runs with DMS fields different from L10 but scaled to give the same global mean flux as L10. All data points are used for the linear regression (grey dashed line).

other hand the model run with K99*, which represents changing the DMS pattern from L10 to K99 while preserving the same global mean flux, shows a reduction in cloud forcing that scales linearly with the reduction in sulfate. The differences among the scaled fields in the cloud forcing is compensated to some extent in the clear sky reflected flux (Figure 4.6). In this case the temporally invariant case shows a greater reduction than expected by a linear dependence on sulfate burden. Experiments with

AN01* and the spatially uniform case conform more closely to the linear trend. The all-sky forcing (i.e., deviation of reflected solar flux at TOA), which is the cumulative forcing of cloud and clear-sky reflection, shows a very similar response to global mean DMS flux and atmospheric sulfate burden (Figure 4.6) as the total radiative forcing (Figures 4.3 and 4.5). The range in all-sky forcing is as large as in total forcing among the model experiments. The total radiative forcing includes variation in longwave radiation, whereas the reflected solar flux accounts only for shortwave radiation. The bottom two panels in Figure 4.6 suggest that radiative forcing is primarily in the shortwave flux and there are only slight variations in the longwave (e.g., compare to Figures 4.3 and 4.5).

4.3.4 The effect of spatial and temporal structure on aerosol and radiative forcing

Suppressing the spatial or temporal variability of ocean DMS concentration changes the radiative fluxes (Figures 4.3 and 4.6). Figure 4.7 shows the changes in global mean flux, oxidation rate, sulfur burdens, and radiation between the control run and model runs with seasonally invariant (red) and spatially uniform (yellow) DMS fields. The two cases are compared with the changes from a model run that used the N00 scheme without the air resistance term (blue). This permits a comparison of model response to changes in DMS distribution with changes in the overall strength of the DMS source. The main effect of removing the air resistance terms is an overall increase in DMS flux but no change in pattern.

The global mean burden of a species in the atmosphere over a given time period is determined by the efficiency of internal sources and sinks (e.g. chemical production rates or emissions) and indirectly by the transport. The mean state can be assumed to be at equilibrium (Table 4.6), so the budgets are a simple sum over all internal sources and sinks, i.e., changes in fluxes should be very nearly balanced by changes in the oxidation rates. This is the case in the model results as shown in Figure 4.7. For spatially or seasonally invariant DMS concentrations, the global mean DMS flux is nearly the same as in the control. There are substantial changes in the sink strengths: daytime oxidation of DMS with OH is decreased and compensated by an increase in nighttime oxidation with NO_3. The model run without air resistance shows an increase in global mean DMS flux compared to the control of about 0.40 μmol m^{-2} d^{-1}, which is balanced by an increase in oxidation rates.

In terms of the atmospheric sulfur burden, there is an obvious response in the model run without air resistance, with an overall increase in the burdens of DMS, SO_2 and SO_4^{2-}. Of the averaged fields, only the spatially-uniform DMS case seems to cause a change in the spatio-temporal oxidation pattern that substantially affects the DMS burden. All of the changes in the atmospheric sulfur burden for the spatially-uniform DMS are well outside of the range of variability (indicated by the error bars). For temporally invariant DMS, this is only true for the atmospheric burden of sulfate. The sulfate burden for spatially uniform and temporally invariant DMS runs shows a reduction comparable to the increase due to the omission of the air resistance term. Resolving the spatial-temporal pattern of DMS affects sulfate to the same extent as neglecting air resistance, which is not routinely considered in air-sea gas transfer models of DMS.

Figure 4.7 demonstrates that the spatial and temporal pattern of DMS concentration affects the aerosol direct radiative forcing, mainly by influencing the efficiency of oxidation of DMS to SO_2 and SO_4^{2-}. There is a much stronger response in the clear-sky reflected flux than in the cloud forcing. The change in total reflected solar flux is outside of the ensemble range only for the temporally-invariant and no-air-resistance case. The dramatic modification in the spatial and temporal distribution associated with seasonally-invariant or spatially-uniform DMS concentration, has very little effect on the indirect forcing (i.e., cloud forcing), but a stronger effect on direct aerosol radiative effects. However, in the spatially uniform case the response does not exceed the internal variability (error bars). Interestingly, the response in the reflected solar radiation is greater for the seasonally invariant case even though the reduction in sulfate burden of the ensemble mean is somewhat smaller compared to the spatially uniform case. In the case of the temporally invariant DMS, the reduction in the reflected solar irradiance is interpreted as being due to the temporal correlation between DMS flux and irradiance over the seasonal cycle, in addition to the reduction of atmospheric sulfate burden.

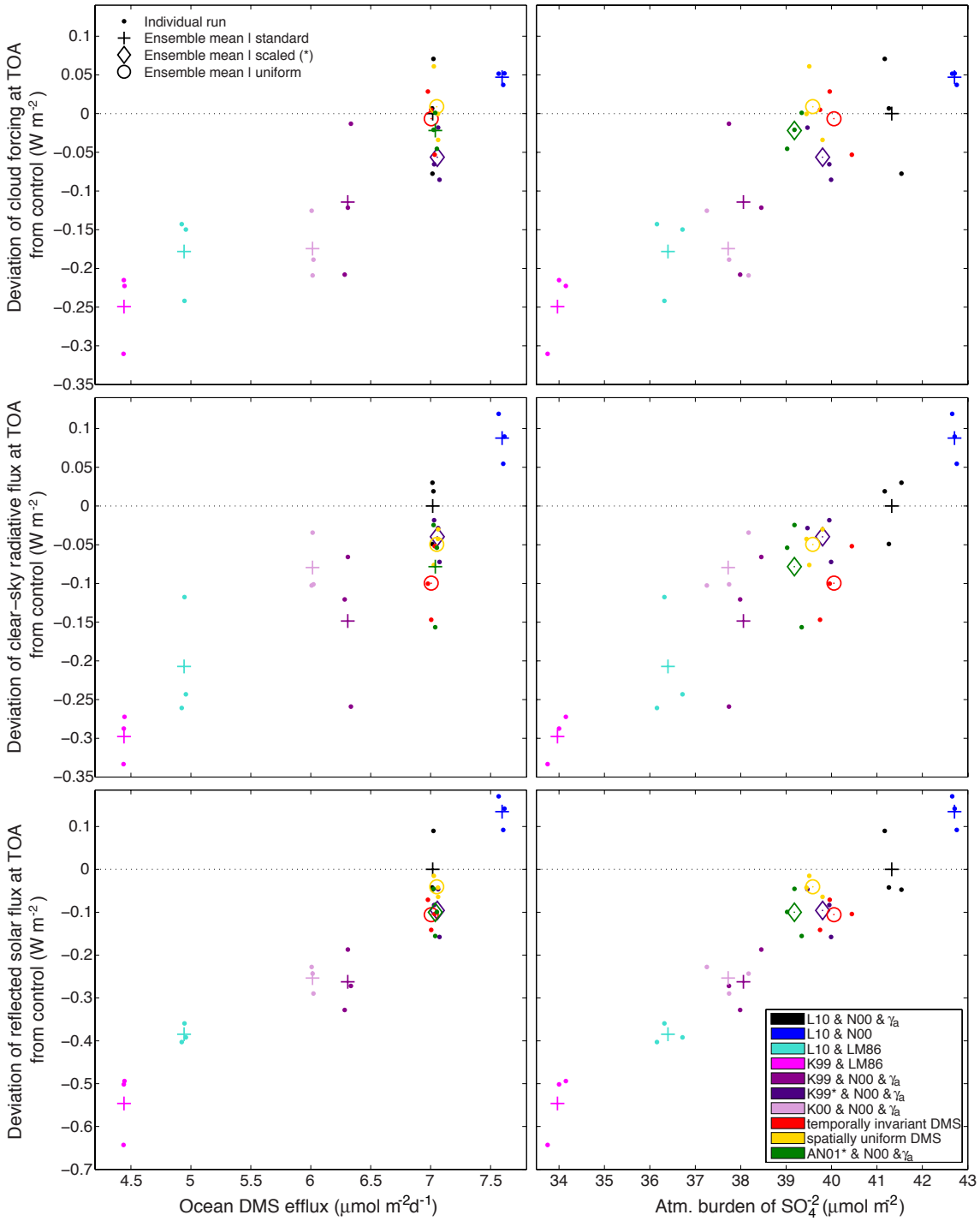

Figure 4.6: Deviation in global means of cloud forcing (upper panels), clear-sky reflected (middle panels), and total reflected irradiance (lower panels) at TOA from control plotted against global annual mean ocean DMS flux (left) and global annual mean atmospheric burden of SO_4^{2-} (right). Symbols are the same as in Figure 4.3 and 4.5. Experiment names are listed in the legend and are described in Table 4.2.

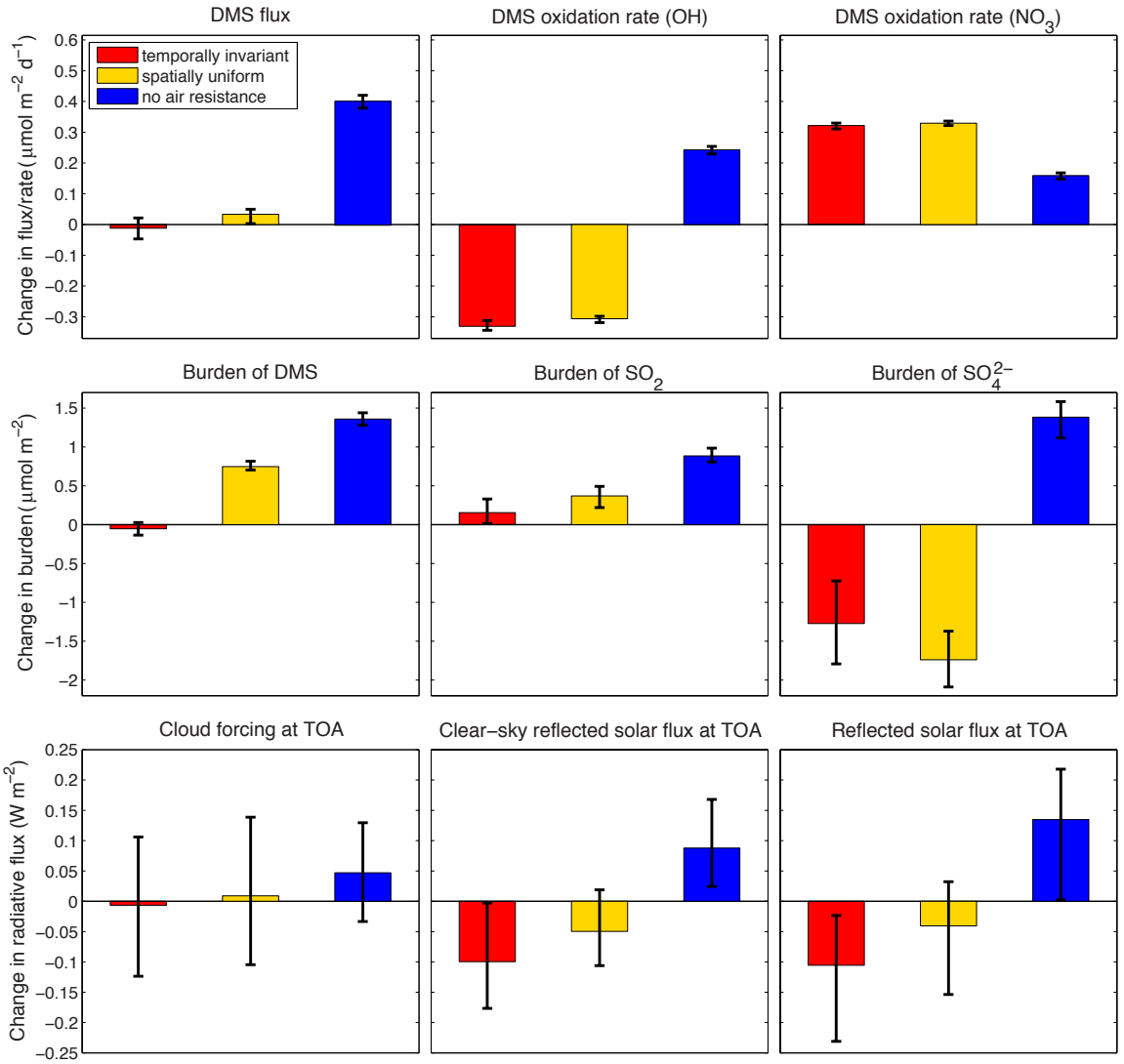

Figure 4.7: Absolute differences in global mean flux, oxidation rates, sulfur burdens, and radiation between the control run and model runs with seasonally invariant (red) or spatially uniform (yellow) DMS concentration, and the L10 & N00 model experiment (blue). Fluxes and oxidation rate of DMS are shown in the upper panels. The global mean DMS flux includes terrestrial sources to ensure mass balance. The only sink for DMS is oxidation to SO_2, which is shown for both oxidation pathways (oxidation by OH and NO_3 radicals). Absolute changes in the atmospheric sulfur burdens of DMS, SO_2 and SO_4^{2-} are shown in the middle panels. Bottom panels show absolute changes in cloud forcing, clear-sky reflected and total reflected shortwave flux. Total reflected flux is the sum of cloud and clear-sky reflected flux.

4.4 Discussion

4.4.1 The effect of spatial pattern of the sources and sinks of DMS on atmospheric sulfur burdens

The burden of DMS is not necessarily linearly related to the magnitude of sources and sinks in the simulation. It is the efficiency of the sinks which determines the burden. A very simple model for global DMS concentrations is given through the following budget equation:

$$\frac{d}{dt}\langle DMS\rangle = \langle E\rangle - \langle O \times DMS\rangle \tag{11}$$

where the angle brackets denote global averages. E is the global mean emissions and O is the oxidation rate (per unit of DMS concentration), or "efficiency" of DMS sinks. In equilibrium, $E = O \times DMS$, and the equilibrium concentration of DMS depends on O. Figure 4.7 shows the relationship between $\langle E\rangle$ and $\langle O \times DMS\rangle$ (upper three panels).

The sink term $\langle O \times DMS\rangle$ can not be decomposed as $\langle O\rangle \times \langle DMS\rangle$, so the size of O (efficiency of DMS sinks) can not be easily determined. If O were uncorrelated with DMS concentration, spatial averaging would have no effect on the sink strength. However, it is clearly seen in Figure 4.7 that the oxidation efficiency is lower in the run without spatial structure, which produces higher atmospheric DMS concentration for the same global mean emissions. Assuming equilibrium, the above equation can be rewritten as:

$$\langle E\rangle = \langle O\rangle_{eff} \times \langle DMS\rangle, \tag{12}$$

where $\langle O\rangle_{eff}$ is the effective global oxidation rate which will depend on the spatial structure of sources and sinks and can be influenced by transport.

A reduction in the global oxidation efficiency can occur for various reasons. The most likely cause is that the transport of DMS depnds on the distribution of sources. For instance, if DMS is emitted in the tropics, some of the DMS is transported to the upper troposphere through convective processes. For many chemical species, sinks are weaker in the upper troposphere than in the lower troposphere. This study omitted analysis of the vertical distribution of the oxidation rates, so it is not possible to know if this is the mechanism responsible. However, it is expected in general that differences in DMS transport lead to differences in DMS removal efficiencies and therefore different burdens in these runs.

One of the most interesting results is that the spatial and seasonal structure does affect the sulfur burden even in the global mean. In the case of atmospheric burdens of SO_2 and sulfate, the underlying reasons for the changes are difficult to identify because of a more complex representation of sinks and sources in the model. The underlying effects are likely due to a change in the spatial pattern of sources. Sulfate has a much longer lifetime if it is transported into the upper troposphere because the main sink of sulfate is scavenging in clouds, which mainly occurs in the lower and mid troposphere. The reason that the sulfate concentrations are lower in the spatially uniform and temporally invariant DMS runs might be partly because of a shift of DMS oxidation into regions with more clouds and precipitation. This would explain the decreases in sulfate despite an unchanged or slightly increased SO_2 burden (Figure 4.7).

4.4.2 The effect of spatial and temporal pattern of DMS on radiative forcing

The results of the AGCM runs show a nearly-linear response of radiative forcing to ocean DMS flux, but scatter exists around this relationship. This variability in radiative forcing for a given global DMS flux is an important uncertainty, which is controlled by the spatial and temporal pattern of DMS. For a particular global total flux, this study presents a rough estimate of the possible range in radiative forcing of just 0.2 W m^{-2} (defined by the range in ensemble means of all model experiments with the same total flux, irrespective of the spatial and temporal structure in DMS concentration). Hence, given an approximate uncertainty of 0.2 W m^{-2}, one can estimate the radiative forcing as a function of global total DMS flux. Consequently, there are two sources of uncertainty: (1) uncertainty in total emissions and (2) uncertainty in spatial/temporal pattern. This study showed that to first order, total emissions are more important than the spatial/temporal pattern.

For higher latitudes L10 (and most other DMS fields) yields stronger seasonality in concentration compared to the temporally invariant or spatially uniform field, implying that there will be seasonality in DMS fluxes correlated with radiative fluxes in these areas, such that DMS concentrations are highest when incoming solar radiation is greatest. In the case of temporally invariant DMS concentration this seasonality is neglected and only the seasonality in wind speed and SST, which is likely less correlated with solar radiation, controls the DMS flux. Thus, the effect of

the seasonality should be to make the climate effects of DMS stronger. A positive radiative forcing perturbation is in fact what can be seen from eliminating seasonality (Figures 4.3 and 4.6). The spatially uniform field represents an extreme case, and it seems likely that any moderation in this modification of spatial pattern (e.g., using hemispheric mean separate for each hemisphere instead of the global mean) would reduce the deviation in the radiative response relative to the control run. These results suggest that resolving the correct temporal distribution of DMS is more important than resolving the spatial distribution.

Identifying the reason for radiative effects due to the change in spatial and temporal structure of the DMS source is difficult, as many processes and feedbacks in the model could affect radiative fluxes. However, this study was able to demonstrate that the change almost entirely happens in the shortwave solar flux and is mostly connected to a general decrease in the atmospheric sulfate burden. As discussed above, the effect of seasonality in DMS is one exception, and the temporal correlation between DMS flux and irradiance seems to be an important factor.

Chapter 5

Summary and conclusions

This review of currently available reconstructions and simulations of DMS distribution (Chapter 2) indicates that no approach reproduces the observed DMS concentration in the ocean particularly well. The reconstructed and simulated distributions disagree with observations and the L10 climatology in terms of variance, and generally display weak spatial and temporal correlation. When using observationally-based input fields, all parameterizations substantially underestimate the variance of the available observational data set or the L10 climatology. Most empirical schemes display low variance and weak correlations relative to either L10 or the raw observations, clustering together at the lower left of the Taylor diagrams (Figures 2.16 and 2.20). None of the global models, either empirical or prognostic, are strongly correlated with L10 ($r < 0.4$ in all cases). However, some of them, such as HAMOCC and HadOCC, approximate the variance of L10 or the raw observations. Furthermore, none of the different approaches are strongly correlated with one another. Correlation coefficients only exceed 0.60 when two models possess common key parameters, such as MLD in SD02 and VS07 (Table 2.8). So in addition to universally low skill there is substantial disagreement among the different approaches. On larger spatial scales, such as latitudinal or hemispheric means, the different approaches are in greater agreement with one another and with L10 (Figures 2.18b and 2.18c). However, these estimates are difficult to test against actual observations.

The analysis in Chapter 2 demonstrated that there are great uncertainties in ocean DMS concentration, both in the spatial and temporal distribution and the global mean. Besides uncertainty in concentration, there is large uncertainty in the air-sea flux. DMS flux distributions derived from algorithms and models also fail to reproduce L10 derived fluxes and show poor agreement with flux estimates derived

from point observations. The large uncertainty about DMS concentrations and the most appropriate flux parameterization yields a large range in possible estimates of global total DMS flux (Chapter 3).

The uncertainty in spatial and temporal distribution of DMS is quite large. However, the sensitivity of the atmospheric response to changes in spatial or temporal structure of the DMS distribution is considerably smaller than that associated with the magnitude of the global total flux (Chapter 4). This result suggests that on a global scale it is most important to have an accurate estimate of the global DMS flux, while resolving the exact spatial and temporal distribution is of less importance. Rough estimates of the range in radiative forcing given the possible range in DMS flux were estimated as 0.67 W m^{-2} (across all model simulations with ocean DMS efflux), 0.75 W m^{-2} (among available DMS fields) and 1.04 W m^{-2} (among different flux parameterizations). Contrasting these uncertainties with the well-constrained radiative forcing of $+1.82 \pm 0.19$ W m^{-2} due to the increase in atmospheric CO_2 from 1750 to 2011 (Myhre et al., 2013), emphasizes the degree of uncertainty in DMS-derived aerosol forcing and the need to better constrain this quantity.

An holistic view of the (global scale) uncertainties is important in terms of understanding the role of DMS in the climate system. Uncertainty about the global DMS concentration translates to uncertainty about global estimates of DMS flux. In the case of the ocean DMS efflux, besides uncertainty about DMS concentration, there is substantial uncertainty associated with parameterizations of gas transfer velocity. This leads to uncertainties in radiative forcing resulting from DMS-derived aerosols, which suggests that DMS may actually play a more important role in the climate system than has previously been estimated, and that changes in DMS fluxes could alter our projections of future climate in unexpected ways.

Previous studies have found a relatively weak influence of DMS fluxes on climate (e.g., Kloster et al., 2007; Vallina et al., 2007b; Woodhouse et al., 2010). However, these studies may have a "weak effect" bias because of a low bias in DMS flux (Figure 4.4), which would translate into a low bias in radiative forcing. The results of the current study show that there is a systematic bias of up to 0.75 W m^{-2} for some DMS models and algorithms. However, this full range of uncertainty might not be a meaningful estimate of the uncertainty, since some representations (e.g., L10) can be considered more skillful than others (algorithms and models).

The uncertainty in DMS concentration estimates contributes substantially to uncertainties in present-day aerosol radiative forcing (Carslaw et al., 2013), defined

as the difference in radiative fluxes between present-day and preindustrial due to anthropogenic changes in the atmospheric aerosol burden. To estimate the present-day forcing, it is necessary to have a reliable estimate of aerosol forcing in preindustrial times. While observationally-based estimates of present-day radiative fluxes can be made, these are not available for preindustrial conditions. Current understanding of the natural sulfur cycle indicates that most preindustrial forcing from sulfate aerosol was determined by DMS flux and volcanic emissions. Uncertainty in estimates of these fluxes, which must be based on models in the absence of direct observations, will impact forcing estimates. The large uncertainty in DMS flux translates into uncertainty in preindustrial aerosol forcing, regardless of whether one assumes that DMS flux remains the same as or similar to preindustrial conditions. As DMS fluxes may have changed from the preindustrial state, the use of fluxes estimated from present-day conditions increases this uncertainty.

Limitations of this study and future directions There are a number of limitations in the present study, which are outlined here along with suggestions for further research. Results in Chapter 2 demonstrated low skill of existing algorithms and models in reconstructing sea-surface concentration of DMS. However, the algorithms and models were tested on a limited dataset of available observations which contain seasonal and spatial sampling biases. In addition, DMS concentration is highly variable, so the observed mean concentrations for e.g. a $1^\circ \times 1^\circ$ grid, used to compare against reconstructed fields, may not be well constrained. This intercomparison study strived to include all available prognostic and diagnostic models, but certainly did not sample the entire spectrum of possibilities.

The intercomparison study may have shown an inherent limitation to the ability of empirical algorithms to reconstruct DMS concentrations accurately. Over the past 15 years there has not been any progressive improvement, which suggests that empirical or diagnostic approaches might not be effective in modelling DMS on a global scale. Empirically derived algorithms may be useful for modelling DMS concentrations in certain regions, but it seems that none of the present algorithms can accurately model DMS concentrations globally. This suggests that using such a parameterization for DMS (as opposed to a climatology) in a climate model is not recommended because of their substantial biases. Although the presently available prognostic models did not demonstrate noticeably better skill than the algorithms, future improvements in process modelling are possible, such that more skillful prognostic DMS models are

likely to emerge in the future. It is also important to note that the sensitivity analysis of DMS flux in this study (Chapter 3) includes only a limited number of gas transfer parameterizations, which are empirical and mainly based on wind speed. Application of these simple parameterizations ignores potentially important physical mechanisms in air-sea transfer. Implementing a more physical representation of the DMS transfer velocity into global models remains a significant challenge.

It is possible that the climate effects of DMS are not completely realistic in the AGCM because idealized assumptions about aerosol processes are made and there is no process-based representation of the indirect aerosol effect. These biases would be expected to be especially pronounced in the parts of the atmosphere least affected by anthropogenic emissions, such as the Southern Hemisphere. Future model simulations could be done with an atmosphere model that has a more physical treatment of aerosol processes and cloud microphysical properties. It is possible that sensitivity to the spatial and temporal distribution of DMS would increase with an improved representation of cloud microphysics. Furthermore, instead of using specified atmospheric concentrations of the oxidants, a more interactive tropospheric chemistry scheme could be used to achieve a more realistic modelling of atmospheric DMS oxidation.

This study did not investigate climate sensitivity to DMS flux in a coupled model; all model simulations were done in an atmosphere-only model (CanAM4.1). These experiments could be repeated in a coupled model setting, which would allow for feedbacks, which is a key concept in the CLAW hypothesis. Furthermore, a coupled model setup could evaluate prognostic DMS modules, for which DMS concentrations are calculated online, as opposed to being specified by (climatological) fields. This would make it possible to explore climate sensitivity to specific parameters or different mechanisms within the prognostic DMS module. Results of using different modules would be more compatible, since input data are generated from the same physical model irrespective of what module is used. Hence, this could give information about the inherent difference among the DMS modules versus differences in the input data associated with physical and biogeochemistry components of the ocean model. However, one should keep in mind that simulation of DMS concentration with model fields (as opposed to observation-based data) will likely introduce additional uncertainty which are potentially larger than the signal that one is trying to investigate.

Bibliography

Anderson, T., Spall, S., Yool, A., Cipollini, P., Challenor, P., and Fasham, M. (2001). Global fields of sea surface dimethylsulfide predicted from chlorophyll, nutrients and light. *Journal of Marine Systems*, 30(1-2):1–20, doi:10.1016/S0924-7963(01)00028-8.

Andreae, M. O. and Crutzen, P. (1997). Atmospheric aerosols: Biogeochemical sources and role in atmospheric chemistry. *Science*, 276(5315):1052–1058, doi:10.1126/science.276.5315.1052.

Andreae, M. O. and Raemdonck, H. (1983). Dimethyl sulfide in the surface ocean and the marine atmosphere: A global view. *Science*, 221(4612):744–747, doi:10.1126/science.221.4612.744.

Antonov, J. I., Seidov, D., Boyer, T. P., Locarnini, R. A., Mishonov, A. V., Garcia, H. E., Baranova, O. K., Zweng, M. M., and Johnson, D. R. (2010). *World Ocean Atlas 2009, Volume 2: Salinity*. In Levitus, S., editor, *NOAA Atlas NESDIS 69*, page 184. U.S. Government Printing Office, Washington, D.C.

Aranami, K. and Tsunogai, S. (2004). Seasonal and regional comparison of oceanic and atmospheric dimethylsulfide in the northern North Pacific: Dilution effects on its concentration during winter. *Journal of Geophysical Research: Atmospheres*, 109(D12), doi:10.1029/2003JD004288.

Archer, S. D., Gilbert, F. J., Nightingale, P. D., Zubkov, M. V., Taylor, A. H., Smith, G. C., and Burkill, P. H. (2002). Transformation of dimethylsulphoniopropionate to dimethyl sulphide during summer in the North Sea with an examination of key processes via a modelling approach. *Deep-Sea Research Part II: Topical Studies in Oceanography*, 49(15):3067–3101, doi:10.1016/S0967-0645(02)00072-3.

Asher, E. C., Merzouk, A., and Tortell, P. D. (2011). Fine-scale spatial and temporal variability of surface water dimethylsufide (DMS) concentrations and sea-air fluxes in the NE Subarctic Pacific. *Marine Chemistry*, 126(1-4):63–75, doi:10.1016/j.marchem.2011.03.009.

Atkinson, R., Baulch, D. L., Cox, R. A., Hampson, R. F., Kerr (Chairman), J. A., and Troe, J. (1989). Evaluated kinetic and photochemical data for atmospheric chemistry: Supplement III. IUPAC subcommittee on gas kinetic data evaluation for atmospheric chemistry. *Journal of Physical and Chemical Reference Data*, 18(2):881–1097, doi:10.1063/1.555832.

Aumont, O., Belviso, S., and Monfray, P. (2002). Dimethylsulfoniopropionate (DMSP)

and dimethylsulfide (DMS) sea surface distributions simulated from a global three-dimensional ocean carbon cycle model. *Journal of Geophysical Research: Oceans*, 107(C4), doi:10.1029/1999JC000111.

Banse, K. and English, D. C. (1999). Comparing phytoplankton seasonality in the Eastern and Western Subarctic Pacific and the Western Bering Sea. *Progress in Oceanography*, 43(2-4):235–288, doi:10.1016/S0079-6611(99)00010-5.

Bates, T., Charlson, R., and Gammon, R. (1987). Evidence for the climatic role of marine biogenic sulphur. *Nature*, 329:319–321, doi:10.1038/329319a0.

Bates, T., Lamb, B., Guenther, A., Dignon, J., and Stoiber, R. (1992). Sulfur emissions to the atmosphere from natural sources. *Journal of Atmospheric Chemistry*, 14:315–337, doi:10.1007/BF00115242.

Bates, T. S., Kiene, R. P., Wolfe, G. V., Matrai, P. A., Chavez, F. P., Buck, K. R., Blomquist, B. W., and Cuhel, R. L. (1994). The cycling of sulfur in surface seawater of the Northeast Pacific. *Journal of Geophysical Research: Oceans*, 99(C4), doi:10.1029/93JC02782.

Bell, T. G., Malin, G., McKee, C. M., and Liss, P. S. (2006). A comparison of dimethylsulphide (DMS) data from the Atlantic Meridional Transect (AMT) programme with proposed algorithms for global surface DMS concentrations. *Deep-Sea Research Part II: Topical Studies in Oceanography*, 53(14-16):1720–1735, doi:10.1016/j.dsr2.2006.05.013.

Belviso, S., Bopp, L., Moulin, C., Orr, J., Anderson, T., Aumont, O., Chu, S., Elliott, S., Maltrud, M., and Simó, R. (2004a). Comparison of global climatological maps of sea surface dimethyl sulfide. *Global Biogeochemical Cycles*, 18(3), doi:10.1029/2003GB002193.

Belviso, S. and Caniaux, G. (2009). A new assessment in North Atlantic waters of the relationship between DMS concentration and the upper mixed layer solar radiation dose. *Global Biogeochemical Cycles*, 23(1), doi:10.1029/2008GB003382.

Belviso, S., Claustre, H., and Marty, J.-C. (2001). Evaluation of the utility of chemotaxonomic pigments as a surrogate for particulate DMSP. *Limnology and Oceanography*, 46(4):989–995, doi:10.4319/lo.2001.46.4.0989.

Belviso, S., Masotti, I., Tagliabue, A., Bopp, L., Brockmann, P., Fichot, C., Caniaux, G., Prieur, L., Ras, J., Uitz, J., Loisel, H., Dessailly, D., Alvain, S., Kasamatsu, N., and Fukuchi, M. (2012). DMS dynamics in the most oligotrophic subtropical zones of the global ocean. *Biogeochemistry*, 110(1-3):215–241, doi:10.1007/s10533-011-9648-1.

Belviso, S., Morrow, R., and Mihalopoulos, N. (2000). An Atlantic meridional transect of surface water dimethyl sulfide concentrations with 10–15 km horizontal resolution and close examination of ocean circulation. *Journal of Geophysical Research: Atmospheres*, 105(D11), doi:10.1029/1999JD900955.

Belviso, S., Moulin, C., Bopp, L., and Stefels, J. (2004b). Assessment of a global climatology of oceanic dimethylsulfide (DMS) concentrations based on SeaWiFS

imagery (1998-2001). *Canadian Journal of Fisheries and Aquatic Sciences*, 61(5):804–816, doi:10.1139/f04-001.

Berge, E. (1993). Coupling of wet scavenging of sulphur to clouds in a numerical weather prediction model. *Tellus Series B: Chemical And Physical Meteorology*, 45(1):1–22, doi:10.1034/j.1600-0889.1993.00001.x.

Bishop, J. K. B., Rossow, W. B., and Dutton, E. G. (1997). Surface solar irradiance from the International Satellite Cloud Climatology Project 1983–1991. *Journal of Geophysical Research: Atmospheres*, 102(D6), doi:10.1029/96JD03865.

Blomquist, B. W., Fairall, C. W., Huebert, B. J., Kieber, D. J., and Westby, G. R. (2006). DMS sea-air transfer velocity: Direct measurements by eddy covariance and parameterization based on the NOAA/COARE gas transfer model. *Geophysical Research Letters*, 33(7), doi:10.1029/2006GL025735.

Bopp, L., Aumont, O., Belviso, S., and Monfray, P. (2003). Potential impact of climate change on marine dimethyl sulfide emissions. *Tellus Series B: Chemical And Physical Meteorology*, 55(1):11–22, doi:10.1034/j.1600-0889.2003.042.x.

Bopp, L., Boucher, O., Aumont, O., Belviso, S., Dufresne, J., Pham, M., and Monfray, P. (2004). Will marine dimethylsulfide emissions amplify or alleviate global warming? A model study. *Canadian Journal of Fisheries and Aquatic Sciences*, 61(5):826–835, doi:10.1139/F04-045.

Boucher, O., Moulin, C., Belviso, S., Aumont, O., Bopp, L., Cosme, E., von Kuhlmann, R., Lawrence, M. G., Pham, M., Reddy, M. S., Sciare, J., and Venkataraman, C. (2003). DMS atmospheric concentrations and sulphate aerosol indirect radiative forcing: a sensitivity study to the DMS source representation and oxidation. *Atmospheric Chemistry and Physics*, 3(1):49–65, doi:10.5194/acp-3-49-2003.

Brasseur, G. P., Hauglustaine, D. A., Walters, S., Rasch, P. J., Müller, J.-F., Granier, C., and Tie, X. X. (1998). MOZART, a global chemical transport model for ozone and related chemical tracers: 1. Model description. *Journal of Geophysical Research: Atmospheres*, 103(D21), doi:10.1029/98JD02397.

Brimblecombe, P. and Shooter, D. (1986). Photo-oxidation of dimethylsulphide in aqueous solution. *Marine Chemistry*, 19(4):343–353, doi:10.1016/0304-4203(86)90055-1.

Brock, T. D. (1981). Calculating solar radiation for ecological studies. *Ecological Modelling*, 14(1-2):1–19, doi:10.1016/0304-3800(81)90011-9.

Cameron-Smith, P., Elliott, S., Maltrud, M., Erickson, D., and Wingenter, O. (2011). Changes in dimethyl sulfide oceanic distribution due to climate change. *Geophysical Research Letters*, 38(7), doi:10.1029/2011GL047069.

Carslaw, K. S., Lee, L. A., Reddington, C. L., Pringle, K. J., Rap, A., Forster, P. M., Mann, G. W., Spracklen, D. V., Woodhouse, M. T., Regayre, L. A., and Pierce, J. R. (2013). Large contribution of natural aerosols to uncertainty in indirect forcing. *Nature*, 503(7474):67–71, doi:10.1038/nature12674.

Chameides, W. L. (1984). The photochemistry of a remote marine strat-

iform cloud. *Journal of Geophysical Research: Atmospheres*, 89(D3), doi:10.1029/JD089iD03p04739.

Charlson, R. J., Lovelock, J. E., Andreae, M. O., and Warren, S. G. (1987). Oceanic phytoplankton, atmospheric sulphur, cloud albedo and climate. *Nature*, 326(6114):655–661, doi:10.1038/326655a0.

Chu, S., Elliott, S., Maltrud, M., Hernandez, J., and Erickson, D. (2004). Ecodynamic and eddy-admitting dimethyl sulfide simulations in a global ocean biogeochemistry/circulation model. *Earth Interactions*, 8(11):1–25, doi:10.1175/1087-3562(2004)008<0001:EAEDSS>2.0.CO;2.

Chu, S. P., Elliott, S., and Maltrud, M. E. (2003). Global eddy permitting simulations of surface ocean nitrogen, iron, sulfur cycling. *Chemosphere*, 50(2):223–235, doi:10.1016/S0045-6535(02)00162-5.

Claustre, H. (1994). The trophic status of various oceanic provinces as revealed by phytoplankton pigment signatures. *Limnology and Oceanography*, 39(5):1206–1210, doi:10.4319/lo.1994.39.5.1206.

Collins, W. J., Bellouin, N., Doutriaux-Boucher, M., Gedney, N., Halloran, P., Hinton, T., Hughes, J., Jones, C. D., Joshi, M., Liddicoat, S., Martin, G., O'Connor, F., Rae, J., Senior, C., Sitch, S., Totterdell, I., Wiltshire, A., and Woodward, S. (2011). Development and evaluation of an Earth-system model – HadGEM2. *Geoscientific Model Development*, 4(4):1051–1075, doi:10.5194/gmd-4-1051-2011.

Croft, B., Lohmann, U., and von Salzen, K. (2005). Black carbon ageing in the Canadian Centre for Climate modelling and analysis atmospheric general circulation model. *Atmospheric Chemistry and Physics*, 5(7):1931–1949, doi:10.5194/acp-5-1931-2005.

Cropp, R. A., Norbury, J., Gabric, A. J., and Braddock, R. D. (2004). Modeling dimethylsulphide production in the upper ocean. *Global Biogeochemical Cycles*, 18(3), doi:10.1029/2003GB002126.

Curson, A. R. J., Rogers, R., Todd, J. D., Brearley, C. A., and Johnston, A. W. B. (2008). Molecular genetic analysis of a dimethylsulfoniopropionate lyase that liberates the climate-changing gas dimethylsulfide in several marine α-proteobacteria and Rhodobacter sphaeroides. *Environmental Microbiology*, 10(3):757–767, doi:10.1111/j.1462-2920.2007.01499.x.

Dacey, J. W. H., Wakeham, S. G., and Howes, B. L. (1984). Henry's law constants for dimethylsulfide in freshwater and seawater. *Geophysical Research Letters*, 11(10), doi:10.1029/GL011i010p00991.

de Boyer Montégut, C., Madec, G., Fischer, A. S., Lazar, A., and Iudicone, D. (2004). Mixed layer depth over the global ocean: An examination of profile data and a profile-based climatology. *Journal of Geophysical Research: Oceans*, 109(C12), doi:10.1029/2004JC002378.

Dee, D. P., Uppala, S. M., Simmons, A. J., Berrisford, P., Poli, P., Kobayashi, S., Andrae, U., Balmaseda, M. A., Balsamo, G., Bauer, P., Bechtold, P., Beljaars, A.

C. M., van de Berg, L., Bidlot, J., Bormann, N., Delsol, C., Dragani, R., Fuentes, M., Geer, A. J., Haimberger, L., Healy, S. B., Hersbach, H., Hólm, E. V., Isaksen, L., Kållberg, P., Köhler, M., Matricardi, M., McNally, A. P., Monge-Sanz, B. M., Morcrette, J. J., Park, B. K., Peubey, C., de Rosnay, P., Tavolato, C., Thépaut, J. N., and Vitart, F. (2011). The ERA-Interim reanalysis: configuration and performance of the data assimilation system. *Quarterly Journal of the Royal Meteorological Society*, 137(656):553–597, doi:10.1002/qj.828.

DeMore, W. B., Golden, D. M., Hampson, R. F., Howard, C. J., Kurylo, M. J., Molina, M. J., Ravishankara, A. R., and Sander, S. P. (1992). *Chemical kinetics and photochemical data for use in stratospheric modeling, evaluation number 10*. JPL Publication 92-20. Jet Propulsion Laboratory, California Institute of Technology, Pasadena, CA.

Dentener, F., Kinne, S., Bond, T., Boucher, O., Cofala, J., Generoso, S., Ginoux, P., Gong, S., Hoelzemann, J. J., Ito, A., Marelli, L., Penner, J. E., Putaud, J.-P., Textor, C., Schulz, M., van der Werf, G. R., and Wilson, J. (2006). Emissions of primary aerosol and precursor gases in the years 2000 and 1750 prescribed data-sets for AeroCom. *Atmospheric Chemistry and Physics*, 6(12):4321–4344, doi:10.5194/acp-6-4321-2006.

Dentener, F. J. and Crutzen, P. J. (1994). A three-dimensional model of the global ammonia cycle. *Journal of Atmospheric Chemistry*, 19(4):331–369, doi:10.1007/BF00694492.

Derevianko, G. J., Deutsch, C., and Hall, A. (2009). On the relationship between ocean DMS and solar radiation. *Geophysical Research Letters*, 36(17), doi:10.1029/2009GL039412.

Doney, S. C., Lindsay, K., Caldeira, K., Campin, J.-M., Drange, H., Dutay, J.-C., Follows, M., Gao, Y., Gnanadesikan, A., Gruber, N., Ishida, A., Joos, F., Madec, G., Maier-Reimer, E., Marshall, J. C., Matear, R. J., Monfray, P., Mouchet, A., Najjar, R., Orr, J. C., Plattner, G.-K., Sarmiento, J., Schlitzer, R., Slater, R., Totterdell, I. J., Weirig, M.-F., Yamanaka, Y., and Yool, A. (2004). Evaluating global ocean carbon models: The importance of realistic physics. *Global Biogeochemical Cycles*, 18(3), doi:10.1029/2003GB002150.

Dufresne, J.-L., Quaas, J., Boucher, O., Denvil, S., and Fairhead, L. (2005). Contrasts in the effects on climate of anthropogenic sulfate aerosols between the 20th and the 21st century. *Geophysical Research Letters*, 32(21), doi:10.1029/2005GL023619.

Elliott, S. (2009). Dependence of DMS global sea-air flux distribution on transfer velocity and concentration field type. *Journal of Geophysical Research: Biogeosciences*, 114(G2), doi:10.1029/2008JG000710.

Elliott, S., Chu, S., and Erickson, D. (2007). Contours of simulated marine dimethyl sulfide distributions under variation in a Gabric mechanism. *Environmental Modelling & Software*, 22(3):349–358, doi:10.1016/j.envsoft.2005.11.006.

Erickson, D. J., Ghan, S. J., and Penner, J. E. (1990). Global ocean-to-atmosphere

dimethyl sulfide flux. *Journal of Geophysical Research: Atmospheres*, 95(D6), doi:10.1029/JD095iD06p07543.

Esbensen, S. K. and Kushnir, Y. (1981). *The heat budget of the global ocean: An atlas based on estimates from surface marine observations*. Issue 29 of Climatic Research Institute Report. Oregan State University, Corvallis.

Fairall, C. W., Hare, J. E., Edson, J. B., and McGillis, W. R. (2000). Parameterization and micrometeorological measurement of air-sea gas transfer. *Boundary-Layer Meteorology*, 96(1-2):63–106, doi:10.1023/A:1002662826020.

Fairall, C. W., Yang, M., Bariteau, L., Edson, J. B., Helmig, D., McGillis, W., Pezoa, S., Hare, J. E., Huebert, B., and Blomquist, B. (2011). Implementation of the Coupled Ocean-Atmosphere Response Experiment flux algorithm with CO_2, dimethyl sulfide, and O_3. *Journal of Geophysical Research: Oceans*, 116(C4), doi:10.1029/2010JC006884.

Friedrichs, M. A. M., Dusenberry, J. A., Anderson, L. A., Armstrong, R. A., Chai, F., Christian, J. R., Doney, S. C., Dunne, J., Fujii, M., Hood, R., McGillicuddy, Jr., D. J., Moore, J. K., Schartau, M., Spitz, Y. H., and Wiggert, J. D. (2007). Assessment of skill and portability in regional marine biogeochemical models: Role of multiple planktonic groups. *Journal of Geophysical Research: Oceans*, 112(C8), doi:10.1029/2006JC003852.

Gabric, A., Ayers, G. P., Murray, C., and Parslow, J. (1996). Use of remote sensing and mathematical modelling to predict the flux of dimethylsulfide to the atmosphere in the Southern Ocean. *Advances in Space Research*, 18(7):117–128, doi:10.1016/0273-1177(95)00954-X.

Gabric, A., Ayers, G. P., and Sander, G. (1995). Independent marine and atmospheric model estimates of the sea-air flux of dimethylsulfide in the Southern Ocean. *Geophysical Research Letters*, 22(24), doi:10.1029/95GL02936.

Gabric, A., Cropp, R., Hirst, T., and Marchant, H. (2003). The sensitivity of dimethyl sulfide production to simulated climate change in the Eastern Antarctic Southern Ocean. *Tellus Series B: Chemical And Physical Meteorology*, 55(5):966–981, doi:10.1034/j.1600-0889.2003.00077.x.

Gabric, A., Matrai, P. A., and Vernet, M. (1999). Modelling the production and cycling of dimethylsulphide during the vernal bloom in the Barents Sea. *Tellus Series B: Chemical And Physical Meteorology*, 51(5):919–937, doi:10.1034/j.1600-0889.1999.t01-4-00005.x.

Gabric, A., Murray, N., Stone, L., and Kohl, M. (1993). Modelling the production of dimethylsulfide during a phytoplankton bloom. *Journal of Geophysical Research: Oceans*, 98(C12), doi:10.1029/93JC01773.

Gabric, A., Qu, B., Matrai, P., and Hirst, A. (2005). The simulated response of dimethylsulfide production in the Arctic Ocean to global warming. *Tellus Series B: Chemical And Physical Meteorology*, 57(5):391–403, doi:10.1111/j.1600-0889.2005.00163.x.

Gabric, A. J., Simó, R., Cropp, R. A., Hirst, A. C., and Dachs, J. (2004). Modeling estimates of the global emission of dimethylsulfide under enhanced greenhouse conditions. *Global Biogeochemical Cycles*, 18(3), doi:10.1029/2004GB002337.

Gabric, A. J., Whetton, P. H., Boers, R., and Ayers, G. P. (1998). The impact of simulated climate change on the air-sea flux of dimethylsulphide in the Subantarctic Southern Ocean. *Tellus Series B: Chemical And Physical Meteorology*, 50(4):388–399, doi:10.1034/j.1600-0889.1998.t01-3-00006.x.

Gabric, A. J., Whetton, P. H., and Cropp, R. (2001). Dimethylsulphide production in the Subantarctic Southern Ocean under enhanced greenhouse conditions. *Tellus Series B: Chemical And Physical Meteorology*, 53(3):273–287, doi:10.1034/j.1600-0889.2001.01244.x.

Galloway, J. N., Penner, J. E., Atherton, C. S., Prospero, J. M., Rodhe, H., Artz, R. S., Balkanski, Y. J., Bingemer, H. G., Brost, R. A., Burgermeister, S., Carmichael, G. R., Chang, J. S., Charlson, R. J., Cober, S., Ellis, W. G., Fischer, C. J., Hales, J. M., Hastie, D. R., Iversen, T., Jacob, D. J., John, K., Johnson, J. E., Kasibhatla, P. S., Langner, J., Lelieveld, J., Levy, H., Lipschultz, F., Merrill, J. T., Michaels, A. F., Miller, J. M., Moody, J. L., Pinto, J., Pszenny, A. A. P., Spiro, P. A., Tarrason, L., Turner, S. M., and Whelpdale, D. M. (1992). Sulfur and nitrogen levels in the North Atlantic Ocean's atmosphere: A synthesis of field and modeling results. *Global Biogeochemical Cycles*, 6(2), doi:10.1029/91GB02977.

Garbe, C. S., Rutgersson, A., Boutin, J., de Leeuw, G., Delille, B., Fairall, C. W., Gruber, N., Hare, J., Ho, D. T., Johnson, M. T., Nightingale, P. D., Pettersson, H., Piskozub, J., Sahlée, E., Tsai, W., Ward, B., Woolf, D. K., and Zappa, C. J. (2014). Transfer across the air-sea interface. In Liss, P. S. and Johnson, M. T., editors, *Ocean-Atmosphere Interactions of Gases and Particles*, pages 55–112. Springer, Heidelberg.

Garcia, H. E., Locarnini, R. A., Boyer, T. P., Antonov, J. I., Zweng, M. M., Baranova, O. K., and Johnson, D. R. (2010). *World Ocean Atlas 2009, Volume 4: Nutrients (Phosphate, Nitrate, Silicate)*. In Levitus, S., editor, *NOAA Atlas NESDIS 71*, page 398. U.S. Government Printing Office, Washington, D.C.

Gargett, A. E. (1991). Physical processes and the maintenance of nutrient-rich euphotic zones. *Limnology and Oceanography*, 36(8):1527–1545, doi:10.4319/lo.1991.36.8.1527.

Giorgi, F. and Chameides, W. L. (1986). Rainout lifetimes of highly soluble aerosols and gases as inferred from simulations with a general circulation model. *Journal of Geophysical Research: Atmospheres*, 91(D13), doi:10.1029/JD091iD13p14367.

Gunson, J. R., Spall, S. A., Anderson, T. R., Jones, A., Totterdell, I. J., and Woodage, M. J. (2006). Climate sensitivity to ocean dimethylsulphide emissions. *Geophysical Research Letters*, 33(7), doi:10.1029/2005GL024982.

Halloran, P. R., Bell, T. G., and Totterdell, I. J. (2010). Can we trust empirical marine DMS parameterisations within projections of future climate? *Biogeosciences*, 7(5):1645–1656, doi:10.5194/bg-7-1645-2010.

Hankin, S., Callahan, J., Manke, A., O'Brien, K., and Li, J. (2007). *Ferret user's guide version 6.02*.

Hare, J. E., Fairall, C. W., McGillis, W. R., Edson, J. B., Ward, B., and Wanninkhof, R. (2004). Evaluation of the National Oceanic and Atmospheric Administration/Coupled-Ocean Atmospheric Response Experiment (NOAA/COARE) air-sea gas transfer parameterization using GasEx data. *Journal of Geophysical Research: Oceans*, 109(C8), doi:10.1029/2003JC001831.

Hefu, Y. and Kirst, G. O. (1997). Effect of UV-radiation on DMSP content and DMS formation of Phaeocystis Antarctica. *Polar Biology*, 18(6):402–409, doi:10.1007/s003000050206.

Hind, A. J., Rauschenberg, C. D., Johnson, J. E., Yang, M., and Matrai, P. A. (2011). The use of algorithms to predict surface seawater dimethyl sulphide concentrations in the SE Pacific, A region of steep gradients in primary productivity, biomass and mixed layer depth. *Biogeosciences*, 8(1):1–16, doi:10.5194/bg-8-1-2011.

Huebert, B. J., Blomquist, B. W., Hare, J. E., Fairall, C. W., Johnson, J. E., and Bates, T. S. (2004). Measurement of the sea-air DMS flux and transfer velocity using eddy correlation. *Geophysical Research Letters*, 31(23), doi:10.1029/2004GL021567.

Hurrell, J. W., Hack, J. J., Shea, D., Caron, J. M., and Rosinski, J. (2008). A new sea surface temperature and sea ice boundary dataset for the Community Atmosphere Model. *Journal of Climate*, 21(19):5145–5153, doi:10.1175/2008JCLI2292.1.

Ilyina, T., Six, K. D., Segschneider, J., Maier-Reimer, E., Li, H., and Núñez-Riboni, I. (2013). Global ocean biogeochemistry model HAMOCC: Model architecture and performance as component of the MPI-Earth system model in different CMIP5 experimental realizations. *Journal of Advances in Modeling Earth Systems*, 5(2):287–315, doi:10.1029/2012MS000178.

Johnson, M. T. (2010). A numerical scheme to calculate temperature and salinity dependent air-water transfer velocities for any gas. *Ocean Science*, 6(4):913–932, doi:10.5194/os-6-913-2010.

Kameyama, S., Tanimoto, H., Inomata, S., Yoshikawa-Inoue, H., Tsunogai, U., Tsuda, A., Uematsu, M., Ishii, M., Sasano, D., Suzuki, K., and Nosaka, Y. (2013). Strong relationship between dimethyl sulfide and net community production in the Western Subarctic Pacific. *Geophysical Research Letters*, 40(15), doi:10.1002/grl.50654.

Karsten, U., Kirst, G., and Wiencke, C. (1992). Dimethylsulphoniopropionate (DMSP) accumulation in green macioalgae from polar to temperate regions: Interactive effects of light versus salinity and light versus temperature. *Polar Biology*, 12(6-7):603–607, doi:10.1007/BF00236983.

Karsten, U., Kück, K., Vogt, C., and Kirst, G. (1996). Dimethylsulfoniopropionate production in phototrophic organisms and its physiological functions as a cryoprotectant. In Kiene, R. P., Visscher, P. T., Keller, M. D., and Kirst, G. O., editors, *Biological and environmental chemistry of DMSP and related sulfonium compounds*, pages 143–153. Springer US.

Kato, S., Loeb, N. G., G, R. F., Doelling, D. R., Rutan, D. A., Caldwell, T. E., Yu, L., and Weller, R. A. (2013). Surface irradiances consistent with CERES-derived top-of-atmosphere shortwave and longwave irradiances. *Journal of Climate*, 26(9):2719–2740, doi:10.1175/JCLI-D-12-00436.1.

Keller, M. D., Bellows, W. K., and Guillard, R. R. L. (1989). Dimethyl sulfide production in marine phytoplankton. In *Biogenic sulfur in the environment*, chapter 12, pages 167–182. American Chemical Society, Washington, D. C., 1 edition. Edited by E. S. Saltzman and W. J. Cooper.

Kettle, A. J. and Andreae, M. O. (2000). Flux of dimethylsulfide from the oceans: A comparison of updated data sets and flux models. *Journal of Geophysical Research: Atmospheres*, 105(D22), doi:10.1029/2000JD900252.

Kettle, A. J., Andreae, M. O., Amouroux, D., Andreae, T., Bates, T., Berresheim, H., Bingemer, H., et al. (1999). A global database of sea surface dimethylsulfide (DMS) measurements and a procedure to predict sea surface DMS as a function of latitude, longitude, and month. *Global Biogeochemical Cycles*, 13(2), doi:10.1029/1999GB900004.

Kieber, D. J., Jiao, J., Kiene, R. P., and Bates, T. S. (1996). Impact of dimethylsulfide photochemistry on methyl sulfur cycling in the equatorial Pacific Ocean. *Journal of Geophysical Research: Oceans*, 101(C2), doi:10.1029/95JC03624.

Kiene, R. P. and Linn, L. J. (2000). The fate of dissolved dimethylsulfoniopropionate (DMSP) in seawater: tracer studies using 35S-DMSP. *Geochimica et Cosmochimica Acta*, 64(16):2797–2810, doi:10.1016/S0016-7037(00)00399-9.

Kiene, R. P., Linn, L. J., and Bruton, J. A. (2000). New and important roles for DMSP in marine microbial communities. *Journal of Sea Research*, 43(3-4):209–224, doi:10.1016/S1385-1101(00)00023-X.

Kinne, S., Schulz, M., Textor, C., Guibert, S., Balkanski, Y., Bauer, S. E., Berntsen, T., Berglen, T. F., Boucher, O., Chin, M., Collins, W., Dentener, F., Diehl, T., Easter, R., Feichter, J., Fillmore, D., Ghan, S. J., Ginoux, P., Gong, S., Grini, A., Hendricks, J., Herzog, M., Horowitz, L., Isaksen, I., Iversen, T., Kirkevåg, A., Kloster, S., Koch, D., Kristjansson, J. E., Krol, M., Lauer, A., Lamarque, J. F., Lesins, G., Liu, X., Lohmann, U., Montanaro, V., Myhre, G., Penner, J. E., Pitari, G., Reddy, S., Seland, Ø., Stier, P., Takemura, T., and Tie, X. (2006). An AeroCom initial assessment – optical properties in aerosol component modules of global models. *Atmospheric Chemistry and Physics*, 6(7):1815–1834, doi:10.5194/acp-6-1815-2006.

Kloster, S., Feichter, J., Reimer, E. M., Six, K. D., Stier, P., and Wetzel, P. (2006). DMS cycle in the marine ocean-atmosphere system – A global model study. *Biogeosciences*, 3(1):29–51, doi:10.5194/bg-3-29-2006.

Kloster, S., Six, K. D., Feichter, J., Maier-Reimer, E., Roeckner, E., Wetzel, P., Stier, P., and Esch, M. (2007). Response of dimethylsulfide (DMS) in the ocean and atmosphere to global warming. *Journal of Geophysical Research: Biogeosciences*, 112(G3), doi:10.1029/2006JG000224.

Kondo, J. (1975). Air-sea bulk transfer coefficients in diabatic conditions. *Boundary-Layer Meteorology*, 9(1):91–112, doi:10.1007/BF00232256.

Lamarque, J. F., Bond, T. C., Eyring, V., Granier, C., Heil, A., Klimont, Z., Lee, D., Liousse, C., Mieville, A., Owen, B., Schultz, M. G., Shindell, D., Smith, S. J., Stehfest, E., Van Aardenne, J., Cooper, O. R., Kainuma, M., Mahowald, N., McConnell, J. R., Naik, V., Riahi, K., and van Vuuren, D. P. (2010). Historical (1850–2000) gridded anthropogenic and biomass burning emissions of reactive gases and aerosols: methodology and application. *Atmospheric Chemistry and Physics*, 10(15):7017–7039, doi:10.5194/acp-10-7017-2010.

Lana, A., Bell, T. G., Simó, R., Vallina, S. M., Ballabrera-Poy, J., Kettle, A. J., Dachs, J., Bopp, L., Saltzman, E. S., Stefels, J., Johnson, J. E., and Liss, P. S. (2011). An updated climatology of surface dimethlysulfide concentrations and emission fluxes in the global ocean. *Global Biogeochemical Cycles*, 25(1), doi:10.1029/2010GB003850.

Lana, A., Simó, R., Vallina, S. M., and Dachs, J. (2012). Re-examination of global emerging patterns of ocean DMS concentration. *Biogeochemistry*, 110(1-3):173–182, doi:10.1007/s10533-011-9677-9.

Le Clainche, Y., Vézina, A., Levasseur, M., Cropp, R. A., Gunson, J. R., Vallina, S. M., Vogt, M., Lancelot, C., Allen, J. I., Archer, S. D., Bopp, L., Deal, C., Elliott, S., Jin, M., Malin, G., Schoemann, V., Simó, R., Six, K. D., and Stefels, J. (2010). A first appraisal of prognostic ocean DMS models and prospects for their use in climate models. *Global Biogeochemical Cycles*, 24(3), doi:10.1029/2009GB003721.

Lee-Taylor, J., Madronich, S., Fischer, C., and Mayer, B. (2010). A climatology of UV radiation, 1979–2000, 65S–65N. In Gao, W., Slusser, J. R., and Schmoldt, D. L., editors, *UV radiation in global climate change: Measurements, modeling and effects on ecosystems*, pages 1–20. Springer, Berlin Heidelberg.

Levitus, S. (1982). Climatological atlas of the World Ocean. Technical report, Geophysical Fluid Dynamics Laboratory Princeton, N.J., Rockville.

Liss, P. and Slater, P. (1974). Flux of gases across air-sea interface. *Nature*, 247(5438):181–184, doi:10.1038/247181a0.

Liss, P. S., Marandino, C. A., Dahl, E. E., Helmig, D., Hintsa, E. J., Hughes, C., Johnson, M. T., Moore, R. M., Plane, J. M. C., Quack, B., Singh, H. B., Stefels, J., von Glasow, R., and Williams, J. (2014). Short-lived trace gases in the surface ocean and the atmosphere. In Liss, P. S. and Johnson, M. T., editors, *Ocean-Atmosphere Interactions of Gases and Particles*, Springer Earth System Sciences, pages 1–54. Springer, Heidelberg.

Liss, P. S. and Merlivat, L. (1986). Air-sea gas exchange rates: Introduction and synthesis. In Buat-Ménard, P., editor, *The role of air-sea exchange in geochemical cycling*, volume 185 of *NATO ASI Series*, pages 113–127. Springer Netherlands.

Liss, P. S., Watson, A. J., Liddicoat, M. I., Malin, G., Nightingale, P. D., Turner, S. M., and Upstill-Goddard, R. C. (1993). Trace gases and air-sea exchanges. *Philosophical*

Transactions of the Royal Society of London. Series A: Mathematical, Physical and Engineering Sciences, 343(1669):531–541, doi:10.1098/rsta.1993.0064.

Lizotte, M., Levasseur, M., Michaud, S., Scarratt, M. G., Merzouk, A., Gosselin, M., Pommier, J., Rivkin, R. B., and Kiene, R. P. (2012). Macroscale patterns of the biological cycling of dimethylsulfoniopropionate (DMSP) and dimethylsulfide (DMS) in the Northwest Atlantic. *Biogeochemistry*, 110(1-3):183–200, doi:10.1007/s10533-011-9698-4.

Locarnini, R. A., Mishonov, A. V., Antonov, J. I., Boyer, T. P., Garcia, H. E., Baranova, O. K., Zweng, M. M., and Johnson, D. R. (2010). *World Ocean Atlas 2009, Volume 1: Temperature*. In Levitus, S., editor, *NOAA Atlas NESDIS 68*, page 184. U.S. Government Printing Office, Washington, D.C.

Loeb, N. G., Wielicki, B. A., Doelling, D. R., Smith, G. L., Keyes, D. F., Kato, S., Manalo-Smith, N., and Wong, T. (2009). Toward optimal closure of the Earth's top-of-atmosphere radiation budget. *Journal of Climate*, 22(3):748–766, doi:10.1175/2008JCLI2637.1.

Lohmann, U., von Salzen, K., McFarlane, N., Leighton, H. G., and Feichter, J. (1999). Tropospheric sulfur cycle in the Canadian general circulation model. *Journal of Geophysical Research: Atmospheres*, 104(D21), doi:10.1029/1999JD900343.

Longhurst, A., Sathyendranath, S., Platt, T., and Caverhill, C. (1995). An estimate of global primary production in the ocean from satellite radiometer data. *Journal of Plankton Research*, 17(6):1245–1271, doi:10.1093/plankt/17.6.1245.

Lovelock, J. E., Maggs, R. J., and Rasmussen, R. A. (1972). Atmospheric dimethyl sulphide and the natural sulphur cycle. *Nature*, 237(5356):452–453, doi:10.1038/237452a0.

Maahs, H. G. (1983). Kinetics and mechanism of the oxidation of S(IV) by ozone in aqueous solution with particular reference to SO2 conversion in nonurban tropospheric clouds. *Journal of Geophysical Research: Oceans*, 88(C15), doi:10.1029/JC088iC15p10721.

Malin, G., Turner, S. M., and Liss, P. S. (1992). Sulfur: The plankton/climate connection. *Journal of Phycology*, 28(5):590–597, doi:10.1111/j.0022-3646.1992.00590.x.

Malin, G., Wilson, W. H., Bratbak, G., Liss, P. S., and Mann., N. H. (1998). Elevated production of dimethylsulfide resulting from viral infection of cultures of Phaeocystis Pouchetii. *Limnology and Oceanography*, 43(6):1389–1393, doi:10.4319/lo.1998.43.6.1389.

Marandino, C. A., De Bruyn, W. J., Miller, S. D., and Saltzman, E. S. (2009). Open ocean DMS air/sea fluxes over the Eastern South Pacific Ocean. *Atmospheric Chemistry and Physics*, 9(2):345–356, doi:10.5194/acp-9-345-2009.

Martin, L. R. (1984). Kinetic studies of sulfite oxidation in aqueous solution. In *Acid precipitation Series Volume 3: SO_2, NO and NO_2 Oxidation Mechanisms: Atmospheric Considerations*, pages 63–100. Butterworth Publishers, Boston.

McClain, C. R. (2009). A decade of satellite ocean color observations. *Annual Review of Marine Science*, 1:19–42, doi:10.1146/annurev.marine.010908.163650.

McClain, C. R., Signorini, S. R., and Christian, J. R. (2004). Subtropical gyre variability observed by ocean-color satellites. *Deep-Sea Research Part II: Topical Studies in Oceanography*, 51(1-3):281–301, doi:10.1016/j.dsr2.2003.08.002.

McGillis, W. R., Dacey, J. W. H., Frew, N. M., Bock, E., and Nelson, R. K. (2000). Water-air flux of dimethylsulfide. *Journal of Geophysical Research: Oceans*, 105(C1), doi:10.1029/1999JC900243.

Miles, C., Bell, T., and Suntharalingam, P. (2012). Investigating the inter-relationships between water attenuated irradiance, primary production and DMS(P). *Biogeochemistry*, 110(1-3):201–213, doi:10.1007/s10533-011-9697-5.

Miles, C. J., Bell, T. G., and Lenton, T. M. (2009). Testing the relationship between the solar radiation dose and surface DMS concentrations using in situ data. *Biogeosciences*, 6(9):1927–1934, doi:10.5194/bg-6-1927-2009.

Monahan, A. (2006). The probability distribution of sea surface wind speeds. Part II: Dataset intercomparison and seasonal variability. *Journal of Climate*, 19(4):521–534, doi:10.1175/JCLI3641.1.

Monterey, G. and Levitus, S. (1997). Seasonal variability of mixed layer depth for the World Ocean. Technical report, National Oceanographic Oala Center Ocean Climate Laboratory Silver Spring, Maryland 20910, Washington, D.C.

Moss, R. H., Edmonds, J. A., Hibbard, K. A., Manning, M. R., Rose, S. K., van Vuuren, D. P., Carter, T. R., Emori, S., Kainuma, M., Kram, T., Meehl, G. A., Mitchell, J. F. B., Nakicenovic, N., Riahi, K., Smith, S. J., Stouffer, R. J., Thomson, A. M., Weyant, J. P., and Wilbanks, T. J. (2010). The next generation of scenarios for climate change research and assessment. *Nature*, 463(7282):747–756, doi:10.1038/nature08823.

Myhre, G., Shindell, D., Bréon, F.-M., Collins, W., Fuglestvedt, J., Huang, J., Koch, D., Lamarque, J.-F., Lee, D., Mendoza, B., Nakajima, T., Robock, A., Stephens, G., Takemura, T., and Zhang, H. (2013). Anthropogenic and natural radiative forcing. In Stocker, T., Qin, D., Plattner, G.-K., Tignor, M., Allen, S., Boschung, J., Nauels, A., Xia, Y., Bex, V., and Midgley, P., editors, *Climate Change 2013: The physical science basis. Contribution of Working Group I to the Fifth Assessment Report of the Intergovernmental Panel on Climate Change*. Cambridge University Press, Cambridge, United Kingdom and New York, NY, USA.

Nguyen, B. C., Belviso, S., Mihalopoulos, N., Gostan, J., and Nival, P. (1988). Dimethyl sulfide production during natural phytoplanktonic blooms. *Marine Chemistry*, 24(2):133–141, doi:10.1016/0304-4203(88)90044-8.

Nightingale, P. D., Malin, G., Law, C. S., Watson, A. J., Liss, P. S., Liddicoat, M. I., Boutin, J., and Upstill-Goddard, R. C. (2000). In situ evaluation of air-sea gas exchange parameterizations using novel conservative and volatile tracers. *Global Biogeochemical Cycles*, 14(1), doi:10.1029/1999GB900091.

Palmer, J. R. and Totterdell, I. J. (2001). Production and export in a global ocean ecosystem model. *Deep-Sea Research Part I: Oceanographic Research Papers*, 48(5):1169–1198, doi:10.1016/S0967-0637(00)00080-7.

Pham, M., Müller, J., Brasseur, G. P., Granier, C., and Mégie, G. (1995). A three-dimensional study of the tropospheric sulfur cycle. *Journal of Geophysical Research: Atmospheres*, 100(D12), doi:10.1029/95JD02095.

Polimene, L., Archer, S. D., Butenschön, M., and Allen, J. I. (2012). A mechanistic explanation of the Sargasso Sea DMS "summer paradox". *Biogeochemistry*, 110(1-3):243–255, doi:10.1007/s10533-011-9674-z.

Quinn, P. K. and Bates, T. S. (2011). The case against climate regulation via oceanic phytoplankton sulphur emissions. *Nature*, 480(7375):51–56, doi:10.1038/nature10580.

Raina, J.-B., Tapiolas, D. M., Forêt, S., Lutz, A., Abrego, D., Ceh, J., Seneca, F. O., Clode, P. L., Bourne, D. G., Willis, B. L., and Motti, C. A. (2013). DMSP biosynthesis by an animal and its role in coral thermal stress response. *Nature*, 502(7473):677–680, doi:10.1038/nature12677.

Saltzman, E. S., King, D. B., Holmen, K., and Leck, C. (1993). Experimental determination of the diffusion coefficient of dimethylsulfide in water. *Journal of Geophysical Research: Oceans*, 98(C9), doi:10.1029/93JC01858.

Sciare, J., Mihalopoulos, N., and Nguyen, B. C. (1999). Summertime seawater concentrations of dimethylsulfide in the Western Indian Ocean: Reconciliation of fluxes and spatial variability with long-term atmospheric observations. *Journal of Atmospheric Chemistry*, 32(3):357–373, doi:10.1023/A:1006132001945.

Shaw, G. (1983). Bio-controlled thermostasis involving the sulfur cycle. *Climatic Change*, 5(3):297–303, doi:10.1007/BF02423524.

Simó, R. (2004). From cells to globe: approaching the dynamics of DMS(P) in the ocean at multiple scales. *Canadian Journal of Fisheries and Aquatic Sciences*, 61(5):673–684, doi:10.1139/f04-030.

Simó, R. and Dachs, J. (2002). Global ocean emission of dimethylsulfide predicted from biogeophysical data. *Global Biogeochemical Cycles*, 16(4), doi:10.1029/2001GB001829.

Simó, R. and Pedrós-Alió, C. (1999). Role of vertical mixing in controlling the oceanic production of dimethyl sulphide. *Nature*, 402(6760):396–399, doi:10.1038/46516.

Six, K. D., Kloster, S., Ilyina, T., Archer, S. D., Zhang, K., and Maier-Reimer, E. (2013). Global warming amplified by reduced sulphur fluxes as a result of ocean acidification. *Nature Climate Change*, 3(11):975–978, doi:10.1038/nclimate1981.

Six, K. D. and Maier-Reimer, E. (2006). What controls the oceanic dimethylsulfide (DMS) cycle? A modeling approach. *Global Biogeochemical Cycles*, 20(4), doi:10.1029/2005GB002674.

Slezak, D., Brugger, A., and Herndl, G. J. (2001). Impact of solar radiation on the

biological removal of dimethylsulfoniopropionate and dimethylsulfide in marine surface waters. *Aquatic Microbial Ecology*, 25(1):87–97, doi:10.3354/ame025087.

Slingo, J. M. (1987). The development and verification of a cloud prediction scheme for the ECMWF model. *Quarterly Journal of the Royal Meteorological Society*, 113(477):899–927, doi:10.1002/qj.49711347710.

Smith, R. C. and Baker, K. S. (1979). Penetration of UV-B and biologically effective dose-rates in natural waters. *Photochemistry and Photobiology*, 29(2):311–323, doi:10.1111/j.1751-1097.1979.tb07054.x.

Spiro, P. A., Jacob, D. J., and Logan, J. A. (1992). Global inventory of sulfur emissions with $1° \times 1°$ resolution. *Journal of Geophysical Research: Atmospheres*, 97(D5), doi:10.1029/91JD03139.

Springer, A. M., McRoy, C. P., and Flint, M. V. (1996). The Bering Sea green belt: shelf-edge processes and ecosystem production. *Fisheries Oceanography*, 5(3-4):205–223, doi:10.1111/j.1365-2419.1996.tb00118.x.

Stefels, J. (2000). Physiological aspects of the production and conversion of DMSP in marine algae and higher plants. *Journal of Sea Research*, 43(3-4):183–197, doi:10.1016/S1385-1101(00)00030-7.

Stefels, J., Steinke, M., Turner, S., Malin, G., and Belviso, S. (2007). Environmental constraints on the production and removal of the climatically active gas dimethylsulphide (DMS) and implications for ecosystem modelling. *Biogeochemistry*, 83(1-3):245–275, doi:10.1007/s10533-007-9091-5.

Steiner, N. and Denman, K. (2008). Parameter sensitivities in a 1-D model for DMS and sulphur cycling in the upper ocean. *Deep-Sea Research Part I: Oceanographic Research Papers*, 55(7):847–865, doi:10.1016/j.dsr.2008.02.010.

Steinke, M., Malin, G., and Liss, P. S. (2002). Trophic interactions in the sea: An ecological role for climate relevant volatiles? *Journal of Phycology*, 38(4):630–638, doi:10.1046/j.1529-8817.2002.02057.x.

Stevens, B. and Feingold, G. (2009). Untangling aerosol effects on clouds and precipitation in a buffered system. *Nature*, 461(7264):607–613, doi:10.1038/nature08281.

Sunda, W., Kieber, D. J., Kiene, R. P., and Huntsman, S. (2002). An antioxidant function for DMSP and DMS in marine algae. *Nature*, 418(6895):317–320, doi:10.1038/nature00851.

Tarrasón, L., Turner, S., and Fløisand, I. (1995). Estimation of seasonal dimethyl sulphide fluxes over the North Atlantic Ocean and their contribution to European pollution levels. *Journal of Geophysical Research: Atmospheres*, 100(D6), doi:10.1029/95JD00849.

Taylor, K. E. (2001). Summarizing multiple aspects of model performance in a single diagram. *Journal of Geophysical Research: Atmospheres*, 106(D7), doi:10.1029/2000JD900719.

Taylor, K. E., Stouffer, R. J., and Meehl, G. A. (2012). An overview of CMIP5 and

the experiment design. *Bulletin of the American Meteorological Society*, 93:485–498, doi:10.1175/BAMS-D-11-00094.1.

Textor, C., Schulz, M., Guibert, S., Kinne, S., Balkanski, Y., Bauer, S., Berntsen, T., Berglen, T., Boucher, O., Chin, M., Dentener, F., Diehl, T., Easter, R., Feichter, H., Fillmore, D., Ghan, S. J., Ginoux, P., Gong, S., Grini, A., Hendricks, J., Horowitz, L., Huang, P., Isaksen, I., Iversen, T., Kloster, S., Koch, D., Kirkevåg, A., Kristjansson, J. E., Krol, M., Lauer, A., Lamarque, J. F., Liu, X., Montanaro, V., Myhre, G., Penner, J. E., Pitari, G., Reddy, S., Seland, Ø., Stier, P., Takemura, T., and Tie, X. (2006). Analysis and quantification of the diversities of aerosol life cycles within AeroCom. *Atmospheric Chemistry and Physics*, 6(7):1777–1813, doi:10.5194/acp-6-1777-2006.

Thomas, M. A., Suntharalingam, P., Pozzoli, L., Devasthale, A., Kloster, S., Rast, S., Feichter, J., and Lenton, T. M. (2011). Rate of non-linearity in DMS aerosol-cloud-climate interactions. *Atmospheric Chemistry and Physics*, 11(21):11175–11183, doi:10.5194/acp-11-11175-2011.

Todd, J. D., Curson, A. R. J., Dupont, C. L., Nicholson, P., and Johnston, A. W. B. (2009). The dddP gene, encoding a novel enzyme that converts dimethylsulfoniopropionate into dimethyl sulfide, is widespread in ocean metagenomes and marine bacteria and also occurs in some Ascomycete fungi. *Environmental Microbiology*, 11(6):1376–1385, doi:10.1111/j.1462-2920.2009.01864.x.

Todd, J. D., Rogers, R., Li, Y. G., Wexler, M., Bond, P. L., Sun, L., Curson, A. R. J., Malin, G., Steinke, M., and Johnston, A. W. B. (2007). Structural and regulatory genes required to make the gas dimethyl sulfide in bacteria. *Science*, 315(5812):666–669, doi:10.1126/science.1135370.

Toole, D., Slezak, D., Kiene, R., Kieber, D., and Siegel, D. (2006). Effects of solar radiation on dimethylsulfide cycling in the Western Atlantic Ocean. *Deep-Sea Research Part I: Oceanographic Research Papers*, 53(1):136–153, doi:10.1016/j.dsr.2005.09.003.

Toole, D. A., Kieber, D. J., Kiene, R. P., Siegel, D. A., and Nelson, N. B. (2003). Photolysis and the dimethylsulfide (DMS) summer paradox in the Sargasso Sea. *Limnology and Oceanography*, 48(3):1088–1100, doi:10.4319/lo.2003.48.3.1088.

Toole, D. A. and Siegel, D. A. (2004). Light-driven cycling of dimethylsulfide (DMS) in the Sargasso Sea: Closing the loop. *Geophysical Research Letters*, 31(9), doi:10.1029/2004GL019581.

Toole, D. A., Siegel, D. A., and Doney, S. C. (2008). A light-driven, one-dimensional dimethylsulfide biogeochemical cycling model for the Sargasso Sea. *Journal of Geophysical Research: Biogeosciences*, 113(G2), doi:10.1029/2007JG000426.

Tortell, P., Guéguen, C., Long, M., Payne, C., Lee, P., and DiTullio, G. (2011). Spatial variability and temporal dynamics of surface water pCO_2, $\Delta O_2/Ar$ and dimethylsulfide in the Ross Sea, Antarctica. *Deep-Sea Research Part I: Oceanographic Research Papers*, 58(3):241–259, doi:10.1016/j.dsr.2010.12.006.

Tortell, P. D. (2005). Small-scale heterogeneity of dissolved gas concentrations in marine continental shelf waters. *Geochemistry, Geophysics, Geosystems*, 6(11), doi:10.1029/2005GC000953.

Turner, S., Malin, G., Nightingale, P., and Liss, P. (1996). Seasonal variation of dimethyl sulphide in the North Sea and an assessment of fluxes to the atmosphere. *Marine Chemistry*, 54(3-4):245–262, doi:10.1016/0304-4203(96)00028-X.

Turner, S., Nightingale, P., Broadgate, W., and Liss, P. (1995). The distribution of dimethyl sulphide and dimethylsulphoniopropionate in Antarctic waters and sea ice. *Deep-Sea Research Part II: Topical Studies in Oceanography*, 42(4-5):1059–1080, doi:10.1016/0967-0645(95)00066-Y.

Vairavamurthy, A., Andreae, M. O., and Iverson, R. L. (1985). Biosynthesis of dimethlysulfide and dimethylpropiothetin by Hymenomonas carterae in relation to sulfur source and salinity variations. *Limnology and Oceanography*, 30(1):59–70, doi:10.4319/lo.1985.30.1.0059.

Vallina, S. M. and Simó, R. (2007). Strong relationship between DMS and the solar radiation dose over the global surface ocean. *Science*, 315(5811):506–508, doi:10.1126/science.1133680.

Vallina, S. M., Simó, R., Anderson, T. R., Gabric, A., Cropp, R., and Pacheco, J. M. (2008). A dynamic model of oceanic sulfur (DMOS) applied to the Sargasso Sea: Simulating the dimethylsulfide (DMS) summer paradox. *Journal of Geophysical Research: Biogeosciences*, 113(G1), doi:10.1029/2007JG000415.

Vallina, S. M., Simó, R., Gassó, S., de Boyer Montégut, C., del Río, E., Jurado, E., and Dachs, J. (2007a). Analysis of a potential "solar radiation dose–dimethylsulfide–cloud condensation nuclei" link from globally mapped seasonal correlations. *Global Biogeochemical Cycles*, 21(2), doi:10.1029/2006GB002787.

Vallina, S. M., Simó, R., and Manizza, M. (2007b). Weak response of oceanic dimethylsulfide to upper mixing shoaling induced by global warming. *Proceedings of the National Academy of Sciences of the United States of America*, 104(41):16004–16009, doi:10.1073/pnas.0700843104.

Vila-Costa, M., Del Valle, D. A., González, J. M., Slezak, D., Kiene, R. P., Sánchez, O., and Simó, R. (2006). Phylogenetic identification and metabolism of marine dimethylsulfide-consuming bacteria. *Environmental Microbiology*, 8(12):2189–2200, doi:10.1111/j.1462-2920.2006.01102.x.

Vogt, M., Vallina, S. M., Buitenhuis, E. T., Bopp, L., and Le Quéré, C. (2010). Simulating dimethylsulphide seasonality with the dynamic green ocean model PlankTOM5. *Journal of Geophysical Research: Oceans*, 115(C6), doi:10.1029/2009JC005529.

von Salzen, K., Leighton, H. G., Ariya, P. A., Barrie, L. A., Gong, S. L., Blanchet, J.-P., Spacek, L., Lohmann, U., and Kleinman, L. I. (2000). Sensitivity of sulphate aerosol size distributions and CCN concentrations over North America to SO_x emissions and H_2O_2 concentrations. *Journal of Geophysical Research: Atmospheres*, 105(D8), doi:10.1029/2000JD900027.

von Salzen, K., Scinocca, J. F., McFarlane, N. A., Li, J., Cole, J. N. S., Plummer, D., Verseghy, D., Reader, M. C., Ma, X., Lazare, M., and Solheim, L. (2013). The Canadian Fourth Generation Atmospheric Global Climate Model (CanAM4). Part I: Representation of physical processes. *Atmosphere-Ocean*, 51(1):104–125, doi:10.1080/07055900.2012.755610.

Wanninkhof, R. (1992). Relationship between wind speed and gas exchange over the ocean. *Journal of Geophysical Research: Oceans*, 97(C5), doi:10.1029/92JC00188.

Wanninkhof, R., Ledwell, J. R., and Broecker, W. S. (1985). Gas exchange-wind speed relation measured with sulfur hexafluoride on a lake. *Science*, 227(4691):1224–1226, doi:10.1126/science.227.4691.1224.

Watts, M. and Bigg, G. (2001). Modelling the nitrogen cycle and DMS production in Lagrangian experiments in the North Atlantic. *Deep-Sea Research Part II: Topical Studies in Oceanography*, 48(4-5):1019–1042, doi:10.1016/S0967-0645(00)00107-7.

Winn, C. D., Campbell, L., Christian, J. R., Letelier, R. M., Hebel, D. V., Dore, J. E., Fujieki, L., and Karl, D. M. (1995). Seasonal variability in the phytoplankton community of the North Pacific subtropical gyre. *Global Biogeochemical Cycles*, 9(4), doi:10.1029/95GB02149.

Wolfe, G. V. and Steinke, M. (1996). Grazing-activated production of dimethyl sulfide (DMS) by two clones of Emiliania Huxleyi. *Limnology and Oceanography*, 41(6):1151–1160, doi:10.4319/lo.1996.41.6.1151.

Wolfe, G. V., Steinke, M., and Kirst, G. O. (1997). Grazing-activated chemical defence in a unicellular marine alga. *Nature*, 387(6636):894–897, doi:10.1038/43168.

Woodhouse, M. T., Carslaw, K. S., Mann, G. W., Vallina, S. M., Vogt, M., Halloran, P. R., and Boucher, O. (2010). Low sensitivity of cloud condensation nuclei to changes in the sea-air flux of dimethyl-sulphide. *Atmospheric Chemistry and Physics*, 10(16):7545–7559, doi:10.5194/acp-10-7545-2010.

Woodhouse, M. T., Mann, G. W., Carslaw, K. S., and Boucher, O. (2013). Sensitivity of cloud condensation nuclei to regional changes in dimethyl-sulphide emissions. *Atmospheric Chemistry and Physics*, 13(5):2723–2733, doi:10.5194/acp-13-2723-2013.

Yang, M., Blomquist, B. W., Fairall, C. W., Archer, S. D., and Huebert, B. J. (2011). Air-sea exchange of dimethylsulfide in the Southern Ocean: Measurements from SO GasEx compared to temperate and tropical regions. *Journal of Geophysical Research: Oceans*, 116(C4), doi:10.1029/2010JC006526.

Yoch, D. C. (2002). Dimethylsulfoniopropionate: its sources, role in the marine food web, and biological degradation to dimethylsulfide. *Applied and Environmental Microbiology*, 68(12):5804–5815, doi:10.1128/AEM.68.12.5804-5815.2002.

Zemmelink, H. J., Dacey, J. W., and Hintsa, E. J. (2004a). Direct measurements of biogenic dimethylsulphide fluxes from the oceans: A synthesis. *Canadian Journal of Fisheries and Aquatic Sciences*, 61(5):836–844, doi:10.1139/f04-047.

Zemmelink, H. J., Dacey, J. W. H., Hintsa, E. J., McGillis, W. R., Gieskes, W. W. C., Klaassen, W., de Groot, H. W., and de Baar, H. J. W. (2004b). Fluxes and gas transfer rates of the biogenic trace gas DMS derived from atmospheric gradients. *Journal of Geophysical Research: Oceans*, 109(C8), doi:10.1029/2003JC001795.